Rolled up Si-based Three Dimensional Micro-/Nanostructures for MEMS/NEMS

INAUGURALDISSERTATION
zur
Erlangung der Würde eines Doktors der Philosophie
vorgelegt der
Philosophisch-Naturwissenschaftlichen Fakultät
der Universität Basel
von

Li Zhang

aus China

Basel, 2006

Genehmigt von der Philosophisch-Naturwissenschaftlichen Fakultät auf Antrag

der Herren Professoren:

Prof. Dr. Christian Schönenberger

Prof. Dr. Detlev Grützmacher

Prof. Dr. Oliver Schmidt

Basel, den 10. 2006

Prof. Dr. Hans-Peter Hauri, Dekan

Abstract

Recently, by combination of the “top down” and “bottom up” approaches, a new strategy to fabricate 3D micro-/nanostructures named self-scrolling technique has been introduced by Prinz *et al.* in 1999. In this PhD dissertation, the method and principle of how to scale down such kinds of novel structures in a better controllable way are explored. Started from the investigation of scrolling SiGe/Si structures in a micrometer scale, which is fundamental for the further research in this field, we have controllably fabricated two different 3D structures, i.e. tubes and helices, from patterned SiGe/Si bilayers and SiGe/Si/Cr multi-layers. Based on our experimental results, the scrolling principles to form Si based tubes and helices from 2D micrometer scale strained thin films are well developed. Furthermore, special attention is paid to find new phenomena and behaviors of the 3D nanostructures when the designed pattern of the strained thin films is scaled down to nanometer size. An anomalous coiling of the strained thin films has been identified, which could not be interpreted by common principles adopted for rolling-up of the mesa-structures in micrometer scale. The followed intensive investigations have revealed that the anomalous coiling is caused by “edge effects”, i.e. the stress relaxation at the rims of thin films. A comprehensive description of the new effects is given in this thesis. The other important aim of this thesis is to characterize physical properties of Si-based rolled-up micro-/nanostructures for potential applications. Both electrical and mechanical properties of freestanding SiGe/Si microtubes are investigated. The high conductivity of boron doped SiGe/Si microtubes is confirmed by two-probe I-V measurements. The bending stiffness and mechanical instability of individual SiGe/Si mcirotubes are probed by atomic force microscopy (AFM) and nanorobotic manipulation. Eventually, nanorobotic manipulation was successfully applied for the characterization of mechanical properties of other 3D micro-/nanostructures such as helices, spirals and rings. Our experimental results revealed that the as-fabricated micro-/nanostructures are elastic, robust, and stable in mechanics, and that the new approach based on nanorobotic manipulation is a promising technique for mechanical properties characterization of these rolled-up 3-D structures.

Nomenclature

Symbol	Description
α	lattice constant
A	cross section area of a tube
C_{11}, C_{12},C_{44}	elastic coefficient
d	diameter
E	Young’s modulus
E_1, E_2	Young’s modulus with respect to layer 1 and layer 2
E_{Si}, E_{SiGe}, E_{Cr}	Young’s modulus with respect to Si, SiGe and Cr
f_s	shape factor
F	internal force due to misfit strain
$F_{[100]}$, $F_{[010]}$, $F_{[hk0]}$	internal force with respect to [100], [010] and [hk0]
G	shear modulus
h_1, h_2	thickness with respect to layer 1 and layer 2
H	deflecting of tube
H_B	deflecting of tube due to bending
H_S	deflecting of tube due to shearing
I	moment of inertia
I_{Si}, I_{SiGe}	moment of inertia with respect to Si and SiGe layer
J_a, J_b	current density with respect to point *a* and *b*
k	spring constant
k_{AFM}	spring constant of an AFM cantilever
k_{beam}	bending stiffness of an ideal seamless tube
k_{tube}	bending stiffness of a rolled-up tube
k_{coil}	spring constant of a coil
l	length of a SiGe/Si bilayer
L	freestanding length of a tube
L_{eff}	effective length of a tube
L_s	shortest contact spacing
L_t	total length of a tube
ΔL	shorten length of a tube under compression load
M	bending moment
N_{stiff}	slope of the photodiode signal vs. AFM tip displacement curve on a stiff surface
N_{tube}	slope of the photodiode signal vs. AFM tip displacement curve on the free end of the freestanding tube
p	pitch of a helix
p_{Si}, p_{SiGe}	doping level with respect to Si and SiGe layer
P	load
P_{cr}	critical load
q	unit of electric charging
R	curvature radius
R_c	contact resistance

R_{Si}, R_{SiGe}	resistance with respect to Si and SiGe layer
$R_{SiGe/Si}$	resistance of a SiGe/Si bilayer
R_t	total resistance of a SiGe/Si tube
R_{tube}	resistance of a SiGe/Si tube
S_{tube}	contact spacing of a SiGe/Si tube
S_{helix}	spacing between each turn of a helix
t	thickness of a tube
w	width of a stripe
x	Ge concentration in SiGe
$\delta_{[100]}$, $\delta_{[010]}$	internal stress with respect to [100] and [010]
δ_{cr}	critical stress
ε	misfit strain
$\Delta\varepsilon$	lattice mismatch of SiGe and Si
κ	curvature
μ	mobility of holes
μ_{Si}, μ_{SiGe}	mobility with respect to hole carriers in Si and SiGe layer
ν	Poisson ratio
$\nu_{<100>}$, $\nu_{<110>}$	Poisson ratio with respect to <100> and <110> direction
ν_{Si}	Poisson ratio of silicon
θ	helicity angle
ϕ	misalignment angle to <110>
ρ	resistivity
σ	conductivity
σ_{tube}	conductivity of a SiGe/Si tube
$\sigma_{SiGe/Si}$	conductivity of a SiGe/Si bilayer

Table of contents

Chapter 1

Introduction

For more than a decade, enormous efforts have been made to miniaturize devices in micro- or nanometer scale because of the promising of the unique physical properties and new potential applications. In general, there are two possible approaches to realize it, i.e. “top down” and “bottom up” strategies. The “top down” approach involves thin film deposition, lithographic patterning and selective etching technologies to fabricate small devices started from bulk materials. It is noticed that the “top down” strategy becomes increasingly challenging when the dimensions of the target structures approach nanometer scale [1]. Moreover, it is a daunting task to fabricate three-dimensional (3D) nanostructures such as nanotubes or nanohelices by “top down” approach in which conventional deposition, etching and lithographic techniques are inherently only two-dimensional (2D) [2, 3]. Thus, over the past few decades, many scientists in the world were exploiting the “bottom up” approach to realize nanostructures. The “bottom up” approach, in contrast to “top down” strategy, builds complex systems by the assembly of atoms or molecules. The “bottom up” approach often uses chemical synthesis, much like the way of nature to construct complex biological system from protein and other macromolecules [4]. Up to now lots of fascinating nanostructures have been achieved via the “bottom up” strategy such as prominent low-dimensional quantum dots [5], carbon nanotubes [6-8], semiconductor nanowires [9, 10], nanobelts of semiconductor oxides [11] and even more complicated three-dimensional twisted helical structures from nanotubes [12], nanowires [13] and nanobelts [14, 15]. These nanostructures are predicted to have considerable potential for manufacturing new building blocks in nanoelectronics, nanomechanics and micro-/nano-electromechanical system (MEMS/NEMS) [16-20]. However, “self-assembly” is still a distant goal for the “bottom up” nanofabrication [21]. In most cases, the size, shape or structure of the as-synthesized nanostructures are not fully controllable.

Recently, by combination of the “top down” and “bottom up” approaches, a new strategy to fabricate 3D structures named self-scrolling technique has been introduced by Prinz et al. in 1999 [22]. This method is based on the coiling up of strained 2D thin films to generate 3D structures, an element of self-assembly, after they detached from the substrate by selective etching. In this process lithographic patterning is employed to define the shape and position of thin films as wanted. Using this self-scrolling technique, some III-V compound semiconductor nanotubes and helices were successfully produced [22]. The diameter of nanotube has a proportional dependence on the wall thickness of the tube and a reciprocal value of the lattice mismatch between the semiconductor bilayers [23]. The inner diameter of such a rolled-up nanotube can be as small as 2nm when its wall contains only two atomic monolayers (1ML GaAs and 1ML InAs) [23]. Compared with carbon nanotubes [7, 8], the rolled-up semiconductor nanotubes provide custom design in diameter, wall thickness and length. Scientists anticipated that this technique can be used for a wide range of possible materials, such as insulators and metals, to integrate them into rolled-up nanotubes [24, 25]. It is believed that these novel semiconductor, metal-semiconductor (MS) and metal-insulator-semiconductor (MIS) rolled-up micro-/nanostructures have a huge potential for various applications in physics, electrical engineering, mechanics and biology due to obvious advantages of the controllable way in design and fabrication. Among these materials, Si or SiGe based materials appear to be particularly suitable for these wide potential applications, since they have good mechanical strength and the compatibility with modern sophisticated CMOS technology. Although the related work was recently introduced in SiGe/Si semiconductor bilayers or SiGe/Si/Cr hybrid systems [26, 27], the studies in this subject are preliminary and quite a few important issues have not been figured out yet. For instance, SiGe/Si helical structures were observed once from coiled-up semiconductor bilayers [23, 26], but few investigations on controllable fabrication were reported. In contrast to rolled-up micro-/nanotubes, helical structures are geometrically more complicated, in which more parameters, such as chirality, helicity angle, pitch of helix, should be taken into account in their designing and fabrication. Furthermore, in order to fabricate delicate nanodevices for NEMS, the dimensions of the designed mesa structures for the formation of 3D shells have to be reduced from micrometer to nanometer scale. It is expected that when the thin films are patterned in such a small size, new effects different from the behavior of bulk crystal may occur to dominate the scrolling process.

Therefore, a main purpose of this PhD dissertation is to seek the method and principle of how to scale down the novel 3D micro-/nanostructures in a better controllable way, especially for the nanostructures that have rarely been exploited before. The ultimate goal of this research is to produce useful devices exactly as designed ones for specific MEMS/NEMS applications. Started from the investigation of scrolling SiGe/Si structures in a micrometer scale, which is fundamental for the further research in this field, we have controllably fabricated two different 3D structures, i.e. tubes and helices, from patterned SiGe/Si bilayers and SiGe/Si/Cr multi-layers. Based on our experimental results, the scrolling principles to form Si based tubes and helices from 2D micrometer scale strained thin films are well developed [28-31]. Furthermore, special attention is paid to find new phenomena and behaviors of the 3D nanostructures when the designed pattern of the strained thin films is scaled down to nanometer size. An anomalous coiling of the strained thin films has been identified, which could not be interpreted by common principles adopted for rolling-up of the mesa-structures in micrometer scale. The followed intensive investigations have revealed that the anomalous coiling is caused by “edge effects”, i.e. the stress relaxation at the rims of thin films. A comprehensive description of the new effects is given in this thesis. These “edge effects” have provided additional freedom in the designing of new 3D nanostructures for more realistic NEMS devices [32, 33].

In addition, it is still premature to judge the impact of 3D micro-/nanostructures on potential applications before their physical properties are evaluated, though scientists expect they are versatile. For instance, it is predicted that micro-/nanotubes can act as nanotweezers, microscopy tips, supporting rods, nanocables [25], very fine injection micro-/nanoneedles, and conducting nanotubes with two-dimensional electron gas (2DEG) for specific investigations [22]. Nanohelices may be used as components of MEMS/NEMS such as nanosprings, electro-megnetic nanocoils, bio-chemical sensors and so on. Thus, another important aim of this thesis is to characterize physical properties of Si-based rolled-up micro-/nanostructures for potential applications. Both electrical and mechanical properties of freestanding SiGe/Si microtubes are investigated. The high conductivity of boron doped SiGe/Si microtubes is confirmed by two-probe I-V measurements. The bending stiffness and mechanical instability of individual SiGe/Si mcirotubes are probed by atomic force microscopy (AFM) and nanorobotic manipulation

[34]. Eventually, nanorobotic manipulation was successfully applied for the characterization of mechanical properties of other 3D micro-/nanostructures such as helices, spirals and rings [32, 35]. Our experimental results revealed that the as-fabricated micro-/nanostructures are elastic, robust, and stable in mechanics, and that the new approach based on nanorobotic manipulation is a promising technique for mechanical properties characterization of these rolled-up 3-D structures.

Chapter 2

Theoretical concepts of the self-scrolling technique

The self-scrolling technique is based on stress relaxation of strained thin films. In detail, the films are patterned by lithography which has an ability to put the designed structures precisely on a substrate at the position where they are needed; when the films detached from the substrate, they roll themselves up into 3D structures due to the stress relaxation. A wide range of possible materials can be used for this technique – calling only for appropriate deposition, a selective etchant and a certain mount of elasticity in the thin films [25]. This technique is adopted for the rolling-up of 3D micro- and nano-structures composed of SiGe/Si, Si/Cr bilayers and SiGe/Si/Cr stacked tri-layers in this thesis work. In this chapter, the bending mechanism of strained films is presented, and the curvature estimation models of the coiled bilayers are also discussed.

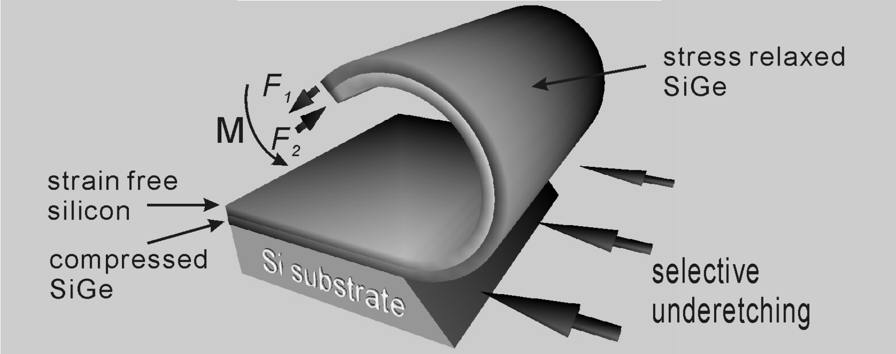

Figure 2.1: Schematic drawing of the self-scrolling process. F_1 *and* F_2 *are the forces in SiGe and Si films, respectively. The former force (*F_1*) is induced by the compressed SiGe film. When the stress relaxation occurs in the compressed SiGe layer, to minimize the total strain energy, the latter force* F_2 *in Si layer and the bending moment M for the SiGe/Si bilayers are induced simultaneously.*

2.1 Self-scrolling mechanism of the strained thin films

The self-scrolling of strained films is caused by the bending moment in the strained films. For a SiGe/Si heterostructure epitaxially grown on a Si substrate, it is composed of an unstrained Si layer and a compressively strained SiGe layer. When the SiGe/Si bilayer is detached from the substrate, the compressive force F_1 in the SiGe layer is turned to be relaxed, which initiates the coiling of the bilayer. The stress relaxation of the SiGe layer induces a counterpart tensile stress, the force F_2, in the parallel connected Si layer. The pair of the opposite forces (F_1 and F_2) will generate a bending moment M to coil the SiGe/Si bilayer, as shown schematically in figure 2.1.

To fabricate rolled-up structures from a Si/Cr bilayer, after the epitaxial growth of a Si layer on Si substrate, a thin Cr layer is deposited on the top Si layer by thermal evaporation. For such a Si/Cr bilayer grown on the Si substrate, the Si layer is unstrained and the as-deposited Cr layer is under tensile stress [36, 37]. The principle of the coiling process is similar to the SiGe/Si bilayer, but the driving force comes from the stressed metal layer. In order to selectively etch Si substrate, the epitaxially grown SiGe and Si layers are heavily doped with boron $(>10^{20}\,cm^{-3})$ while the substrate keeps a very low doping level $\left(\leq 10^{14}\,cm^{-3}\right)$. The details of the selective wet etching are presented in chapter 3 (section 3.4.2). In addition, SiGe/Si/Cr stacked tri-layers can be considered as a combination of above two different bilayers, i.e. SiGe/Si and Si/Cr, in which the SiGe layer is compressed whereas the Cr layer is stretched. When they detached from the substrate, the composed forces from SiGe and Cr layer give rise to the bending moment scrolling the stack of strained films. The contribution of the bending moment depends on the thickness of SiGe and Cr layers, whereas the Si layer will be stretched during coiling.

2.2 Radius estimation models

To the best of author's knowledge, Stoney is the first person to analyze the residual stress and bending curvature of bilayer structures consisting of a film and a substrate [38], by assuming that the film thickness is infinitesimal compared with that of substrate. In 1925, Timoshenko improved the solution for the bilayer structure, in which the film thickness cannot be ignored [39]. The original work was applied to analyze the bending curvature of bi-metal thermostats using force and moment balance theory. Based on Timoshenko's method, an analytical model is developed by Tsui and Clyne [40, 41] in 1997 for predicting residual stresses of deposited coatings on a substrate and the stress-induced curvature of radius. Here we start from the Tsui and Clyne's analysis and then show how to apply it for the estimate the radius of rolled-up Si-based bilayer structures, such as SiGe/Si bilayers.

Tsui and Clyne developed the curvature estimation model for a plate consisting of a pair of layers bonded together, which has a width of b and a misfit of $\Delta\varepsilon$ in the x direction as shown in figure 2.2 [40, 41]. The misfit strain is replaced by using two equal and opposite forces $+F$ and $-F$ (see figure 2.2c) which will induce a bending moment M. Curvature of the plate is generated to balance the bending moment (see figure 2.2e). By applying the simple beam bending theory, the curvature of a beam κ can be expressed as the bending moment (M) divided by the bending stiffness (Σ) of the plate [42]:

$$\kappa = \frac{M}{\Sigma} \qquad (2.1)$$

in which

$$M = F\left(\frac{h_1 + h_2}{2}\right) \qquad (2.2)$$

In Eq. (2.2) h_1 and h_2 are the thickness of the layer 1 and 2, respectively, as shown in figure 2.2b. The misfit strain is a function of force F:

$$\Delta\varepsilon = \frac{F}{h_1 b E_1} + \frac{F}{h_2 b E_2} \quad \Rightarrow \quad F = \Delta\varepsilon \cdot b\left(\frac{h_1 E_1 h_2 E_2}{h_1 E_1 + h_2 E_2}\right) \qquad (2.3)$$

The bending stiffness Σ is given by

$$\Sigma = b\int_{-h_1 - y_c}^{h_2 - y_c} E(y) y^2 dy = bE_2 h_2\left(\frac{h_2^2}{3} - h_2 y_c + y_c^2\right) + bE_1 h_1\left(\frac{h_1^2}{3} + h_1 y_c + y_c^2\right) \qquad (2.4)$$

where E_1 and E_2 are the Young's moduli of layer 1 and layer 2, respectively, y_c and y are the distances from the neutral axis to the bilayer interface (y=0) and to an arbitrary plane in the curved plate, respectively, as shown in figure 2.2(g). The value of y_c is

$$y_c = \frac{h_2^2 E_2 - h_1^2 E_1}{2(h_2 E_2 + h_1 E_1)} \qquad (2.5)$$

Combination of Eqs. (2.1-5) leads to a formula for the radius R arising from the residual stress in the bilayer:

$$R = \frac{1}{\kappa} = \frac{\left(\frac{E_1}{E_2}\right) h_1^4 + 4h_1^3 h_2 + 6h_1^2 h_2^2 + 4h_1 h_2^3 + \left(\frac{E_2}{E_1}\right) h_2^4}{6(h_1 + h_2) h_1 h_2 \Delta\varepsilon} \qquad (2.6)$$

On consideration of biaxial stress in the plate ($\delta_x=\delta_z$ and $\delta_y=0$), δ_z will induce a strain in the *x*-axis due to the Poisson effect [40, 41]. According to Hook's law, the total strain in the *x* axis is

$$\varepsilon_x E = \delta_x - \nu(\delta_y + \delta_z) = \delta_x(1-\nu) \qquad (2.7)$$

Thus the effective Young's modulus *E'* should be applied instead of *E* in Eqs. (2.1-2.6) and

$$E' = \frac{\delta_x}{\varepsilon_x} = \frac{E}{1-\nu} \qquad (2.8)$$

$$\Rightarrow E_1' = \frac{E_1}{1-\nu_1} \text{ and } E_2' = \frac{E_2}{1-\nu_2} \qquad (2.9)$$

in which v_1 and v_2 are the Poisson ratios of the layer 1 and 2, respectively.

Using SiGe/Si bilayer as an example, the misfit strain here is the lattice mismatch between the SiGe layer and the Si layer:

$$\Delta\varepsilon = \frac{a_{SiGe} - a_{Si}}{a_{Si}} \qquad (2.10)$$

in which a_{SiGe} and a_{Si} are the lattice constants of SiGe and Si, respectively . For a $\mathrm{Si}_{(1-x)}\mathrm{Ge}_x$ material with Ge concentration of *x*, the lattice constant a_{SiGe} can be calculated by

$$a_{SiGe} = a_{Si}(1-x) + a_{Ge} \cdot x \qquad (2.11)$$

Assuming SiGe and Si layer are layer 1 and layer 2, respectively, since the Poisson ratios of Si and Ge are very close to each other [43], e.g. $\nu_{\mathrm{Si}<100>}=0.27$ and $\nu_{\mathrm{Ge}<100>}=0.26$, i.e. $E_1'/E_2' \approx E_1/E_2$, Eq. (2.6) is still valid for the radius estimation of SiGe/Si bilayers.

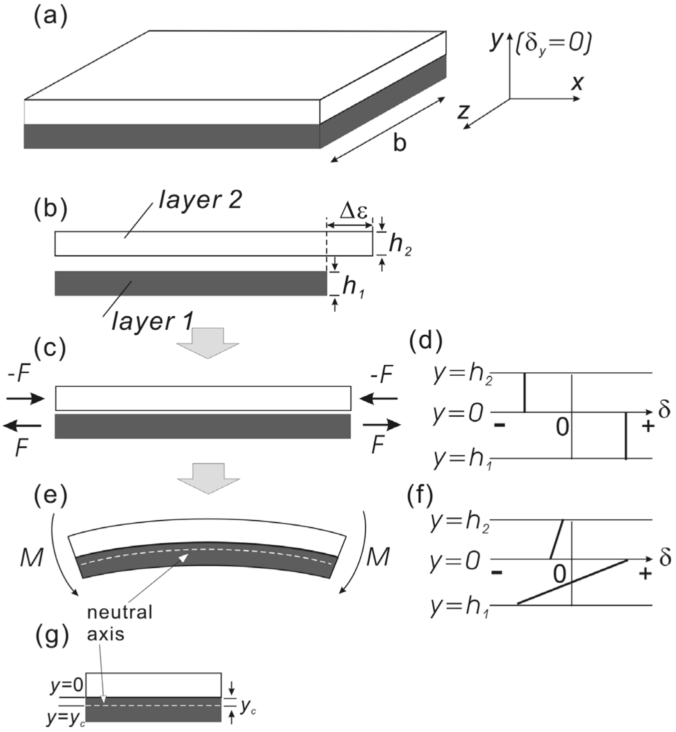

Figure 2.2: Schematic drawing of the generation of curvature in a flat 2-D bilayer resulted from the misfit strain Δε. (a) The bi-layer plate has a width of b. (b) The stress-free condition. (c) Bi-films are constrained by forces (F and –F) in order to have the same sizes. (d) The stress distribution in the plate before bending. (e) Bending moment is generated by the pair of forces (F and –F) which will induce bending of the plate. (f) The stress contribution in the bilayer after bending. (g) The cross section of the bilayer after bending. (after Clyne [40])

In 2003, Grundmann developed a model for the strain relaxation in nanotubes made up from semiconductor bilayers using the continuum elasticity theory [44]. He assumed that the cylindrically rolled structure, e.g. a tube, is formed, in which the stress is relaxed along the radial axis *r*. The according strains in the tangential (*t*), cylindrical (*y*) and radial (*r*) axis are ε_r, ε_y and ε_r, respectively.

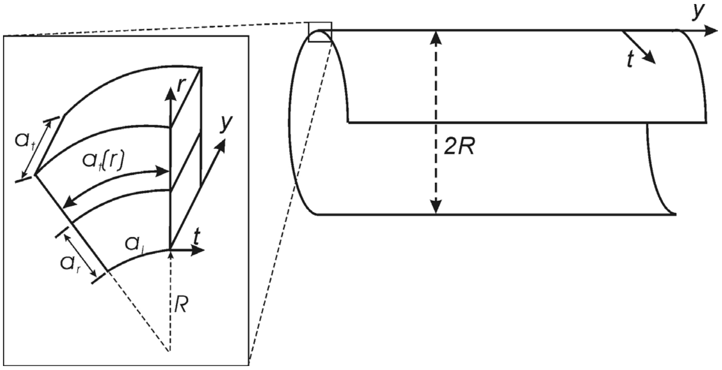

Figure 2.3: Schematic drawing of a rolled-up tube. The tube axis is along y-direction, the radial direction is r-axis, and the t-axis represents the tangential direction of the tube.

If a_y and a_0 are the strained and unstrained lattice constants of the film respectively, thus, $\varepsilon_y=(a_y-a_0)/a_0$; for a radius R in the inner surface of the cylinder, in the tangential axis the lattice constant and the strain depending on the radial coordinate (r) are expressed as:

$$a_t(r)=a_i\left(1+\frac{r}{R}\right) \qquad (2.12)$$

and

$$\varepsilon_t(r)=\frac{a_t(r)-a_0}{a_0} \qquad (2.13),$$

in which a_i is the lattice constant at the inner surface of the cylinder as shown in inset of figure 2.3. The strain energy density is given by [44]

$$E_v=\frac{E}{2(v^2-1)}\left(\varepsilon_t^2+\varepsilon_y^2+2v\varepsilon_t\varepsilon_y\right) \qquad (2.14)$$

Thus, E_v is a function of a_i, R and r. Then, the total strain energy in a strained thin film with a layer thickness of d is

$$E_{tot}(a_i,a_y,R)=\int_0^d E_v(a_i,a_y,R,r)dr \qquad (2.15)$$

For an isotropic bilayer system, assuming the Young's modulus in the outer layer (layer 1) and the inner layer (layer 2) are E_1 and E_2 respectively, and the layer thicknesses are h_1 and h_2 respectively, the total strain energy (E_{tot}) summed up from the strain energy of bi-films is [45]

$$E_{tot}(a_i,a_y,R)=\int_0^{h_1} E_{v(layer1)}dr+\int_{h_1}^{h_1+h_2} E_{v(layer2)}dr \qquad (2.16)$$

Since E_{tot} is a function of a_i, a_y and R, we need three boundary conditions to solve the radius R. When the strain state is in equilibrium, we have:

$$\frac{\partial E_{tot}}{\partial a_i} = 0 \qquad (2.17)$$

$$\frac{\partial E_{tot}}{\partial a_y} = 0 \qquad (2.18)$$

$$\frac{\partial E_{tot}}{\partial R} = 0 \qquad (2.19)$$

Thus, the resulting radius R of such two isotropic layers with lattice mismatch $\Delta\varepsilon$ and the same Poisson ratio ν worked out as [44]:

$$R = \frac{E_1^2 h_1^4 + 4E_1E_2h_1^3h_2 + 6E_1E_2h_1^2h_2^2 + 4E_1E_2h_1h_2^3 + E_2^2h_2^4}{6\Delta\varepsilon E_1 E_2 (1+\nu) h_1 h_2 (h_1 + h_2)} \qquad (2.20)$$

In contrast to the estimation equation from Tsui and Clyne, i.e. Eq. (2.6), this equation has an extra term of $(1+\nu)$.

2.3 Energetically favorable scrolling direction

For semiconductor materials with a diamond structure such as Si and SiGe, if the Si or SiGe film scrolling along <100>, the strain energy is then given by [44]

$$E_{100}(\varepsilon_t, \varepsilon_y) = \frac{C_{11} - C_{12}}{2C_{11}}\left[C_{11}(\varepsilon_t + \varepsilon_y)^2 + C_{12}(\varepsilon_t^2 + \varepsilon_y^2)\right] \qquad (2.21)$$

in which C_{11}, C_{12} are the elastic coefficients, their values for Si and Ge are shown in table 2.1. When the (001) oriented film rolled up along <*hk0*> deviated an angle of ϕ from the <100> direction, the strain energy can be expressed as [44]

$$E_\phi(\varepsilon_t, \varepsilon_y) = E_{100}(\varepsilon_t, \varepsilon_y) + (2C_{44} - C_{11} + C_{12})\left(\frac{\varepsilon_t - \varepsilon_y}{2}\right)^2 \sin^2(2\phi). \qquad (2.22)$$

Since $(2C_{44} - C_{11} + C_{12})\left(\frac{\varepsilon_t - \varepsilon_y}{2}\right)^2 \sin^2(2\phi) > 0$, films scrolling along <100> should have the smallest strain energy, thus it is the energetically favorable direction for bending of anisotropic films.

Table 2.1: Some related elastic coefficient values of Si and $Si_{1-x}Ge_x$ crystals [43, 46]

	C_{11} (GPa)	C_{12} (GPa)	C_{44} (GPa)	$2C_{44}+C_{12}-C_{11}$ (GPa)
Si	166	64	80	58
$Si_{1-x}Ge_x$	$165.8 - 37.3x$	$63.9 - 15.6x$	$79.6 - 12.8x$	$57.3 - 3.9x$

Chapter 3

Micro- and nanofabrication methods

To fabricate Si based 3-D micro-/nanostructures using self-scrolling technique, thin film deposition, lithography, etching and drying techniques are required. This chapter only describes the main processes in the fabrication sequence, more general introduction and detailed descriptions can be found in the literatures of modern Si technology [47] and fundamentals of micro-/nanofabrication [48].

3.1 UHV CVD epitaxial growth

The first step in fabrication of SiGe/Si rolled-up 3-D structures is epitaxial growth of SiGe/Si bilayers on a Si substrate, while for Si/Cr 3-D structures a Si layer is grown instead of SiGe/Si bilayers. In this work, ultrahigh vacuum chemical vapor deposition (UHV CVD) has been employed in the epitaxial growth of above Si and SiGe thin films. Comparing with molecular beam epitaxy (MBE), the main advantage of CVD is that it is possible for large scale production. In our UHV CVD system, a batch of 4-inch Si wafers (maximum 24 pieces) can be mounted vertically in a quartz wafer boat, which can be transferred on a rail between the load lock and the reaction chamber in the CVD system. A schematic illustration (see figure 3.1) shows a geometrical arrangement of the CVD reaction chamber.

For the preparation of silicon substrate before epitaxial growth, a 4-inch low-boron-doped (doping level $< 10^{14} cm^{-3}$) Si wafer is cleaned in the following procedures: firstly, the wafer is dipped into a Caros solution (H_2SO_4:H_2O_2 = 2:1) for 10 minutes at 90 ^{o}C to remove organic contamination on the surface; then the wafer is rinsed in a quick dump rinser by deionized water until the resistance of the rinsed water reaches 13 MΩ, so that the residual ions from Caros solution are removed completely; finally the Si wafer is dipped in a diluted aqueous hydrofluoric acid solution (5% HF) for 2 minutes at room temperature to etch away the native oxide and to passivate the dangling Si bonds at the surface with an adlayer of hydrogen [49].

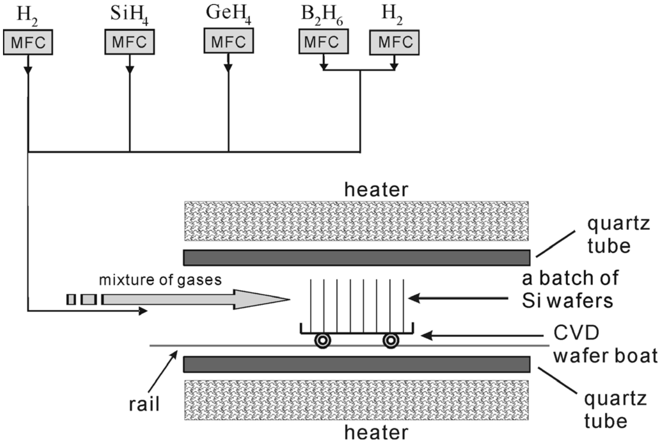

Figure 3.1: Schematic drawing of the reaction chamber of the UHV CVD system, in which a quartz boat is loaded with Si wafer vertically. The reaction chamber is made of a quartz tube covered by heater. Four different gas species, i.e. hydrogen (H_2), silane (SiH_4), germane (GeH_4) and diborane (B_2H_6) are connected to the reactive chamber. The flow rate of each gas is controlled by mass flow controllers (MFC).

After cleaning, the Si wafer is mounted in a CVD wafer boat and then placed into the load lock of the UHV CVD system immediately to avoid the reoxidation of the surface. When the pressure of the load lock is pumped down to lower than $5x10^{-7}$ mbar, the substrate is transferred, under a hydrogen flow, into the reaction chamber of the CVD system which was maintained at 550°C by a heater. Afterward, a Si buffer layer is grown by flowing the mixture of silane (SiH_4) and hydrogen (H_2) gases in the reactor for 1 hour. Sufficient long growth time of the Si buffer layer will guarantee the Si wafer reaching a constant temperature, i.e. 550°C, in the reactor. Then, the epitaxial SiGe and Si layers with the Si layer on the top, are to be successively grown on the Si buffer. Since the lattice constant of SiGe alloy is larger than that of Si, there exists a maximum thickness, a so-called critical thickness, for the epitaxial layer. Beyond this thickness, it costs too much energy to strain additional layers into coherence with the Si substrate and misfit dislocations will form at the interface of the heterostructure [50]. The solid line in figure 3.2 shows the relation between the critical thickness of SiGe layer and the Ge concentration on Si (001) substrate [50] based on the mechanical equilibrium model from Matthews and Blakeslee [51]. It shows clearly that the critical thickness of the epitaxial SiGe layer decreases with the increase of Ge concentration. Bean *et al*. also demonstrated that the defect free films much thicker than the equilibrium thickness could be grown at 550 °C by MBE [52]. In our experiments, the thickness of the deposited SiGe layer is always smaller than the critical thickness indicated by Bean *et al.* results [52] to avoid stress relaxation in the grown SiGe/Si bilayers.

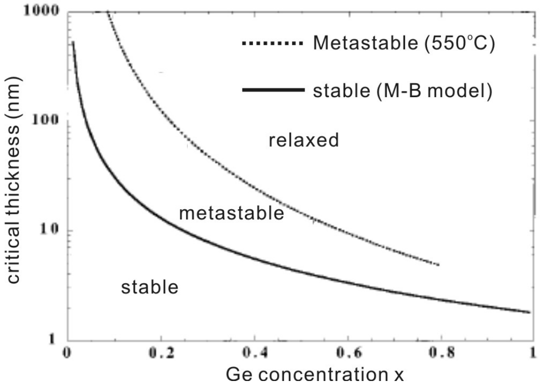

Figure 3.2: The relation between critical thickness and Ge concentration of $Si_{1-x}Ge_x$ layer grown on Si (001) substrate. M-B model means Matthews and Blakeslee model [51].

A gas-phase mixture of silane (SiH_4), diborane (B_2H_6) and hydrogen (H_2) is used during the epitaxial growth of p-type Si layer, in which B_2H_6 gas molecules are used for the p-type doping and H_2 is used as carrier gas. To epitaxially grow p-type SiGe layer, germane (GeH_4) gas is mixed into SiH_4, B_2H_6 and H_2 ambience as a germanium (Ge) source. When the growth process of SiGe/Si bilayer is finished, the gas flow is terminated and the wafer boat is transferred back to the load lock chamber of the CVD system. The layer thickness and the Ge concentration in SiGe layer are calibrated by transmission electron microscopy (TEM) and X-ray diffraction (XRD). A typical TEM bright field image of our calibration sample with ten periods of $Si_{1-x}Ge_x$/Si (x = 23%) quantum well structure is shown in figure 3.3, in which the SiGe layers show a darker contrast than the Si layers and the interfaces are smooth. The high resolution electron microscope image (inset of figure 3.3) indicates that the lattice is continuous in their interfaces and no misfit dislocation along the interfaces could be observed. It also implies that the stress in the SiGe/Si bilayers arising from the lattice misfit is kept in this structure. The Si layers including the top one are unstrained because the epitaxial growth is based on a Si substrate. Figure 3.4 shows a typical X-ray diffraction (XRD) experimental spectrum and the simulation curve of the SiGe/Si ten periods quantum wells specimen (see figure 3.3), they fit to each other well. From this XRD analysis SiGe/Si bilayers with thickness of 4.7 nm/6.8 nm respectively and 23% of Ge concentration in SiGe layers are estimated. Based on TEM and XRD experiments, a curve is drawn (figure 3.5) for the dependence of growth rate on the Ge concentration of SiGe layer. This curve shows that the growth rate of the SiGe film first increases rapidly with the increase of Ge concentration when the Ge concentration is relatively low, while it becomes flat gradually after the Ge concentration reaches 30-40%.

To determine the doping level in the SiGe/Si bilayers, Hall measurement was employed using van der Pauw method [53]. For the Hall measurement, a sample of 230 nm thick boron-doped Si layer and a sample of 60 nm thick boron-doped SiGe with the same growth condition as SiGe/Si bilayer were prepared separately on Si (001) substrates. Four aluminium point contacts with 200 nm thickness were evaporated on the samples' surface in van der Pauw geometry [53] through a mask, then the samples with aluminium contacts were annealed at 400 ºC for 2 minutes in a gas mixture of nitrogen (N_2) and hydrogen (H_2). Finally, the samples were glued into a chip holder for Hall measurement. The experiment results show that the boron-doping levels of both SiGe and Si layers are higher than $2 \cdot 10^{20}$ cm^{-3} ($p_{SiGe} = 4.57 \cdot 10^{20} cm^{-3}$, $p_{Si} = 2.03 \cdot 10^{20} cm^{-3}$) at room temperature (300K).

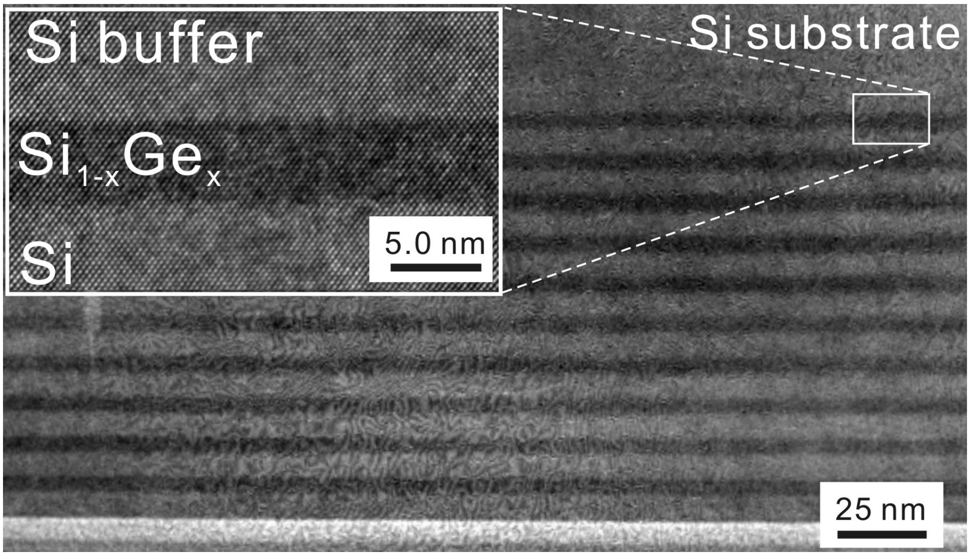

Figure 3.3: TEM image of a calibration sample with 10 SiGe/Si periods quantum wells, showing the epitaxially grown layers and the smooth interfaces between the layers. The inset shows that no misfit dislocation is observed in the interface.

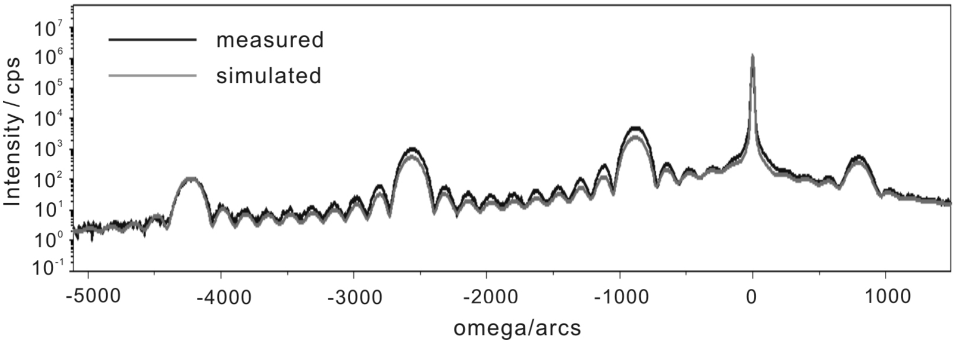

Figure 3.4: Determination of Ge concentration in SiGe layer and Si, SiGe layers thickness by X-ray diffraction (XRD) with of 10 periods of SiGe/Si bilayers structure as shown in figure 3.3. The measured signals correspond to the (004) reflection and the simulation result is calculated from 10 periods of SiGe/Si bilayers with thickness of 4.7 nm/6.8 nm respectively and 23% of Ge concentration in SiGe layers.

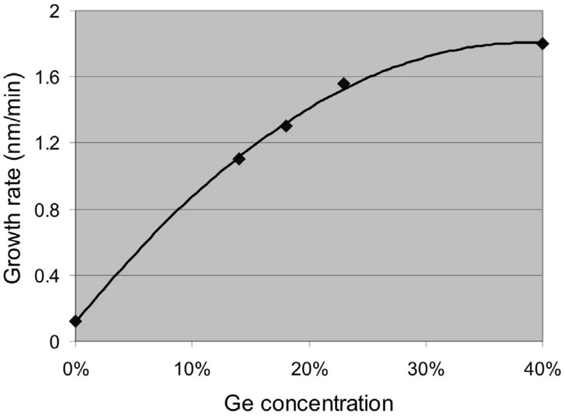

Figure 3.5: SiGe film growth rate as a function of Ge concentration in the film.

3.2 Thermal evaporation of Cr layer

After the epitaxial growth of SiGe/Si bilayer (or a Si layer for Si/Cr bilayer structures), a thin layer of chromium (Cr) is deposited on the sample by thermal evaporation process as a mask layer for electron beam (e-beam) lithography. The deposited Cr layer will generate internal stress in the Si film, thus it also acts as a stressor for SiGe/Si/Cr or Si/Cr metal-semiconductor (MS) hybrid structures. In this Ph D work, a thin Cr layer was deposited by e-beam evaporation using a “Balzers BAK600” equipment. The evaporation is performed in a vacuum chamber at a low pressure (typical $2 \cdot 10^{-7}$ mbar). In order to evaporate Cr on the sample surface, the e-beam is focused on the Cr source which is placed in a crucible. Due to the heating from the e-beam irradiation, Cr atoms will sublimate locally from the source and move straight towards the sample surface. The growth rate of the deposited Cr layer is approximately 3-5 angstrom/second. To improve the uniformity of Cr film in thickness, the sample holder is rotated in the chamber during the evaporation.

For the conductivity measurements of individual SiGe/Si microtubes, different metals, such as aluminum (Al) and Cr, have been used for preparing contacts. The details of the fabrication and measurements for the tube conductivity investigation are provided in chapter 5.

3.3 Lithography

The final shape of a rolled-up 3-D structure strongly depends on the predefinition of the size and shape of 2-D patterned thin films. To achieve flexibility in design of the mesa structures, e-beam lithography and photolithography have been employed. Various shapes of patterns have been investigated, the results and discussion of the relation between the 2-D patterned thin films and the 3-D rolled-up structures are given in the next chapter (chapter 4).

3.3.1 E-beam lithography

The key advantage of e-beam lithography is its high resolution, a pattern size as small as 10 nm is feasible. Contrary to photolithography which just copies designed patterns from a photo-mask, e-beam lithography is a mask-less lithographic technique which allows to write even random pattern designs onto the sample directly. Polymethyl methacrylate (PMMA) is used as a standard high resolution positive resist for e-beam lithography.

In our lithographic treatments, after metal evaporation, a 100 nm thick PMMA layer was spin-coated on the top of the sample. Then the sample is baked on a hotplate at 90°C for 1 minute. Subsequently, the sample is mounted on the sample holder of the e-beam lithography system. The e-beam lithography system in Paul Scherrer Institute is Lion-LV1, which allows different types of data format for a pattern design. The bitmap format is adopted in our experiments for a convenience of design, where one bitmap file for a pattern design consists of 4000 x 4000 pixels. Black or white in a single pixel means this pixel region to be exposed or unexposed, respectively. Each pixel size is defined as 40 nm by the system. According to the designed binary color bitmap file, the e-beam lithography system writes an entire pattern on PMMA coated sample one pixel by another. Thus, for each pattern design, the real exposure area on a sample is a square of 160μm x 160 μm. A group of patterned arrays can be obtained on the sample by programming the e-beam system. After the exposure, all of the samples are developed using a recipe of methylisobutylketone (MIBK) and isopropyl alcohol with a ratio of 1:3 as developer in a HAMATECH (Steag-Hamatech HME 500) developing equipment. Then, the sample is sprayed by pure isopropyl alcohol to stop the development immediately, and dried by high speed spinning in the developing equipment.

3.3.2 Photolithography

Photolithography is an alternative method to make patterns on samples. The main advantage to use photolithography is its possibility for batch fabrication. Usually it takes less than half minute to transfer all patterns from the photo-mask to the photoresist coated 4-inch Si wafer by a single exposure. However, the resolution of the resulting line width in the pattern is usually about half micron. In this work, SHIPLEY MICROPOSIT S1813 photoresist is used for photolithography, its resolution limit is 0.48 μm [54]. After epitaxial growth of SiGe/Si bilayers, ca. 1.3 μm thick photoresist S1813 is spin-coated on the sample directly without metal evaporation, because the photoresist is sufficiently thick to be used as a mask for reactive ion etching. The sample is baked at 120 °C for 1 minute, and then is exposed by a standard mask aligner (Karl Suess MA-6). The exposure process was performed under soft contact mode with an intensity of 10mW/cm^{-2} at a wave length of 365 nm for 4.5 seconds. Subsequently, the exposed sample was developed by rinsing it in developer solution (MICROPOSIT MF 24A) for 20-30 seconds. Finally the sample is rinsed in deionized water and dried by blowing nitrogen gas on the surface.

3.4 Etching

3.4.1 Reactive ion etching

The most important reason to use reactive ion etching (RIE) is the possibility for directional (anisotropic) etching, so that the pattern can be transferred from PMMA or photoresist to the underneath thin films with a precisely controlled size and shape. This directional etching is attributed to the presence of ionic species in the plasma and the electric fields that direct them normal to the sample surface [47]. The etching rate is also highly controllable by tuning the plasma parameters such as gas pressure, voltage bias and power.

In the experiments, three steps of RIE are applied to transfer the pattern from PMMA to SiGe/Si/Cr stacked thin films. In the first step, the pattern was transferred from PMMA into the Cr layer by mixture of Cl_2 and CO_2 gas plasma. Secondly, the top residue PMMA layer is removed by oxygen plasma etching. After that, the patterned Cr layer was used as a mask to transfer the pattern further to the underneath SiGe/Si bilayer using RIE in a SF_6, CHF_3 and O_2 ambience. Figure 3.6 shows a high resolution SEM image of RIE etched mesa line structure, in which the formed vertical side-walls of the mesa confirm the directional etching towards the substrate. To fabricate SiGe/Si 3D structures, in addition, the residual Cr layer on the SiGe/Si/Cr stacked thin films is finally removed by RIE. For samples covered by photoresist directly, the etching steps for patterning Cr layer are skipped.

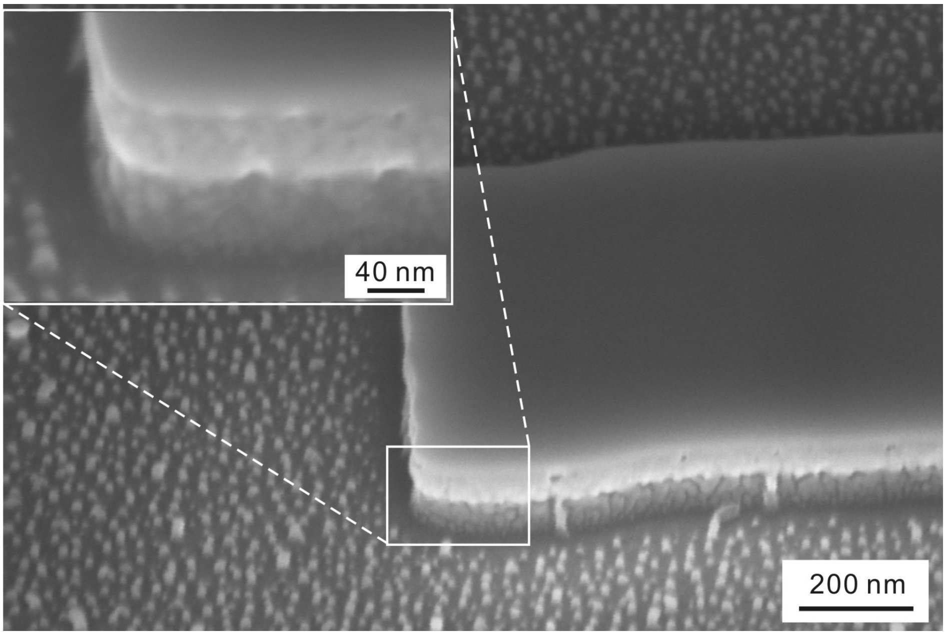

Figure 3.6: SEM image of RIE etched mesa-line structure, showing the etching is dominated in the direction normal to the surface of substrate.

3.4.2 Wet etching

To release the strained thin films, i.e. SiGe/Si, SiGe/Si/Cr and Si/Cr, from the Si substrate (and the undoped Si buffer), wet etching is performed by immersing the sample in a bath of chemical solution. Wet etching can have the possibility for high etching selectivity because it depends on chemistry. The selectivity is defined as the ratio of etching rates between two materials: the etching rate of the faster etching material divided by the etching rate of the lower etching material [55].

Wet chemical etching based on ammonium-hydroxide water ($NH_4OH{\cdot}H_2O$) solution for micromachining monocrystalline silicon was developed recently [56-58]. $NH_4OH{\cdot}H_2O$ shows strong dependence of the etching rate on the crystal orientation with anisotropic behavior similar to that of potassium hydroxide (KOH) and ethylenediamine pyrochatechol water (EPW) which are commonly used for Si micromachining [58]. In contrast to KOH, EPW and other etchants for Si micromachining, $NH_4OH{\cdot}H_2O$ solution fulfills all the following requirements: it does not incorporate alkaline ions which can contaminate CMOS integrated circuits; it is not toxic; and the most important factor is that it gives excellent etching selectivity to heavily boron doped Si and SiGe layers. Schnakenberg et al. reported that the etching rate of highly boron-doped ($1.3{\cdot}10^{20}$ atoms/cm^3) silicon epitaxial layers in 3.7% $NH_4OH{\cdot}H_2O$ at 75 ºC was smaller than 3 nm/h, which corresponds to a selectivity of approximately 8000 [56]. A higher concentration of $NH_4OH{\cdot}H_2O$ (> 3.7%) leads to a significant decrease of ammonia concentration with the etching time due to high volatility, which results in unreliable reproducibility. In SiGe alloys, Ge can be considered as an electrically inactive donor impurity in silicon. Wang et al. reported that, in $NH_4OH{\cdot}H_2O$ at 75ºC, the etching selectivity of SiGe layer with 10% concentration of Ge was better than 80, and it increased with Ge concentration [59]. The mechanism of etching resistance on highly boron doped Si and SiGe alloy is still unclear, but it is suggested that a passivating oxide film is formed due to the heavily doping in silicon [55, 59]. Thus, the selectivity of highly boron doped SiGe layer with Ge concentration larger than 10% can reach higher etching selectivity than that of Si with the same doping level. In addition, metals such as Au, Cr, Ti show excellent stability in $NH_4OH{\cdot}H_2O$ solutions [57]

When the SiGe/Si bilayer (or SiGe/Si/Cr, Si/Cr thin films) is released from Si substrate by dissolving the Si substrate using $NH_4OH{\cdot}H_2O$ solution, the internal stress in the heterostructures tends to relax spontaneously and the bilayer curls themselves to form freestanding 3D micro-/nanostructures.

The surface finish status of the sample after etching process in micromachining is greatly concerned because a smooth surface is essential for the fabrication of MEMS/NEMS [58]. In our work, it has been found that after the RIE process, if the sample surface is not very clean, e.g. the residual photoresist (or PMMA) sticks on the surface, pyramids will form and the surface roughness increases significantly during the wet etching. Figure 3.7 shows that the residual contaminator causes the higher surface roughness of the sample, and that very smooth surface can be obtained from the sample with clean surface before etching.

Therefore, special attention is paid in our experiments to avoid any contaminations on the sample surface before the wet etching.

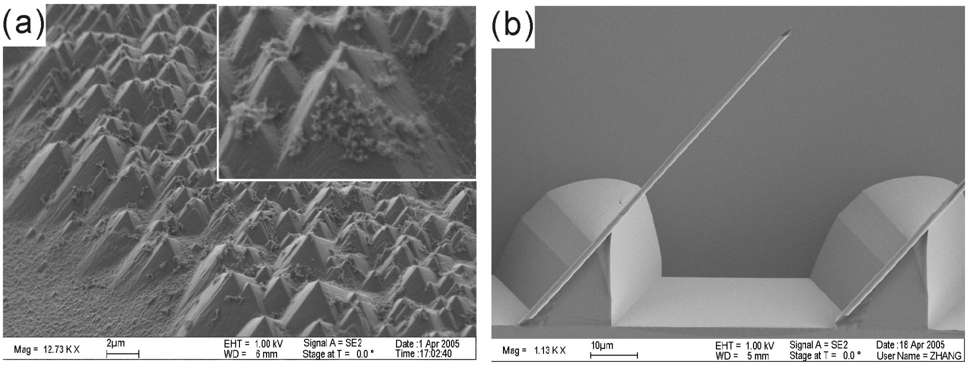

Figure 3.7: SEM images of sample surfaces after wet etching process. (a) Sample has very rough surface due to the residual polymer sticking on the surface after RIE. (b) Very smooth surface can be obtained after the wet etching process, if the sample surface is clean before the wet etching.

3.5 Rinsing and drying

Drying a freestanding 3D micro-/nanostructure in air could drastically deform even destroy the structure due to surface tensions produced by the liquid inside the 3D structures or between the structure and the substrate at the stage when the residual liquid changes into gaseous phase and reduces its volume. Figure 3.8 shows some as-fabricated SiGe/Si microtubes dried in air from water and isopropyl alcohol solution, where the structures were deformed or attached to the substrate by the surface tension. The van der Waals forces and hydrogen bonding may keep it sticking to the substrate strongly, the mechanical force to release it from the substrate is usually large enough to damage the delicate micro-/nanostructures [48]. Thus, it is crucial to decrease or eliminate the surface tension during the drying step.

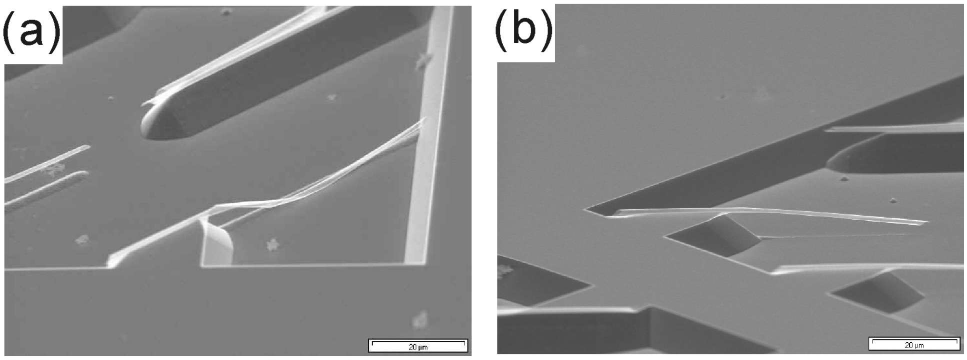

Figure 3.8: SEM images of deformed freestanding microtubes after a drying process affected by surface tension. (a) Sample is dried from water. (b) Sample is dried from isopropyl alcohol.

A simple way to reduce the effect of surface tension is to dry the sample from a just boiling isopropyl alcohol solution. Compared with water, isopropyl alcohol has a relative low surface tension and the boiling isopropyl alcohol evaporates extremely fast, thus the impact time from surface tension is well reduced. The processing steps are as follows: after the freestanding structures have been fabricated in the aqueous NH_4OH solution, the sample is thoroughly rinsed in deionized water and subsequently in isopropyl alcohol; then the sample is dried by removing them carefully out of boiling isopropyl alcohol and placed on a clean-room tissue. Experimental results show that this method is able to increase the yield of resulted devices, however, this method is still not promising for the fabrication of very fine nanostructures such as single turn rolled up nanotubes [60] or nanohelices with only a layer thickness of several nanometers. Therefore, more gentle drying technique is required. One well known method is critical point drying which can eliminate the surface tension completely. Figure 3.9 presents the general phase diagram of a substance such as CO_2; by increasing the pressure and temperature of the substance, it is possible to dry the sample without crossing the phase boundary, i.e. method II in figure 3.9. This is because once the critical point is exceeded, which means in the supercritical region, no distinction exists between liquid and gas, therefore the surface tension disappears.

In the experiments, the sample is immersed in deionized water to stop the etching and then it is placed into a chamber of the critical point dryer equipment (tousimis, Automegasamdri®-915B, Series B) filled with isopropyl alcohol solution. The next drying processes are automatically operated by the equipment: the rinse liquid (isopropyl alcohol) is replaced by liquid CO_2 in the chamber of the critical point dryer; the liquid CO_2 then will be driven into supercritical phase under a pressure of 1100 psi at 35°C and pumped out from the chamber. This supercritical drying method works well in our experiments to avoid the impact of capillary force.

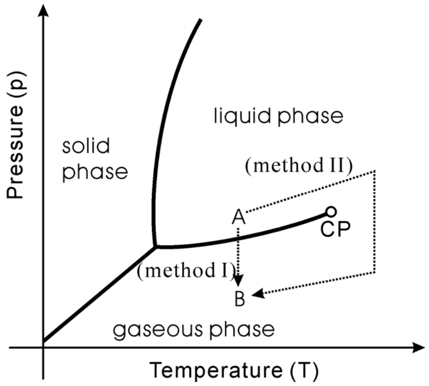

Figure 3.9: If the sample is dried in the air (method I) from a liquid phase to gaseous phase, surface tension will impact the structures of the sample. However, if the sample is dried under a supercritical condition of the liquid (method II), the surface tension disappears. CP means the critical point of the liquid.

3.6 Summary

As a short summary, to fabricate SiGe/Si, SiGe/Si/Cr and Si/Cr 3-D micro-/nanostructures, epitaxial growth of semiconductor thin films, e-beam evaporation of metal layer, lithography, reactive ion etching, selective wet etching and drying processes are performed. Figure 3.10 gives the schematic drawing flowchart for the fabrication of SiGe/Si 3-D structures, the fabrication methods of SiGe/Si/Cr and Si/Cr structure can be easily developed based on this fabrication flow. These fabrication techniques are compatible to the modern Si technology, and the fabrication of rolled-up Si-based 3-D structures is very reproducible and possible for large scale production.

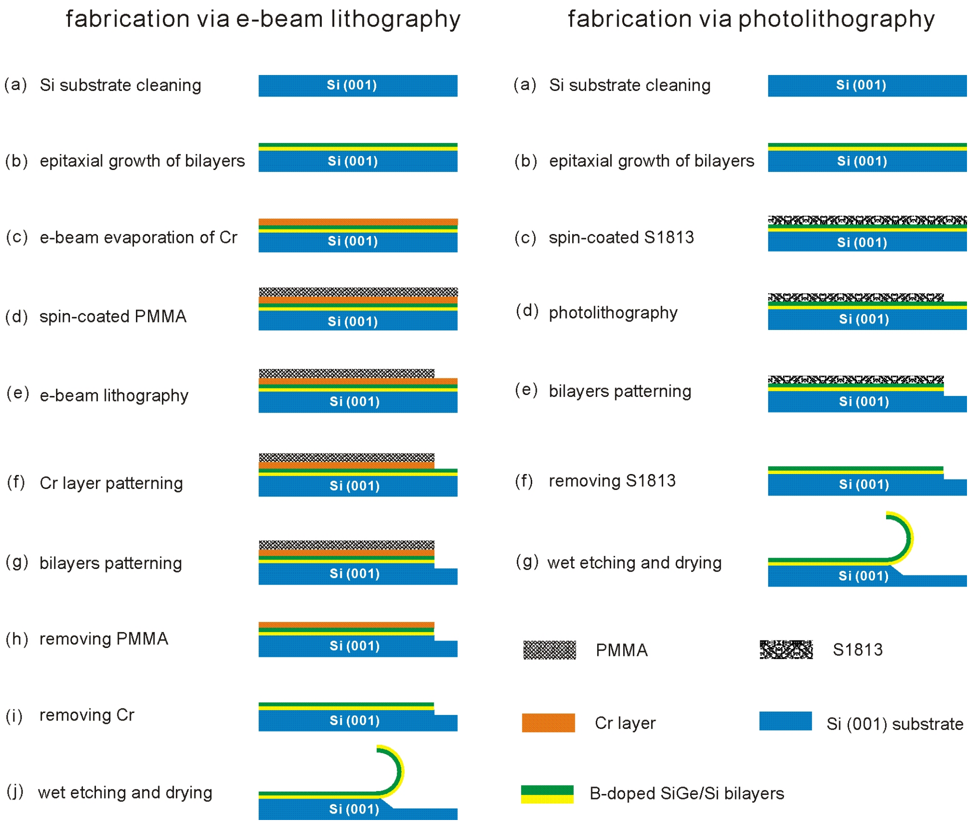

Figure 3.10: The flowchart for fabrication of rolled-up SiGe/Si bilayer structures via e beam lithography (the left column) and photolithography (the right column). To fabricate SiGe/Si/Cr and Si/Cr 3D structures, step (i) is skipped. Moreover, to fabricate Si/Cr 3D structures, only one Si layer is epitaxially grown on the substrate instead of a SiGe/Si bilayer.

Chapter 4

Controllable fabrication of 3-D micro-/nanostructures

In this chapter, a variety of Si-based 3D micro-/nanostructures with different shapes and dimensions have been obtained by controllable fabrication. Started with the fabrication of conventional micro-structures with the mesa pattern in micrometer scale, then the dimension of the designed pattern is further scaled down to nanometer size (<1μm), the scrolling behaviors and rules of the nanostructures fabrication are intensively studied. Especially, the stress relaxation at the rim of mesa lines during the formation of nanostructures has been probed to be responsible for the anomalous coiling of the strained thin films. The achieved flexible design and controllable fabrication of the rolled-up 3D micro-/nanostructures is promising for their applications in MEMS/NEMS devices.

4.1 Scrolling behaviors of tubes and helices in micrometer size

Two types of freestanding 3D micro-structures (tubes and helices) have been fabricated from strained SiGe/Si bilayers and SiGe/Si/Cr film stacks. The tube structure is fabricated on Si (001), (110), and (111) surfaces respectively to investigate the scrolling behavior on different substrates. Also, helical micro-structures with different designs of the mesa stripes have been obtained on Si (001) surfaces, and the factors to influence the geometry of the coils, such as the helical angle, the chiraity and the pitch, have been examined.

4.1.1 As-fabricated microtubes on different Si substrates

4.1.1.1 Microtubes on Si (001) surface

Crystalline Si is an anisotropic material showing different mechanical properties with respect to the crystallographic orientation, for instance, the Young's moduli along <100> and <110> directions on Si (001) substrate are 130.2 GPa and 168.9 GPa, respectively [43]. In chapter 2 (section 2.3), we have shown that according to the strain energy calculation, <100> should be the energetically favourable scrolling direction of Si and SiGe layers. It is understandable that the strained films to form tubes will always trend to scroll themselves along the most compliant scrolling direction, i.e. in the direction having the smallest Young's modulus on the surface [26]. On a Si (001) substrate it is along <100> directions. This regulation is used to direct the scrolling process for fabrication of freestanding tubes on Si (001) substrate. Figure 4.1a schematically shows a mesa structure design of a freestanding tube on the Si (001) surface, where the long sides of the mesa line is parallel to [010] direction [28]. In experiments, the width of the stripe *w* was also increased to fabricate tubes with different numbers of turns. Since there are two equivalent <100> directions on the Si (001) surface, i.e. [100] and [010], which are perpendicular to each other, the scrolling direction of the bilayer is still not uniquely settled. Thus, to better control the initial scrolling direction of the patterned bilayers or multi-layers in a specifically desired <100> direction, anisotropic underetching effect has been utilized by applying a special pattern design in the mesa's tip [28]. Figure 4.1a demonstrates a pattern design conducted for this purpose, where the edge $\overline{BC}$ of the tip is tailored along <110> direction in the pattern to allow the bilayer preferentially rolling first in the [100] direction. During the initial stage of etching, the formed (111) facets at the sidewall under the mesa's tip will retard the underetching in this direction [28], whereas mesa edges $\overline{AB}$ and $\overline{CD}$ oriented along the [010] direction are underetched rapidly. As a result, the strained film has much higher priority to scroll itself along [100] direction than along [010]. Figure 4.1 b-e show field emission scanning electron microscope (FESEM) images of typical as-fabricated freestanding tube structures, in which the initial planar films consist of a SiGe/Si bilayer with a thickness of 11/8 nm, respectively, and about 40% Ge in the SiGe layer. The freestanding length of the two tubes formed from the pre-patterned SiGe/Si bilayers in figure 4.1(c, d) is about 60 μm and 110 μm, respectively. In figure 4.1c it is clearly seen that the as-fabricated tube is very straight and the diameter is uniform from the free end to the fixed end of the tube. Since the bilayers begin coiling from both sides of the mesa stripe simultaneously, i.e. along the opposite [100] and [-100] direction in the case, the width of stripe (*w*) should be appropriately selected for a single freestanding tube fabrication. According to our experimental results, when the width of the stripe *w* is less than that about 1.6 times of the tube circumference, i.e. $1.6\pi d$ (*d* is the diameter of the tube), a single freestanding tube can be fabricated, as shown in figure 4.1b-d. In the case of $w > 1.6\pi d$, a pair of two parallel tubes (“twin tube”) is formed as shown in figure 4.1e. By increasing the width of the mesa line each of the two tubes will contain several turns.

In addition, Si/Cr or SiGe/Si/Cr micro-tubes have also been fabricated on Si (100) surface, and the scrolling direction of these metal-coated films is found as same as that of SiGe/Si bilayers, i.e. in the <100> direction. This phenomenon can be understood that the coated polycrystalline or amorphous Cr layer shows an isotropic Young’s modulus, thus the preferential scrolling direction of the metal-coated films is still determined by the anisotropic nature of the Si layer or SiGe/Si bilayer. Figure 4.1f shows a Si/Cr “twin tube” as an example, in which a rectangular-shaped pattern was applied on Si/Cr hybrid bilayers.

The diameter d ($d=2R$) of tubes formed from the $Si_{1-x}Ge_x$/Si bilayers can be theoretically estimated either by Tsui and Clyne’s calculation (see chapter 2 Eq. 2.6) or by Grundmann’s equation (see chapter 2 Eq. 2.20). In order to compare the experimental diameters with theoretical ones systematically, a series of $Si_{1-x}Ge_x$/Si bilayers with varied Ge concentration (x), $Si_{1-x}Ge_x$ layer thickness (h_1) and Si layer thickness (h_2) have been designed, as listed in Table 4.1, with increasing of Ge concentration and decreasing of bilayer thickness. Both the theoretically calculation and the experimental results indicate that the higher Ge concentration as well as the thinner film will lead to a smaller diameter of the tube. Most of the experimental diameters are in good agreement with those predicted by calculations except for sample (a). It is also noticed that the calculation of Eq. (2.20) based on model II gives more accurate results than that of Eq. 2.6 based on model I, indicating that model II fits better to the real situation of the self-scrolling of SiGe/Si bilayers. Contrary to model I, a factor of ($1+\nu_{Si}$) is applied in Eq. 2.6 of model II by taking the condition of cylindrical scrolling into account [61], which leads to a more precisely calculated result. The minor discrepancy between the experimental diameter and the calculated value based on Eq. (2.20) is attributed to the thin native oxide layer which might form in- or outside of the tube. Depending on the thickness and strain state of oxide layer the diameter of tube could be deviated a little from the ideal one. Sample (a) shows the largest diameter in the table 4.1 and also gives largest relative error to the calculation. The measured diameter of this tube (12.25 μm) is obviously smaller than the calculation (14.71 μm) from Eq. (2.20). This is probably due to the extremely long etching time (ca. 7 hours) for the formation of this "big" tube in aqueous NH_4OH solution to complete a whole turn [3], then the top p-type Si layer is undesirably etched and becomes thinner than the original thickness. All other samples in this series have much shorter wet etching time (< 80 min), thus this effect is negligible. The smallest diameter of SiGe/Si tubes achieved in our experiments without using supercritical drying technique is about 200 nm.

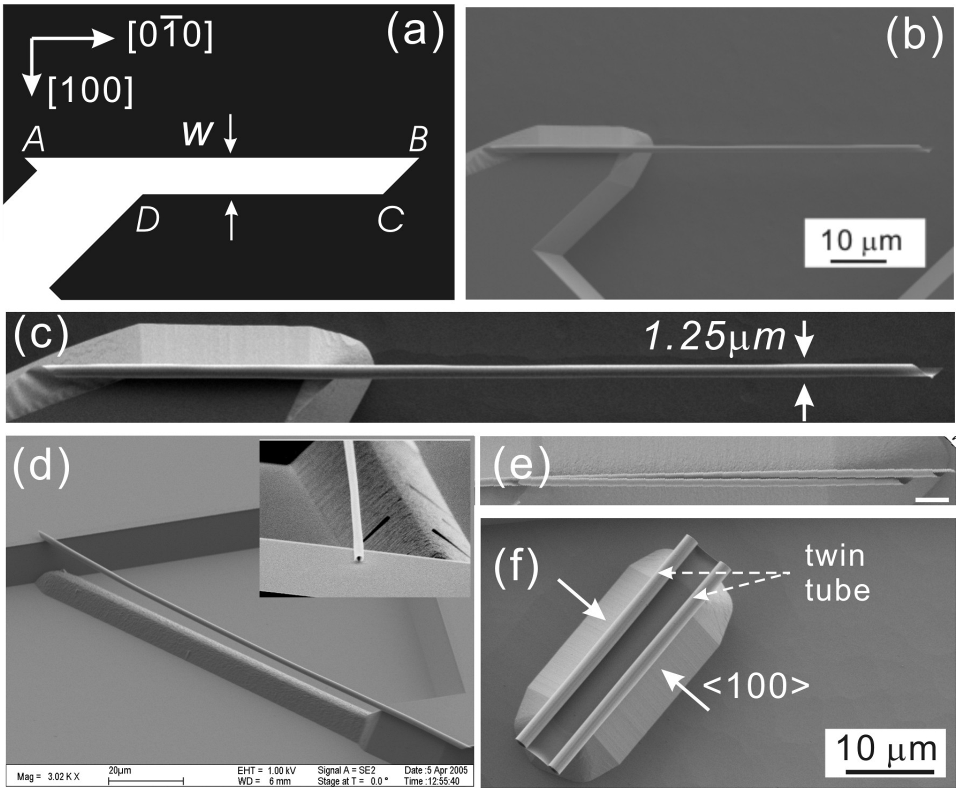

Figure 4.1: (a) The schematic layout of the mesa designing with respect to the crystallographic orientation of the substrate. Here, w is the width of the stripe. (b) FESEM top-view image of a one side fixed freestanding tube. The diameter of the tube is 1.25 μm. (c) Locally magnified SEM image of (b). (d) FESEM side-view images of one side fixed microtubes. (e) FESEM top-view image of a freestanding "twin tube". The scale bar is 5 μm. (f) FESEM top-view image of Si/Cr "twin tube" with bilayer thickness of 10/10 nm. The patterned bilayer is rectangular-shaped and the scrolling direction is <100>.

Table 4.1: Experimental and calculated diameters of the tubes fabricated from $Si_{1-x}Ge_x/Si$ bilayers. h_1 and h_2 are thickness of SiGe and Si layer, respectively. d_{exp} represents the measured experimental diameter, d_I and d_{II} are the diameters from calculation based on Eq. (2.6) and Eq. (2.20) respectively. Model I is based on Tsui and Clyne's equation and model II is based on Grundmann's equation.

sample Nr.	x	h_1 (nm)	h_2 (nm)	d_{exp} (μm)	model I d_I (μm)	model II d_{II} (μm)	relative error to d_I	relative error to d_{II}
(a)	14%	12.1	43.5	12.25	18.68	14.71	34.4%	16.7%
(b)	23%	11.7	7.8	2.10	2.83	2.23	25.8%	5.8%
(c)	40%	11.0	8.0	1.25	1.56	1.22	19.9%	2.5%
(d)	40%	5.5	4.0	0.60	0.78	0.61	23.1%	1.6%
(e)	40%	2.8	4.0	0.50	0.57	0.45	12.3%	11.1%
(f)	40%	2.8	2.0	0.30	0.40	0.31	25%	3.2%

4.1.1.2 Microtubes on Si (110) and (111) surfaces

The methodology to scroll strained hetero-structures to form tubes was also investigated on Si (110) and (111) surfaces which are frequently used for MEMS/NEMS [62, 63]. A pronounced anisotropy of Young's modulus is found in the direction parallel to Si(110) surface [43]. The main advantage of using Si(111) as substrate is that the etching rate in the <111> direction is 7.5 times lower than that in the <110> direction [56], which allows a rapid underetching in the <110> direction of a mesa holding the SiGe/Si bilayers. Thus, the requirement on the etching selectivity between SiGe/Si bilayers and their substrate is less demanding compared with using Si(001) as a substrate [26]. These peculiarities of (110) and (111) substrates make them of particular interest to study the fabrication of micro- and nano-objects by scrolling of hetero-/hybridstructures. Based on the differences of the crystallographic orientation and Young's modulus on (100), (110) and (111) Si wafer surfaces, as shown schematically in figure 4.2, SiGe/Si and SiGe/Si/Cr semiconductor and hybrid thin films are expected to have different scrolling regulations for the formation of 3D structures on Si (110) and (111) substrates. On Si (110) substrate, the two important crystallographic directions, i.e. [001] and [1-10], are perpendicular to each other as shown in figure 4.2b, whereas the two inclined (111) planes intersect the (110) surface with the [1-10] direction (see figure 4.2e). Thus, it is predictable that these two etching-stop (111) planes will retard the lateral underetcing process in [001] direction, hampering the films to scroll along [001], the direction of the smallest young's modulus on the surface. Among different Si substrates, Si (111) is the only one which has an almost isotropic Young's modulus in the plane [43, 64]. Hence, it is expected that on this kind of substrate the effect of anisotropic underetching rate will play an important role in deciding the scrolling direction. The purpose of this section is to discover the scrolling behavior of 3D freestanding structures fabricated on these two important surfaces.

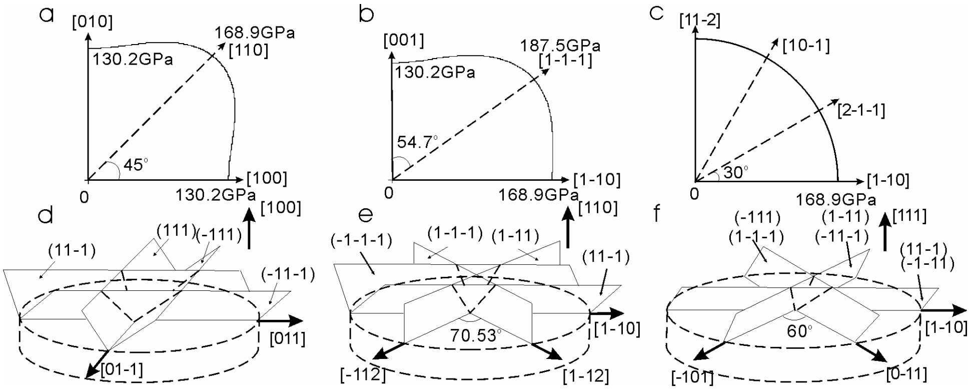

Figure 4.2: (a-c) Schematic drawing showing the values of Young's modulus on Si(100), (110) and (111) surfaces, respectively. (d-f) Geometry of the (111) etching stop planes in Si(100), (110), (111) substrates and the orientation of intersection line on the surface.

Before the fabrication of tubes on Si (110) and (111) substrate, wagon wheel shaped patterns [65] were designed for both types of substrates to investigate the dependence of lateral underetching rate on the crystallographic orientation of mesa lines. As the mask layer of the samples used in this test, a 15 nm thick Cr layer was deposited directly on the substrate. After the lithography process, the samples were etched in 3.7% $NH_4OH{\cdot}H_2O$ at room temperature. To determine the lateral underetching rate of the samples quantitatively, the width of freestanding underetched Cr mesa lines was measured in a FESEM. To get rid of Cr stripes on the surface, the Cr layer was finally etched away by RIE after the lateral underetching rate measurement. The resulted etching profiles (figure 4.3) clearly show the anisotropy of the lateral underetching of the both surfaces. On the

(110) surface, an interesting feature is noticed that the underetching rate in [1-10] direction (the lateral etching direction of the mesa line along [001]) is rather high, whereas the underetching rate in [001] direction (the lateral etching direction of the mesa line along [1-10]) is the lowest. The very low lateral underetching rate in the latter case can be explained due to the (111) etching-stop plane facing to this etching direction (see figure 4.2e). The underetching profile on the (111) surface shows a 6-fold symmetry, and the mesa line direction with [11-2] orientation shows a high lateral underetching rate. In contrast, the mesa line along [1-10] direction has the slowest underetching speed due to the (111) facets (see figure 4.2f) to be formed in that direction. The influence of the anisotropic etching profiles (figure 4.3) together with the Young's modulus (figure 4.2) on the scrolling behavior of the tubes fabricated on Si (110) and (111) substrates will be further discussed in the following parts of this section.

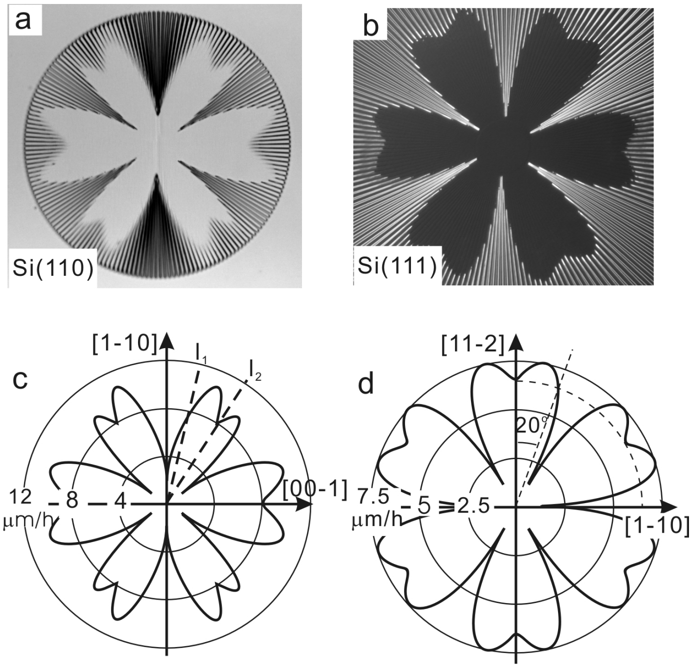

Figure 4.3: (a) SEM image of lateral underetching profile on Si (110). (b) SEM image of lateral underetching profile on Si (111). (c) Lateral underetching rate as a function of orientation. l_1 *is 13° off [1-10] and* l_2 *is 33° off [1-10]. Note that all orientations between these two lines have a higher lateral underetching rate than [00-1]. (d) Lateral underetching rate as a function of orientation.*

The tubes fabricated on Si(110) substrate consist of SiGe/Si/Cr layer stacks with the thickness of 5/4/10 nm, respectively. The SiGe/Si/Cr layer sequence deposited on Si(111) substrate contains the thicknesses of the individual films of 3/4/13 nm, respectively. The Ge concentration of all above SiGe films is about 30%. On the Si(110) oriented substrate, the long sidewalls of mesas were aligned to either [001] or [1-10] directions. On the Si(111) substrates, the tube formation was investigated using triangular shaped mesa patterns with edges aligned in the direction perpendicular to the <112> first, then in directions deviated from the <112> by 10° to 350° in steps of 10°.

SEM images in figure 4.4 show the SiGe/Si/Cr microtubes produced from a "butterfly"-shaped pattern (figure 4.4b inset), in which its edge is aligned in the direction of <001> (figure 4.4 a-d) or <1-10> (figure 4.4a inset) on the Si(110) surface. The diameter of the tubes is about 1.9 μm. The experimental results show that the scrolling direction of the SiGe/Si/Cr film stacks is along <110>, the direction with the highest lateral etching rate, but not along <001>, although the latter is the direction of the smallest Young's modulus on the (110) oriented surface.

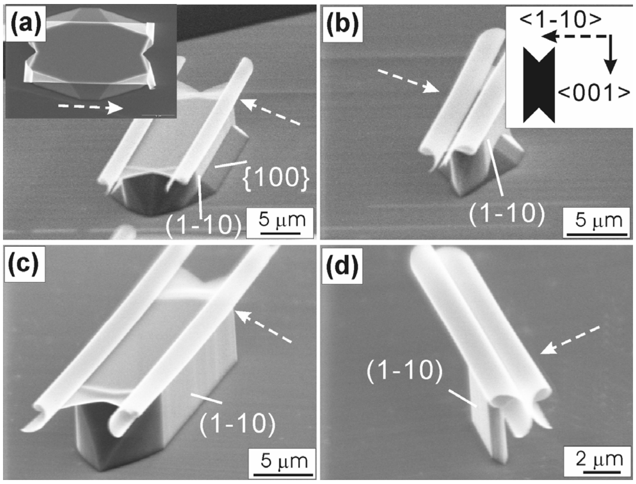

Figure 4.4: SEM images of the SiGe/Si/Cr micro-tubes fabricated on Si(110) surfaces etched at different temperatures. The scrolling direction of the mesa pattern is <110>. (a-b) Two mesas of different sizes etched for 45 minutes at room temperature. (c-d) The samples etched at 75 °C for 12 minutes. Only (1-10) underetching facet was observed along <1-10>. The inset of image (a) indicates the mesa pattern aligned to <110>. The inset of image (b) indicates the designed mesas aligned with <001>. The dash line arrows in all of the images point to <1-10>.

Above results clearly show that the scrolling direction of SiGe/Si bilayers on Si(110) is governed by the fast underetching rate, due to the anisotropic underetching of the substrate. By using this regulation, other preferential scrolling directions, in addition to <110>, are possible to be predicted. According to the underetching profile (figure 4.3c), the maximum etch rate on Si(110) in the direction 22º off <1-10> is noticed; also, the Young's modulus in this direction is smaller than that in the <1-10>. Thus additional scrolling directions can be expected for the mesa lines oriented in an angular range near this direction (between l_1 and l_2, see figure 4.3c). This prediction is confirmed by our experiments. Indeed, tubes containing SiGe/Si/Cr and SiGe/Si layer sequences can be rolled up easily when their sidewalls are oriented in the directions from about 13º to about 33º off <1-10> (between l_1 and l_2, figure 4.3c). Some examples are shown in figure 4.5.

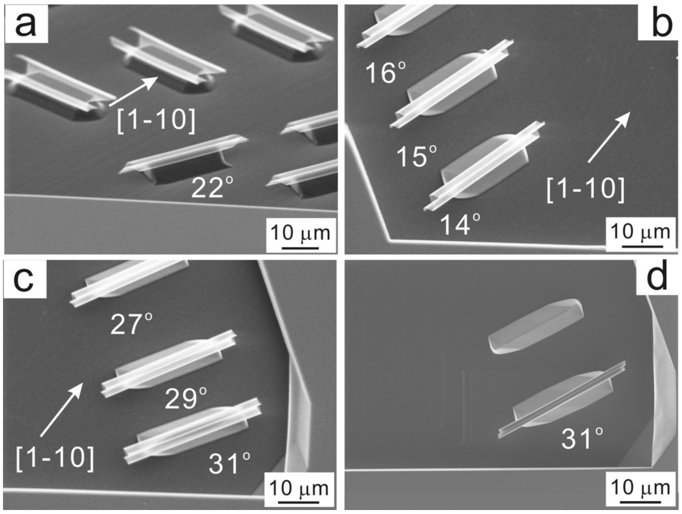

Figure 4.5: SEM images showing the scrolling directions on Si(110) surface of samples etched in 3.7% NH_4OH solution at room temperature. (a)-(c) micro-tubes with Cr coating, (d) without Cr coating. (b-c) SEM images showing top-view of the tubes. The angles indicate the misalignment towards the [1-10] orientation. The white arrows present the [1-10] direction. (d) The patterns are the same as (c), but without a top Cr layer. The SiGe/Si tube has a diameter of about 900 nm. The wet etching process was performed at room temperature by 3.7% $NH_4OH{\cdot}H_2O$ solution.

Since (111) plane would suppress the scrolling of the films as presented for (110) surface, it is expected that the deviation of a few degrees off from <1-10> is necessary for the directional scrolling of SiGe/Si/Cr stacked films in (111) substrate. Figure 4.6 shows the experimental results for fabrication of microtubes with different orientation of the patterns in this substrate. One can find that when the pattern aligned to <110>, it is very difficult to scroll the film to form a tube, whereas the patterns misaligned 10º or more from <110> direction formed tubes with a good reproducibility. This result verifies that to roll up tubes on Si(111) surface, the designed sidewalls of the Si-based strained films should be oriented at least 10° off from the <110> direction.

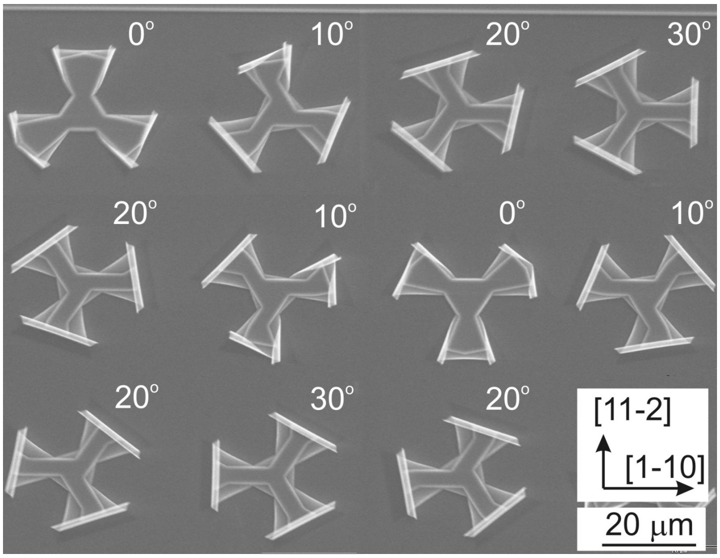

Figure 4.6: SEM top-view image of the 3-fold symmetrical patterns employed to test the preferred scrolling direction on Si(111) substrates. In the top right corner of each pattern, the misaligned angle to <1-10> direction is marked.

4.1.1.3 Conclusion

In conclusion, we have demonstrated a simple and thus reliable technology to fabricate 3D microtubes from the strained SiGe/Si films deposited on different Si substrates by UHV CVD growth. The tube diameter is precisely controlled by the thin film layer thickness and the lattice mismatch between SiGe and Si layers. Also, the preferred scrolling directions of microtubes on Si(110) and Si(111) surfaces were compared to those on Si(001) substrates. It has been found that on Si(110) and Si(111) substrates, the scrolling direction of microtubes is dominated by the anisotropic underetching of mesa structures, whereas anisotropy of Young's modulus is of minor importance.

4.1.2 Helical micro-structures

Si-based microcoils are quite interesting 3D micro-structures having potential applications for sensors as well as for inductors in microelectronics. The structure of microcoils is mechanically elastic and more flexible than tubes. Moreover, the helical structures have an excellent surface to volume ratio and easy accessible surfaces, which is opening new potential applications in particular for biological and chemical sensors [66]. However, it is still in a challenge to fabricate Si-based semiconductive or hybrid microcoils with desired shapes and dimensions for the real applications, and the scrolling behavior behind the fabrication of microcoils needs to be better understood. In this section, we focus on the principle and technology for the controllable fabrication of SiGe/Si and SiGe/Si/Cr microcoils using different design of mesa line patterns with the stripe width equal to or larger than 1μm. Clearly, contrary to fabrication of a tube, a misaligned angle between stripe and scrolling direction is necessary to form a microcoil with a specific helicity angle. The helicity and pitch of a helix are described in figure 4.7. Here we define the pitch p as the rising distance of the coil along the tube axis needed for one turn. The helicity angle θ is equal to the misalignment angle between the preferred scrolling direction [xyz] and the orientation of the stripe [uvw] as defined in figure 4.7. The mesa configuration illustrated schematically in figure 4.7 results in a right-handed helix. The geometrical relation between the pitch p, the diameter d and the helicity angle θ of a helix is described by Eq. (4.1):

$$p = \pi d \cdot \tan \theta \qquad (4.1)$$

The width of the stripe w is given by its initial pattern design. The spacing s between each turn of helix in the axis direction can be calculated by:

$$s = p - w / \cos \theta \qquad (4.2)$$

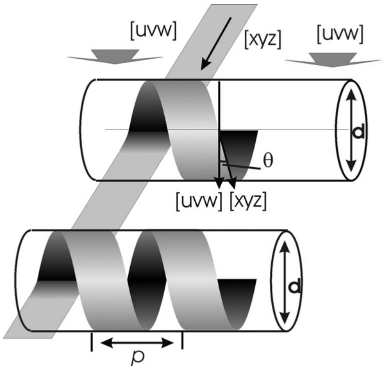

Figure 4.7: Schematic drawing of a helix formed by rolling-up of a stripe. The definitions of diameter d, pitch p, and helicity angle θ *are presented in the figure, where* $p = \pi d \tan\theta$ *. The crystal orientation of the stripe is represented by [xyz], and [uvw] is defined as the scrolling direction. This helix shows a right-handed chirality.*

4.1.2.1 One end fixed microcoils

Narrow stripes with different misaligned angles to the <100> direction were designed (see figure 4.8) for microcoil fabrication on Si (001) surface. Details of the SiGe/Si/Cr mesa line patterning and wet etching to fabricate SiGe/Si/Cr helical coils have been described in chapter 3.

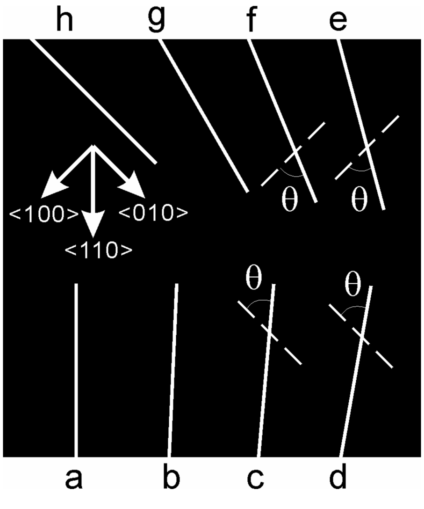

Figure 4.8: The image gives the mesa pattern used to fabricate microcoil. The white region indicates the 8 stripes to form helices, the stripes a, b, c, d, e, f, g, h, have $\theta = 45°, 47.5°, 50°, 55°, 60°, 67.5°, 75°$ *and* $90°$ *respectively,* θ *is the angle between one <100> direction and the orientation of stripe; the crystallographic directions are marked in the image.*

Figure 4.9 shows SEM images of typical microcoils made by the mesa lines depicted in figure 4.8. Here the initial planar films consisted of a three-layer SiGe/Si/Cr stack having a thickness of 3.5 nm, 4.5 nm, 15nm, respectively, and a Ge concentration of about 50% in the SiGe film. The width of mesa stripes is 1 μm. Measured from the SEM images, the diameter of these helices is about 1.7 μm. Table 4.2 summarizes the different etching temperatures and times of the four samples depicted in the SEM micrographs in figure 4.9. Table 4.3 shows a good agreement of the experimentally determined parameters of these helical coils with the values calculated by Eq. (4.1).

The pitch of a helix measured from SEM image is sometimes slightly smaller than the calculated one because: (i) The observation angle of the SEM images may not be exactly perpendicular to the axis of the helix, and (ii) During the drying process, the coil might be deformed by surface tension: the liquid in the helical belt tries to contract the coil during its drying. One way to avoid the effect of surface tension is to use supercritical drying, then surface tension will be eliminated at the interface [60]. (iii) Stress relaxation at the edge of the stripe may occur, which leads to the scrolling direction slightly deviating from the preferred <100>. This effect will be discussed in section 4.2 for the fabrication of nanostructures, which becomes more significant if the width of the mesa line is scaled down to less than 1 μm.

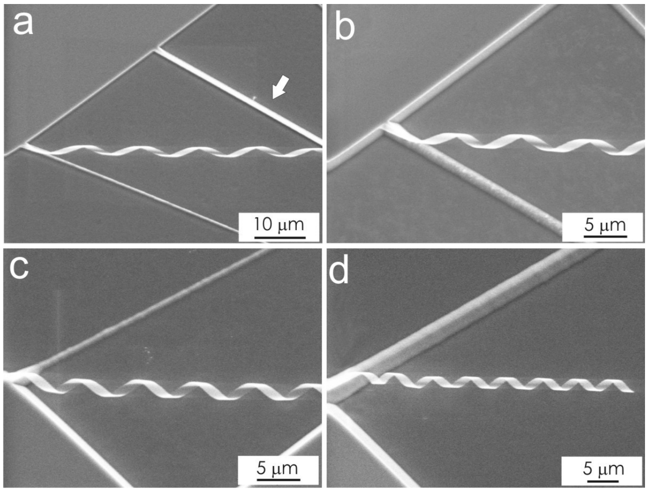

Figure 4.9: SEM images of $Si_{0.5}Ge_{0.5}$/Si/Cr (3.5/4.5/15 nm) helices with different misalignment angle (θ) and pitch (p_{exp}) values. (a) θ=67.5° (b) θ=60° (c) θ=55° (d) θ=50°. The pitch data are presented in table 4.3.

Table 4.2: Etching conditions and diameters of helices shown in Figure 4.9.

Helices	Etching Time (min)	Etching Temperature (K)	Etchant (NH_4OH)	Diameter d (μm)
Fig. 4.9a	5.25	300	3.7%	1.7
Fig. 4.9b	1.75	370	3.7%	1.7
Fig. 4.9c	15	300	3.7%	1.7
Fig. 4.9d	25	300	3.7%	1.7

Table 4.3: Comparison of the pitch obtained experimentally (p_{exp}) and theoretically ($p=\pi d \cdot \tan\theta$) for various misalignment angle θ, i.e. the mesa orientation.

misaligned angle θ	theoretical value p (μm)	experimental value p_{exp} (μm)
67.5°	12.89	12.29 ± 0.16
60°	9.25	8.58 ± 0.10
55°	7.62	7.05 ± 0.10
50°	6.36	6.00 ± 0.12
47.5°	5.83	5.40 ± 0.10

An interesting phenomenon revealed by SEM observations is the difference of the scrolling speed of the stripes with different misalignment angles. Figure 4.9a shows an example, in which a stripe with $\theta = 67.5°$ has already scrolled completely into a helix, whereas the adjacent one with $\theta = 60°$, looked as a straight stripe indicated with an arrow in figure 4.9a, even has not yet started to roll up. The different etching time needed for releasing the SiGe/Si/Cr films with the same length but different orientation from the substrate is mainly caused by the anisotropic underetching rate of the substrate. On Si (001) substrate, the smaller the angle between the narrow stripe and the <110>, the slower the etching speed. For stripes aligned closer to the <110> direction, (111) facets rapidly form at the sidewalls along the mesa stripe, hampering the underetching in the sidewalls. In this case, the etching process predominately started from the tip of the mesa, thus it will take a much longer time to free the structure from the substrate. This effect is illustrated in figure 4.10, representing SEM images of the $Si_{0.6}Ge_{0.4}$/Si/Cr microcoils prepared from the same pattern as previously discussed ones, thus they were fabricated together having the same etching time in the NH_4OH solution. The stripes shown in figure 4.10a-f have misalignment angles of $\theta = 45°$ (see figure 4.10a-c), 47.5° (see figure

4.10d-e) and 50° (see figure 4.10f), respectively. Figures 4.10a-c show images of the same stripe observed from different viewing angles, clearly demonstrated that the stripe with $\theta = 45°$ has the lowest rate of underetching from the sides. Here the sidewalls are rather smooth and actually formed by (111) facets, which are the planes with the lowest etching rate. An increase of the deviation of the mesa line orientation from the <110> direction leads to an increase of the underetching rate on the sidewalls. At small deviations, the dense etching steps already can be observed on the (111) facets (see figure 4.10d-e), which allow the attack of the anisotropic etch actively at the kink-like steps on the sidewalls. The more kinks form with the increasing deviation from <110>, the faster the lateral underetching of the mesa stripe. From the thermodynamic point of view, etch pits can nucleate at kink positions much easier [67, 68]. Thus, lateral underetching is faster when the sidewalls have more steps. Here we might note that the change of lateral etching rate in the vicinity of (111) planes is very sensitive even to a small angular misalignment. It has been reported by H. Seidel et al [65], that for EDP (a water solution of ethylenediamine and pyrocatechol) and KOH, the etching rate increases by about a factor of two for a misalignment angle of 1° on a <100> wafer. Finally, for a larger deviation (figure 4.10f) the sidewalls become rough, no obvious (111) planes form and the underetching occurs rapidly. Thus, the microcoil has scrolled out of the viewing field of the image in figure 4.10f, and formation of the helix is completed as shown by a lower magnification image in the inset of figure 4.10f.

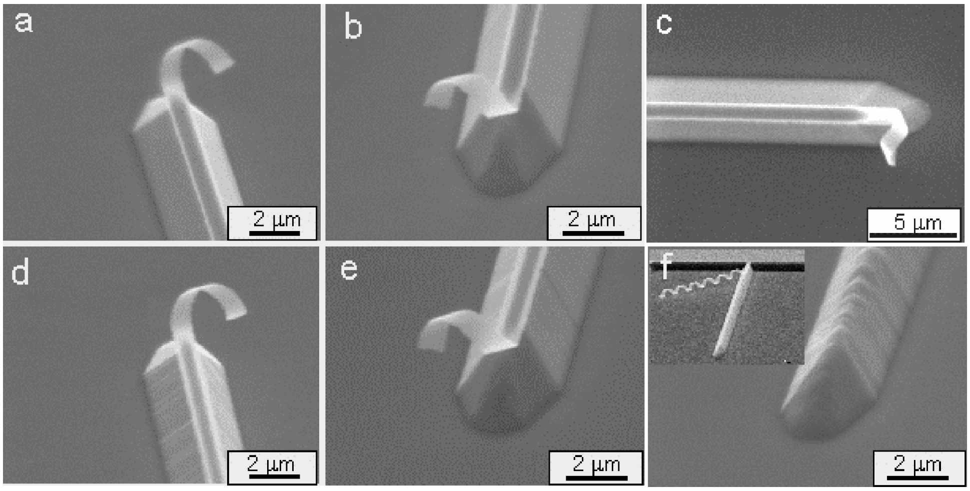

Figure 4.10: SEM images of $Si_{0.6}Ge_{0.4}$/Si/Cr (8/10/15 nm) helices on the Si(001) substrate, showing the different underetching speed with the different misaligned angles. (a-c) $\theta = 45°$, (d-e) $\theta = 47.5°$, (f) $\theta = 50°$. All samples are investigated in SEM with the sample holder 60° tilted except image c which is a top-view.

The chirality of the helical structures has also been investigated. It can be expected that the orientation of the mesa stripe is critical to control the chirality. This is illustrated in figure 4.11, showing three mesa lines with three different crystal orientations on the surface, where the center one is oriented along the <110> direction and the left and right ones with a deviation of minus and plus ϕ degree $\left(0 < \phi < 45^\circ\right)$, labeled "a" and "b" respectively. The two preferred <100> etching directions are indicated by the arrows in the figure. Due to the misalignment, these preferred etching directions form different angles to the left and right sides of the two mesa stripes ("a" and "b"), as indicated by θ_1 and θ_2 in figure 4.11. The larger angle θ_2, which is always larger than 45° here, determines the helicity angle, i.e. $\theta=\theta_2=45^\circ+\phi$ (see figure 4.11). Consequently, it is expected that the mesa "a" will lead to a left handed helix and the mesa "b" to a right handed one.

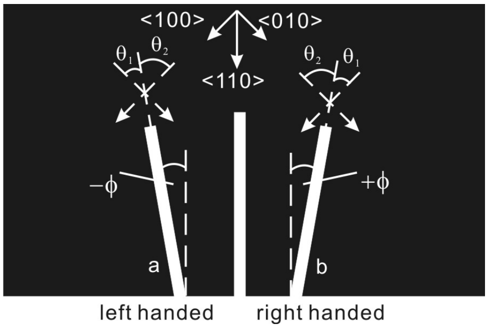

Figure 4.11: Illustration of stripes pattern design with different misaligned angles. There are two possible preferential etching directions of <100>, which are shown in the figure. One of the angles between etching direction and stripe is larger than 45°, and the other is smaller than 45°. The stripe scrolls along the direction with θ > 45°. This rule will lead stripe "a" to form a left handed helix and stripe "b" a right handed one. When θ = 45°, i.e. stripe oriented to <110>, both left and right handed chiralities are possible.

To estimate the driving force for rolling-up of a stripe with a specific chirality, an important fact must be noticed: the detaching and the spontaneous releasing of the local stress of the SiGe/Si bilayers (or SiGe/Si/Cr film stacks) from the Si substrate is a gradual and continuous process with the etching time. Since this is a dynamical process, it is necessary to localize the momentary contribution to the bending moment in a narrow area near the "etching front", other than the whole freestanding triangular-shaped piece.

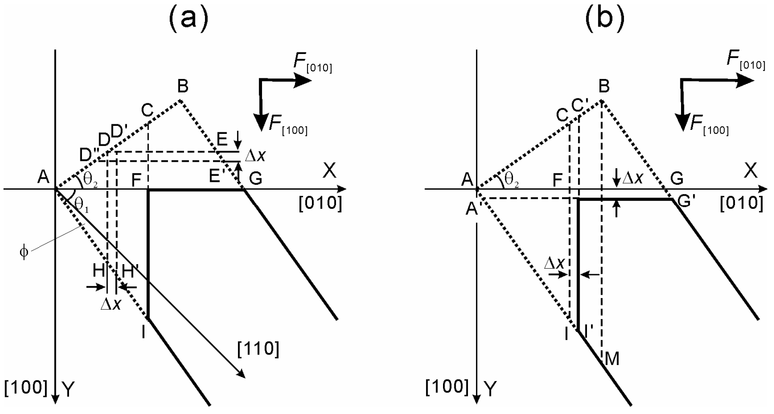

Figure 4.12: The rectangular-shape stripe has ϕ degree off <110>, $0^\circ < \phi < 45^\circ$. *In the image,* $\theta_1 = 45^\circ + \phi$; $\theta_2 = 45^\circ - \phi$.

To make the discussion easier, a simple drawing is given to illustrate the etching process (see figure 4.12) for a rectangular-shaped SiGe/Si bilayer stripe oriented ϕ degree off [110], assuming that <100> is the maximum etching rate direction on the stripe. The general principle of this assumption will be still held for the real situation where the maximum etching rate direction is about several degrees off from <100>. So, two etching fronts along <100> would be developed from the corners (*A* and *B*) of the stripe when the etching process starts. Apparently, the distance from the two corners to the respective etching fronts is equal since the etching rate along [010] and [100] is the same owing to the same crystallographic nature.

The successive etching process developed from the corners of a rectangular-shaped stripe can be divided into the following steps though it may happen rather quickly in practice. Firstly, in a very beginning stage, both the corners of *A* and *B* started to be underetched, then the two etching fronts ($\overline{DH}$ and $\overline{DE}$) gradually developed from corners *A* and *B* and met each other at point *D* as illuminated in figure 4.12a. The local stress of the freestanding parts in the triangular-shaped region of the corners tended to be released along the preferential rolling-up direction one step by another after they successively detached from the substrate, and both the small freestanding parts at the corner *A* and *B* would be bent up slightly along their most compliant directions of [010] and [100] respectively. To calculate the momentary stress for the bending, the successive new freestanding part nearby the etching front can be considered approximately as a narrow rectangular strip with a length of Δx, as shown with the parallel dashed lines in figure 4.12a. In this case, the force (per unit length) *F* along the edges of a rectangular-shaped film (here it is along the two <100> to bend) can be estimated, according to Tsui and Clyne [41], as follows:

$$F_{[100]} = \delta_{[100]}\overline{DE}\left(\frac{h_1 h_2 E_{Si}}{h_2 E_{Si} + h_1 E_{SiGe}}\right) \tag{4.3}$$

and

$$F_{[010]} = \delta_{[010]}\overline{DH}\left(\frac{h_1 h_2 E_{Si}}{h_2 E_{Si} + h_1 E_{SiGe}}\right), \tag{4.4}$$

where δ is the stress in SiGe layer due to the lattice mismatch of the SiGe layer to the Si layer, E is the Young's modulus, h_1 and h_2 are the thicknesses of the SiGe and Si layer, respectively. Obviously, in this stage, $F_{[010]} = F_{[100]}$, which implies that the scrolling direction or the chirality of the stripe is not decided yet at this moment.

However, the magnitude of $F_{[100]}$ and $F_{[010]}$ along the two possible preferred scrolling orientations [100] and [010] is going to change soon after the further underetching as the [010] line developed from corner *A* intersects the stripe reaching its maximum value, i.e. $\overline{AG}$ (see figure 4.12a). In this stage, the etching fronts move from *HDE* to *IFG*. Furthermore, the [100] line will intersect the stripe with an increasing value until it reaches $\overline{BM}$ as shown in figure 4.12b. By applying the same method to estimate the force as demonstrated above, $F_{[010]}$ will finally becomes larger than $F_{[100]}$ in each etching step in this stage since $F_{[010]}$ is increasing while $F_{[100]}$ kept constant, as we can see *C'I'>CI* while *A'G'=AG* in figure 4.12b. Because the bending moment is proportional to the force [41]:

$$M = F\left(\frac{h_1 + h_2}{2}\right) \qquad (4.5)$$

The larger force generated the larger bending moment in the corresponding bending direction, thus finally determines the scrolling direction of the stripe. Once the scrolling towards a certain direction started, it would be continued to the end of the stripe because the difference between two forces keeps constant. Therefore, the freestanding part of the stripe will be coiled along [010] in this case and a right-handed microcoil formed eventually.

Furthermore, the chirality of the helices is affected not only by the orientation of mesa stripes but also by the shape of mesa's tip at the end of mesa stripe, which is illustrated in figure 4.13. Figure 4.13a-c show the mesa designs in black and white schematics and the corresponding SEM images for mesa stripes oriented along θ = 45°, 50°, and 55°, respectively. For each orientation different shapes of the end tip of mesa stripes have been chosen. These different pattern designs permit the control of the chirality of the helix, which is clearly visible in the SEM images presented in figure 4.13a-c. For instance, the symmetric, rectangular shape of the tip of the stripe with $\theta = 45°$ leads to a random chirality (see figure 4.13a, stripes of the top row). However, if the end has a triangular shape with a cutting direction of the tip along <100>, the initial rolling direction on the tip is pre-determined and the chirality of the helix is given.

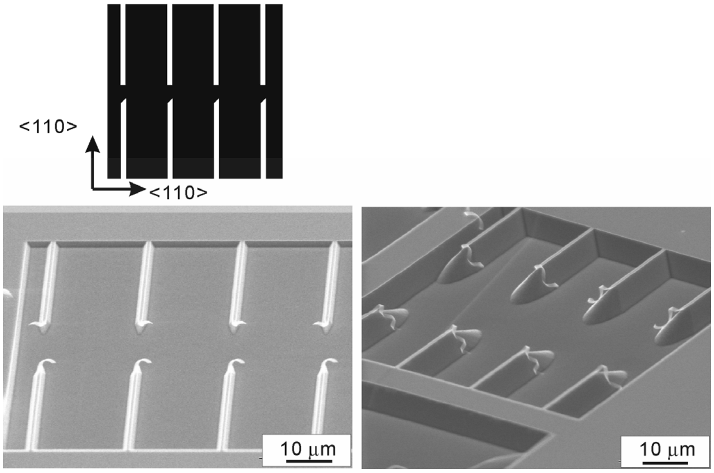

Figure 4.13a: All of the stripes have $\theta = 45°$ those of the top row have rectangular tip and formed random chirality; whereas the stripes of the bottom row were cut on the tip along <100> direction instead of <110>, and all formed the right handed chirality exclusively. The width of stripe is 1 µm.

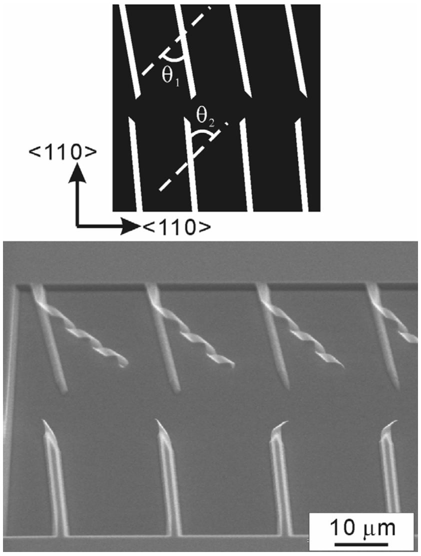

Figure 4.13b: All tips of the stripes were cut along <100>. The stripes of the top row have $\theta = 55°$. The stripes of the bottom row have $\theta = 50°$ all of them with a width of 2 µm. The chiralities formed from the stripes with $\theta = 50°$ are modified by the shape of the tips, but stripes with $\theta = 55°$ are not modified.

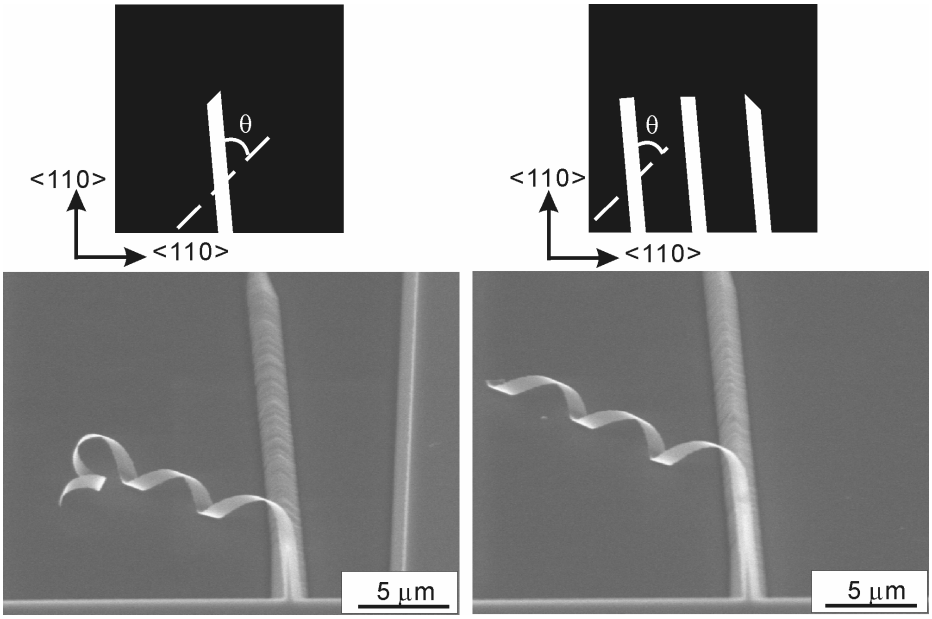

Figure 4.13c: SEM images of stripes with different types of tips, showing that even though the chralities of the stripes are modified, the influence of this modification is limited. θ = 50°. The width of the stripes is 1 µm.

However, the shape of the tip has less impact on the chirality if the stripes are misaligned with respect to the <110> direction. For θ = 55°, i.e. a misalignment of 10°, the chirality is independent of the shape of the tip and completely determined by the direction of the mesa stripe (see figure 4.13b, top row). Here the asymmetric underetching on the side of the mesa lines is fast, eliminating the effect of the shape of the mesa tip. For θ=50° (see figure 4.13b, bottom row) the underetching on the sides becomes much slower. Thus even though the bottom and top lines were processed together, the top ones are completely freed from the substrate whereas for the bottom ones the etching has barely started. Here, at least the starting of the scrolling process depends on the orientation of facets developing at the tip, thus the shape of the tip determines the chirality at the beginning of the etching. However, in the process of etching again the asymmetry of the sidewall underetching of the mesa line becomes the dominant process, which might change the initial chirality as it is shown in figure 4.13c.

4.1.2.2 Both ends fixed microcoils

To produce freestanding SiGe/Si helices with their two ends fixed on substrate, V-shaped mesas were scrolled. This design leads to helices with two arms of opposite chirality [69], and also makes this type of helix mechanically stronger than the helix with only one end fixed, allowing us to synthesize longer helices. This design also allows us to fabricate source and drain contacts to such a structure to produce bio-chemical sensors similar to those using Si nanowires [66]. In contrast to the helix with one end fixed, whose helical angle is always larger than 45° as mentioned in the previous section, a helix with both ends fixed does not have such a limitation. Because the rolling direction of the two stripe parts is fixed to only one <100> direction as indicated by an arrow in the inset of figure 4.14a. It means that the two helical parts with opposite chiralities in the helix can have helical angles even smaller than 45°, which increases the freedom of design.

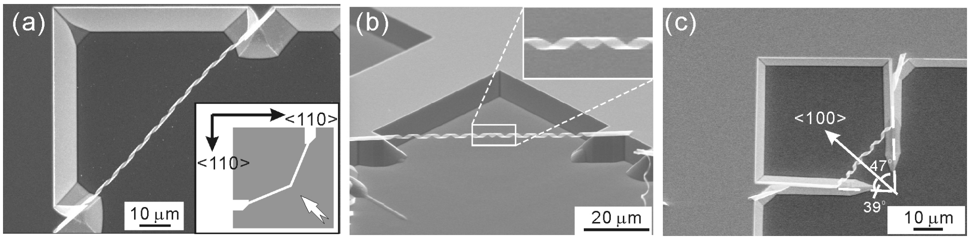

Figure 4.14: (a) SEM image of a typical helical structure (diameter of 1.4 μm) with the both ends fixed on the substrate, showing that the upper and below parts of the helix have opposite chiraities. The inset shows the mesa design and the rolling direction of the helix as indicated with a white arrow. (b) A helix with diameter of 1.7 μm and structured of $Si_{0.5}Ge_{0.5}$/Si/Cr (3.5/4.5/15 nm). The width of the stripe is 2 μm. (c) An unsymmetrical helical structure showing different pitches in the two parts of the helix, resulted from the different misalignment angles (47° and 39°) between the two parts as indicated.

The Cr layer was etched away in a mixture of ceric ammonia nitride (CAN) and acetic acid after the SiGe/Si/Cr microcoil was formed. To prove that the Cr layer has been removed by the Cr-etchant, both planar and 3D samples have been investigated by EDX (Energy Dispersive X-ray). To increase the sensitivity detecting the residual Cr on the surface, all the samples were tilted at a large angle (close to the grazing angle) giving the incident beam a longer path near the surface. No Cr and predominantly Si, Ge, and some oxygen have been detected by EDX.

Figure 4.14a shows a typical SiGe/Si helix with a diameter of about 1.4 μm fabricated in this way, which has an 8 nm thick $Si_{0.6}Ge_{0.4}$ and a 10 nm thick Si layer. The structural parameters of the fabricated helices, which are fixed on both sides, match well to the theoretical predictions (Eq. 4.1 and 4.2). An additional example of a helix fixed on both sides with the Cr still on the top is shown in the SEM image in figure 4.14b. Note that no supercritical point drying was applied and the as-fabricated helix is very straight with uniform pitches and helictiy angles. The helices shown in figure 4.14 a-b are fabricated from V-shaped mesa structures, whose two arms are symmetric to the <100> direction of the substrate. This design leads to helices with a left- and a right-handed arms having the same pitch and helicity angle. This structure makes them applicable as micro- or nano-capacitors in modern micro-electronic systems, because the net inductance is neutralized by the opposite chiralities of the two parts of the helix. Based on this structure, an asymmetrical structure can also be formed, if the misalignment angles of the two parts of the stripe are different in the design pattern. This design leads to a helix with arms of opposite chirality and a pronounced difference in the pitch, easily visible in figure 4.14c. The diameter of the helix is about 1.8 μm, which consists of two parts with different pitches of about 4.1 μm and 5.4 μm approximately. To obtain this unsymmetrical helix, the two arms of the V shaped mesa stripes were designed having a same width (1.5 μm), but different misaligned angles of 39° and 47° to the <100> etching direction, as indicated in figure 4.14c. By using this technique a helix with defined inductance can be produced, if one part of the structure is a helix whereas the other part is designed to form a tube-like structure, due to a misalignment angle θ close to 0°. Therefore, both micro-capacitors and inductors can be obtained using the helices fabricated by this controllable method.

4.1.2.3 Conclusions

We have developed the technology for fabrication of helical micro-structures with the stripe width not smaller than 1 μm. Reproducible fabrication allowed us to study in detail the design parameters which determine the shape and chirality of the structures. The results unambiguously show that the preferred rolling direction for strained SiGe/Si and SiGe/Si/Cr strained films is determined by the Young's modulus to be the (100) direction on a (001) oriented substrate. Comparison with simple models reveals that the pitch and the helicity angle of one end fixed helix can be quantitatively controlled by the starting 2D mesa design. The chirality of the helix can be locally modified by tailoring its tip. Freestanding helices with both ends fixed to the substrate were also successfully fabricated, which can have either symmetric or asymmetric helicity angles. The method was used to produce semiconductor SiGe/Si as well as hybrid semiconductor-metal SiGe/Si/Cr helical structures.

4.2 Scrolling behaviors of nanostructures

In order to fabricate delicate nanodevices for NEMS, the dimensions of the designed mesa structures for the formation of 3D shells have to be reduced from the micrometer to nanometer scale. In this part, a variety of novel 3D nanostructures such as vertical rings, freestanding nanohelices, multiwall nanorings and nanospirals have been successfully fabricated from the strained SiGe/Si, SiGe/Si/Cr and Si/Cr films with a width of the mesa lines in nanometer scale. The mechanism behind the formation of these nanostructures has been shown to be intriguing due to the great increase of edges with narrowing of the stripe width. A new fundamental phenomenon, referred as “anomalous coiling” of the strained films arising from the stress relaxation at edges, is particularly noticed and exclusively investigated as the films stripe width becomes below 1 μm.

4.2.1 Fabrication of vertical rings

The rings lying on a substrate surface, i.e. with their rotational axis vertical to the substrate surface, are called here as “vertical rings” [25, 26]. The vertical rings with their belt width of 300 nm were fabricated from SiGe/Si bilayers and SiGe/Si/Cr stacked films, by forcing the rings to tip over using ‘‘T’’-shaped mesa structures on a Si (100) surface as illustrated in figure 4.15a. The asymmetry of the mesa leads to a two-step scrolling process during the etching: firstly, the narrow stripes are scrolled along [001] or [00-1] direction and form upright standing rings; in the second step these rings are underetched from one side, i.e. along [010] in figure 4.15, causing the rings to tip over and forming the vertical rings. The vertical rings in our experiment have a diameter of about 2.5 μm and 1.5 μm for SiGe/Si/Cr and SiGe/Si respectively as shown in figure 4.15b-e. The width of the rings, i.e. the height of the vertical rings, is lithographically defined by the design of the mesa to a width of 300 nm. The SiGe/Si/Cr vertical rings depicted in figure 4.15b and figure 4.15d have a wall thickness of the 23 nm, (SiGe/Si/Cr=3.5/4.5/15 nm), thus the vertical walls have an aspect ratio of 13. The Cr top layer can be removed easily by RIE. In this case, the aspect ratio increases to 37.5 and the radius of the rings decreases to 1.5 μm. In contrast to (100) substrates, Si (111) substrates have almost isotropic Young's modulus [64] and high symmetry of the crystal orientation in the surface plane. This feature allows forming vertical rings from narrow mesa lines oriented in various directions on the surface (see figure 4.16). The vertical rings, depicted in figure 4.16, are fabricated from SiGe/Si/Cr (3/4/13 nm) layer stacks resulting in an aspect ratio of 15.

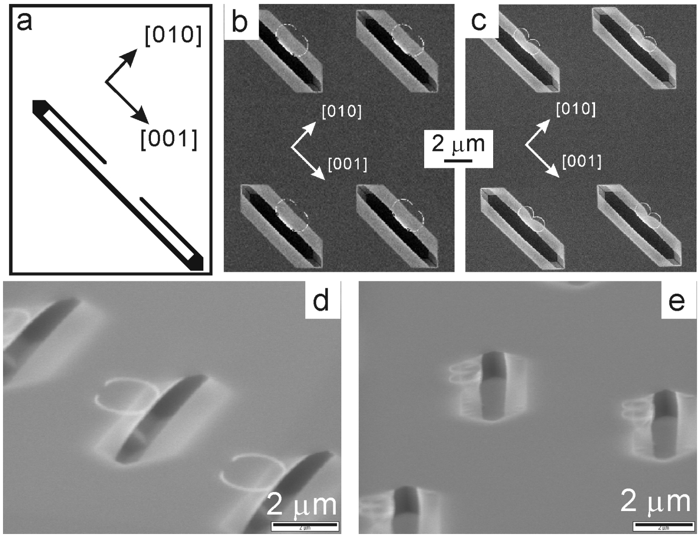

Figure 4.15: (a) Illustration of the "T"-shape mesa design which was used to obtain vertical rings on a S(100) surface. The black part shows the area in which the SiGe/Si bilayer is removed by RIE. (b) SEM top-view image of the SiGe/Si/Cr vertical ring with about half turn. (c) SEM top-view image of the SiGe/Si vertical ring with about one turn. (d) Side-view image of the same sample as shown in (b). (e) Side-view image of the same sample as shown in (c). The sample holder was tilted 70° to horizontal position to take the side-view images.

This technology is an elegant way to produce nanostructures with a high aspect ratio. The metal-coated vertical walls are of large mechanical strength and have smooth sidewalls, which makes them suitable to be used as masters containing nano-structures for nano-imprinting technology.

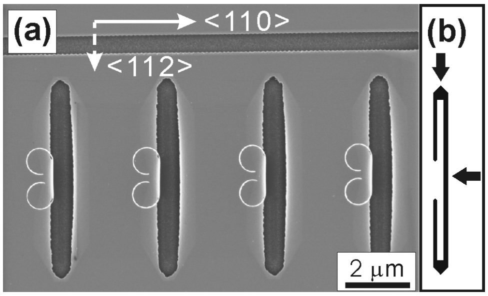

Figure 4.16: SEM top-view image showing an array of vertical ring structures on a Si(111) surface. (b) The initial ''T'' shape mesa pattern used to fabricate the vertical structure. The black arrows indicate the scrolling directions of the hetero-films.

4.2.2 Compact nanohelices

In the previous section (4.1.2), we showed that for mesa lines oriented away from the <100> direction, the helicity angle of these microcoils cannot be smaller than 45°. For applications of the helices in nanoelectromagnets, nanoinductors or nanosprings, it would be desirable if the helicity angle could be reduced sufficiently to allow for a significant increase of the magnetic flux density [70] or the flexibility. In this section, the formation of helical nano-structures from mesa lines of the width less than 1 μm is investigated. Reducing the width of the mesa lines increases the impact of edge effects on the scrolling process, which may offer a new path to overcome the restrictions on the geometry of the as-fabricated structure for bulk mesa stripes. Therefore, it is necessary to study in detail the impact of edge effects on chirality, scrolling direction, and diameter of SiGe/Si and SiGe/Si/Cr helical nanobelts. In the fabrication of SiGe/Si/Cr and SiGe/Si helices, the initial planar SiGe/Si/Cr tri-layer structure contains an 11 nm thick SiGe layer with approximately 40% Ge, an 8 nm thick Si layer and a 10 or 21 nm thick Cr layer. All stripes deviated by 5° or 10° from the <110> direction. The widths of the stripes were varied from 1.30 μm to 0.30 μm in steps of 100 nm. To fabricate the SiGe/Si stripe pattern, the Cr layer on SiGe/Si/Cr stripe was removed by RIE etching process prior to wet etching.

In addition, the dependence of the curvature radius on the stripe width of Si/Cr bilayers is also investigated symmetrically. In the experiment, a 10 or 35 nm thick Si layer with a 10 nm thick Cr on the top is used. The width of Si/Cr stripes is decreased from 3.0 μm to 100 nm, and the stripes are patterned with 3° or 5° off from <110>. All of the samples discussed in section 4.2.2 were dried in a supercritical point dryer to get rid of the impact of the surface tension on the as-fabricated structures during the drying process.

4.2.2.1 SiGe/Si/Cr, SiGe/Si and Si/Cr nanohelices: anomalous coiling

Figure 4.17a-g show SEM images of SiGe/Si/Cr helical nanobelts fabricated from mesa lines with the stripe width ranging from 1.3 μm (see figure 4.17a) to 0.7 μm (see figure 4.17g). All mesa lines are oriented +10° from the [110] direction as indicated in figure 4.17a. The helical coils produced from relatively wide stripes (1.30 μm and 1.20 μm), show a right-handed chirality (figure 4.17a-b), which is consistent with the results of the previously reported microcoils (see section 4.1.2). Here, this type of helical coil is named as "α-helix". Reducing the stripe width to 1.1 and 1.0 μm, both left- and right-handed chiralities occur in a single helix as depicted in figure 4.17c and 4.17d, respectively. This type of slightly disordered helical coil is named as "β-helix" in this thesis. The position on the coil where the chirality of the helix changes is near the free end of the coil in figure 4.17c, whereas the chirality changes close to the fixed end of the stripe for the helix with a smaller width (see figure 4.17d). Also, the shape of the β-helix is often irregular, sometimes appearing disordered due to the competition of two chiralities. The width of the mesa lines is further reduced to 0.9, 0.8 and 0.7 μm in figure 4.17e, f and g, respectively. The helices formed from 0.9 and 0.8 μm wide mesa lines possess a left-handed chirality, which is the opposite chirality of those formed from wider mesa lines of the same orientation. This kind of helix is defined as a "γ-helix". Thus, three different regimes can be defined, broad mesa lines leading to right-handed helices, narrow lines resulting in left-handed helices and a transition regime with disordered helices exhibiting both chiralities. A reverse orientation of mesa lines of -10° leads to opposite chiralities.

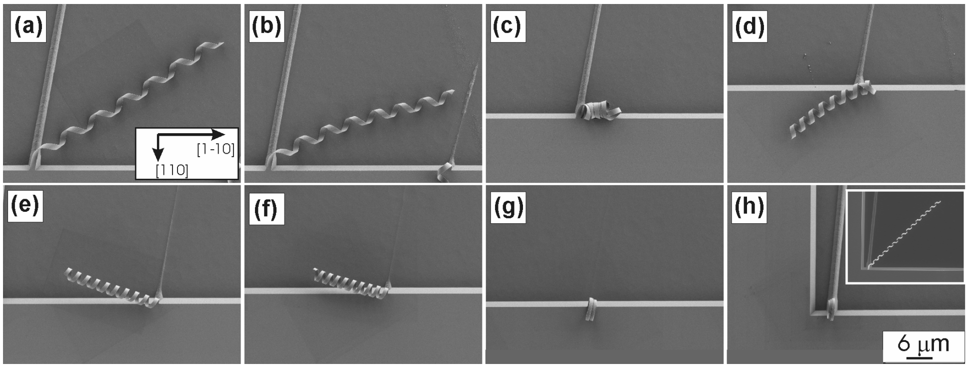

Figure 4.17: SEM top view images of $Si_{0.6}Ge_{0.4}$/Si/Cr helical coils with layer thickness of 11/8/21 nm, except for the one in the inset of (h) which is without a Cr layer. The <110> orientation on the substrate is shown in (a) by black arrows. In (a)-(g) all stripes deviate 10° from the <110> direction, and the width of the stripes decreases stepwise from 1.30 μm to 0.70 μm with steps of 100 nm. Both nanobelts in (h) deviate 5° from <110>. All images have the same scale bar.

Moreover, not only the chirality, but also the pitch and helicity angle change when the stripe width becomes smaller. Comparing the two "γ-helices" shown in figure 4.17e and 4.17f, one can clearly observe in figure 4.17f that the pitch and helical angle is smaller for the helix fabricated from the narrow mesa line (0.9 μm). Moreover when the mesa line is reduced to 0.7 μm, the helical structure collapses into a multi-turned ring structure, as depicted in figure 4.17g. Here, both the helicity angle and the pitch go to zero. Consequently, by adjusting the stripe width for a given strained SiGe/Si/Cr layer stack it is possible to control the pitch of the helical nanobelts. In particular, more tightly wound nano-coils can be designed and fabricated.

To study the impact of the Cr layer, SiGe/Si helices were fabricated from the same sample (SiGe/Si/Cr) using the same mask layout. After the mesa structures were fabricated, the Cr layer was removed by an RIE step, and subsequently, scrolling was initiated by wet chemical etching of the substrate. Interestingly, all of these stripes with a width in the range of 0.7 to 1.3 μm transformed into α-helices. Figure 4.17h compares the result of a scrolling experiment using 0.7 μm wide mesa lines for a SiGe/Si/Cr layer stack and a SiGe/Si bilayer (inset of figure 4.17h). Here the misalignment angle was +5°. Strikingly, the SiGe/Si/Cr layers scroll into a multi-walled ring, whereas the SiGe/Si bilayer forms a right-handed helix. Therefore, to further reveal the effect of stripe width on the formation of SiGe/Si/Cr helical nanobelts, it is necessary to investigate the influence of the Cr layer on the scrolling behavior.

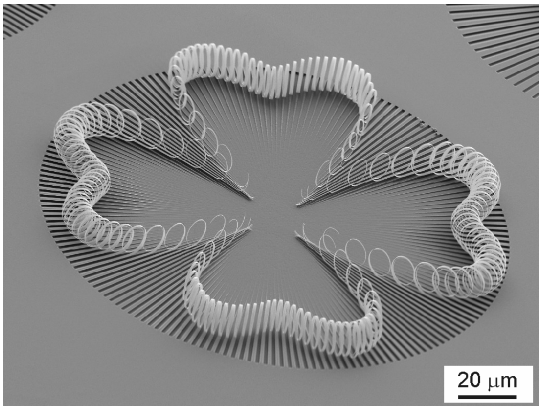

Figure 4.18: SEM image of 3-D structures formed from a bilayer of p-type mono-crystalline Si coated by amorphous Cr, which was applied to investigate the influence of the Cr layer on scrolling behavior of hybrid nanostructure. The "ring-like" structure is formed after selective etching of the undoped Si substrate underneath.

For further investigation of the scrolling behaviour of Cr coating on boron doped Si films, stripes of a Si/Cr bilayer with 35 nm/10 nm thickness have been patterned into a wagon wheel pattern [65], consisting of tapered mesa lines with a width of 1.4 μm in the outer most region and 60 nm close to the centre of the wheel. Figure 4.18 shows an SEM image of the rolled-up Si/Cr stripes obtained from the wagon wheel pattern. Clearly, without exception all these stripes are coiled in the direction along the longitudinal axis of stripes. Comparing the experiments done with SiGe/Si/Cr, SiGe/Si and Si/Cr, possibly indicates that the Cr layer is responsible for the change in the helicity angle and the pitch observed in figure 4.17. The strained polycrystalline or amorphous Cr layer can be assumed to be an isotropic material, thus inducing no preferential scrolling direction. However, the underlying Si layer is stretched by the scrolling process. This Si layer has an anisotropic Young's modulus, which should effect the preferred scrolling direction. However, experimental observation for thin lines demonstrates an additional effect which apparently overrides the effect of the anisotropic Young's modulus.

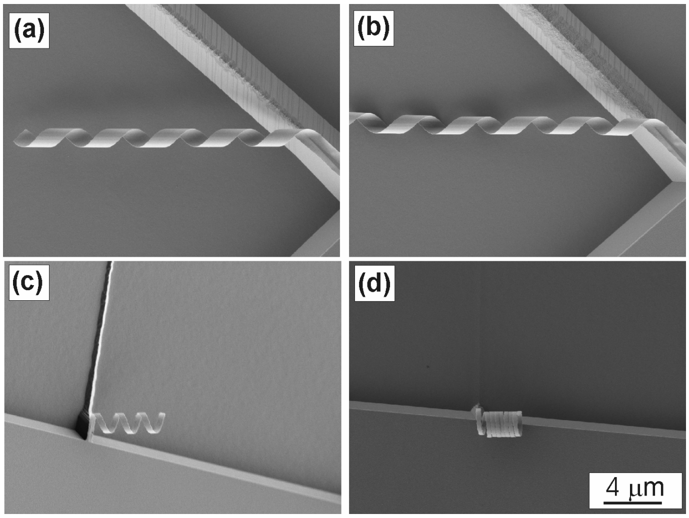

Figure 4.19: SEM images of $Si_{0.6}Ge_{0.4}$*/Si (11/8 nm) helical nanobelts with the same deviation of 5° from <110>, and the stripe width in (a) to (d) is 1.30 µm, 1.20 µm, 0.40 µm and 0.30 µm, respectively. All the images have the same magnification.*

In addition, it has been observed that for thinner Cr layers, the stripe width necessary to switch the helicity of the SiGe/Si/Cr coil from α to β and γ types is reduced. For the bilayers without Cr layer, e.g. $Si_{0.6}Ge_{0.4}$/Si bilayer structures, the α types have been kept until the mesa width is reduced to 700 nm (figure 4.19a-b). It implies that a further reduction of the width is required to observe the helicity changing of the $Si_{0.6}Ge_{0.4}$/Si bilayer structures. Consequently, the width of the mesa lines of the $Si_{0.6}Ge_{0.4}$/Si bilayers was decreased again from 700 nm to 300 nm. The misaligned angle of all stripes is 5° from <110>. The experiment results show that the helices formed by the 400 and 300 nm wide lines are γ type and exhibited a significant decrease in pitch (figure 4.19c-d), indicating a pronounced deviation from the <100> scrolling direction determined by the Young's modulus. This phenomenon is also observed for Si/Cr bilayer stripes as presented in figure 4.20, clearly showing that the scrolling direction changes with the decrease of the stripe width. Thus, it is expected that there is a fundamental effect which significantly impacts the scrolling behavior of SiGe/Si/Cr, SiGe/Si and Si/Cr stripes when the stripe width becomes sufficiently narrow.

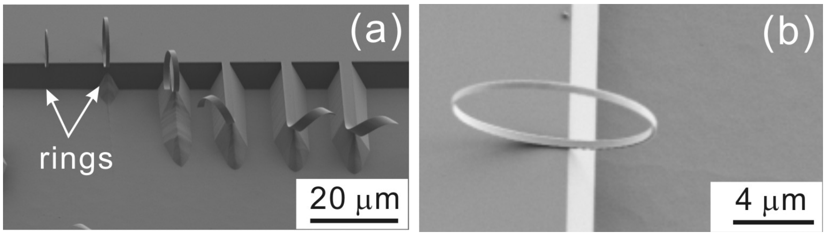

Figure 4.20: (a) SEM image of Si/Cr (35/10 nm) 3D structures, showing the helicity changing with the decrease of the stripe width. The width of the six stripes from left to right is 0.5 μm, 1.0 μm, 1.5 μm, 2.0 μm, 2.5 μm and 3.0 μm. The stripes are aligned 3° deviated from the <110>. (b) SEM image of a Si/Cr (35/10 nm) nanoring. The stripe width is 400 nm and the stripe is 5 degree off from <110>.

The experimental observations for SiGe/Si bilayers and SiGe/Si/Cr film stacks are summarized in figure 4.21, showing the dependence of the diameter and the helicity angle on the width of the mesa lines, respectively. Figure 4.21a-b compared the diameter of SiGe/Si/Cr helices having 21 nm and 10 nm thick Cr layers to that of SiGe/Si helices formed from the mesa lines oriented 5° (see figure 4.21a) and 10° (see figure 4.21b) off from the [110] direction. The diameter d (d=2R) of the SiGe/Si helix can be calculated by Eq. (2.20). When the coiling direction deviates from <100> to the strip orientation <hk0>, the Poisson's ratio of the Si layer decreases [43], leading to an increase in diameter. However, since $0.07 \le \nu_{Si} \le 0.27$ on Si(001), the increase in diameter should be bounded by the limits of the Poisson's ratio. The broken horizontal lines in figure 4.21a-b indicate the maximum$(\nu_{<110>})$ and minimum $(\nu_{<100>})$values of the calculated diameter when these extremes of the Poisson's ratio and corresponding Young's modulus are used. Figure 4.21 demonstrates that α-helices formed by wide mesa lines of the SiGe/Si bilayers are close to the predictions for scrolling along the <100> direction. Also, in the transition regime of β helical nanobelts the diameter is within the limitations given by the Poisson's ratio. However, when the γ type helical nanobelts appear, the diameter increases dramatically and the diameter of helices formed from narrow mesa lines deviates significantly from the model.

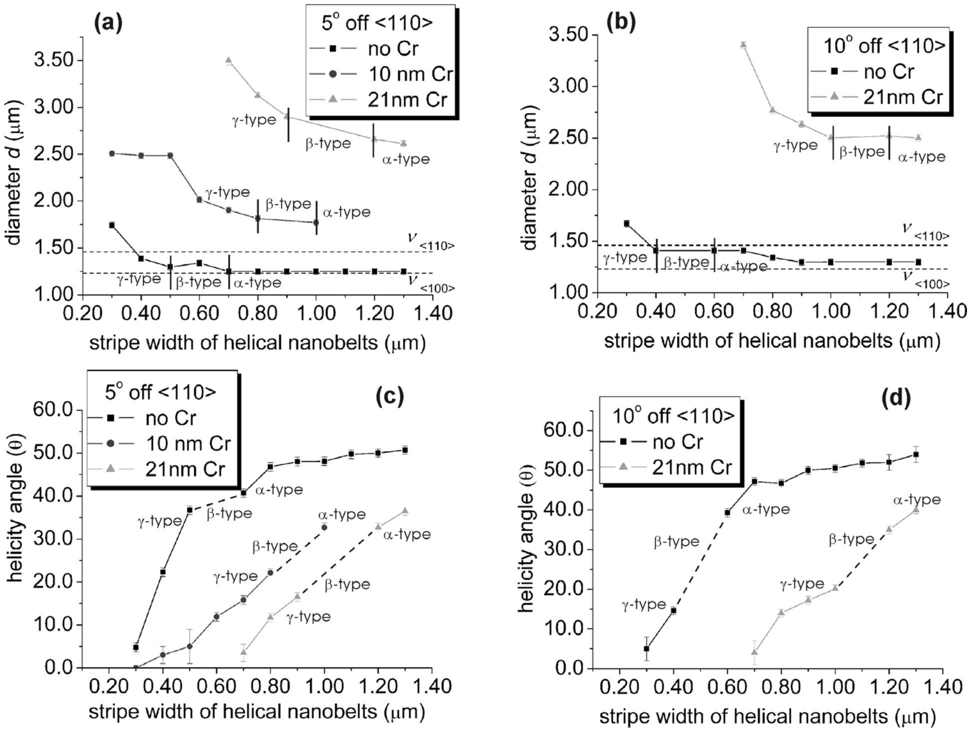

Figure 4.21: Statistical curves showing the relationship between the stripe width and the diameter d for $Si_{0.6}Ge_{0.4}$/Si and $Si_{0.6}Ge_{0.4}$/Si/Cr nanocoils. (a) Stripes deviate 5° from <110>. (b) Stripes deviate 10° from <110>. Dashed lines give the calculated diameter of helical nanobelts which scroll along the <100> and <110> directions. (c-d) The relationship of the stripe width and the helicity angle (θ) for $Si_{0.6}Ge_{0.4}$/Si and $Si_{0.6}Ge_{0.4}$/Si/Cr nanocoils. (c) Stripes deviate 5° from <110>. (d) Stripes deviate 10° from <110>. Dashed lines represent the β-helix region, which has a mixed chirality and irregular helicity.

Figure 4.21c-d give the relationship between the measured helicity angle θ and the stripe width for the same helices previously discussed in the context of figure 4.21a-b. Due to the preferred scrolling direction along the <100> direction in combination with the anisotropic etching, the helicity angles of stripes with a misaligned angle of 5° (see figure 4.21c) or 10° (see figure 4.21d) from <110> should produce coils with helicity angles of 50° and 55°, respectively. Within the experimental error of the SEM measurements this is confirmed by the α-helices. However, the experimental results for β and γ type helices clearly deviate from this prediction. It is evident from figure 4.21c-d that deviation increases with decreasing stripe width and increasing Cr layer thickness. Furthermore, once the γ type helix appears, the helicity angle linearly decreases until rings form from very narrow mesa lines.

The experimental result of the dependence of the curvature radius on Si/Cr stripe width with different bilayer thickness is shown in figure 4.22. Similarly to the SiGe/Si/Cr and SiGe/Si samples shown in figure 4.21a-b, the reversion of the chirality and increase of the curvature radius with the reduced stripe width were also observed. However, after the radius reaches the maximum, the curvature radius decreases almost linearly with the reduction of the stripe width (see figure 4.22), which was not observed in SiGe/Si/Cr and SiGe/Si samples. The reversion of chirality and the increasing of diameter/radius with the reduced SiGe/Si/Cr, SiGe/Si and Si/Cr stripe width are attributed to the stress relaxation at the edge of narrow mesa line. A systematic analysis of this effect will be given in the following content of the section. The opposite trend of radius changing with the decreasing of the stripe width observed on Si/Cr stripe is mainly attributed to the unexpected narrowing of the Si layer in Si/Cr bilayer stripe by etching, which will be discussed in section 4.2.3.

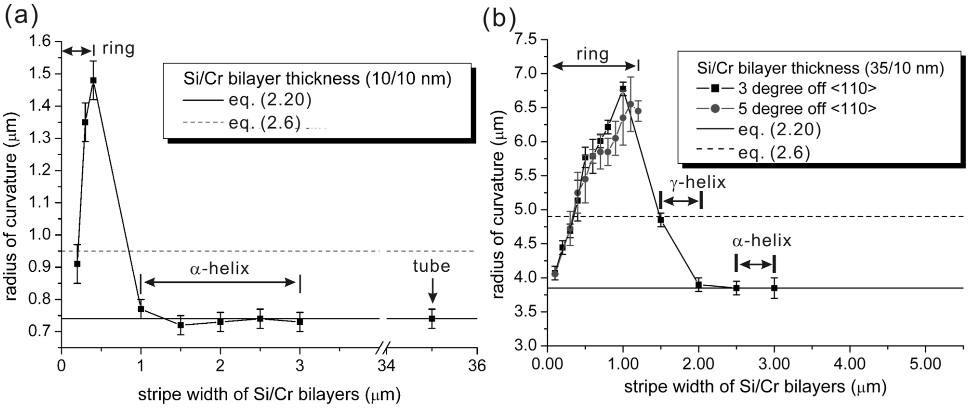

Figure 4.22: Dependence of curvature radius of 3D nanostructures on Si/Cr mesa stripe widths. The stripe width reduced from 3.0 μm to 100 nm. (a) Results obtained from Si/Cr bilayer thickness of 10/10 nm, respectively. (b) Results obtained from Si/Cr bilayer thickness of 35/10 nm, respectively. The horizontal solid lines and dashed lines indicate the calculated curvature radius obtained from the equation (2.20) and equation (2.6), respectively.

4.2.2.2 Finite element analysis of the stress relaxation in narrow mesa lines

It is predicted that at the edges, part of the stress incorporated in the mesa line [71, 72] will relax and, thus, decrease the strain ε. The stress relaxation at the stripe edges is assumed to be more pronounced when the width of the stripe is reduced to nanometer scale and responsible for the observed anomalous coiling of the mesa lines. Finite element method (FEM) simulations (ABAQUS) were used to validate this prediction. For the simulation, a 300 nm wide and 1000 nm long SiGe/Si bilayer stripe with an 8 nm thick Si layer and an 11 nm SiGe layer with 40% Ge concentration was used. As the length should have no influence on the strain (if the length is long compared to the width), the simulation was not done with lengths of 100 μm in favor of having many small and accurate finite elements.

For orthotropic crystal systems ABAQUS uses engineering constants for the elastic properties of the materials (Young's moduli, Poisson ratios, shear moduli). These constants are related to the three mutually orthogonal axes, i.e. *X*, *Y*, *Z*, shown in figure 4.23a. The SiGe/Si bilayer was oriented based on the orientation of *X*=(1-10), *Y*=(110) and *Z*=(001) main axes. The values of the Young's moduli, Poisson ratios and shear moduli related to this main axes system were taken from ref. [43] and shown in table 4.4. The simulation was done also for 5 degree deviation of this orientation.

The mesh in the simulation was defined as follows: 10 units along *Z* axis, 42 units along the *X* axis and 100 units along the *Y* axis, thus there are 42000 finite elements in a 300 nm wide, 1000 nm long and 19 nm thick stripe totally. According to the FEM simulations, the displacement of the nodes of the finite elements increases linearly with the distance from the center line of the stripe. For instance, the lattice displacement in the *X*-direction at the edges of the SiGe stripe is about 1.24 nm at each side of the stripe as shown in figure 4.23. Thus, the FEM simulations show that the stress in the SiGe layer is partially relaxed along the width direction of the stripe, i.e. *X*-direction. Moreover, our FEM also show that (see figure 4.24) when the stress is transversely relaxed at the edge of the stripe, it has biaxial bending at the edge of the stripe and forms a gutter-like structure instead of a flat cantilever. In other words, cylindrical scrolling (uniaxial bending condition) will only exist in the region close to the longitudinal centerline of the stripe and this region will decrease as the stripe width reduced. The simulation for stripe with 5 degree off from the <110> shows very similar results.

Table 4.4: The materials properties for Si and SiGe layer using X=(1-10), Y=(110) and Z=(001) as the main axes.

Si-layer	Young's modulus (GPa)		
	$E_y=E_{(110)}=170$	$E_z=E_{(001)}=130$	$E_x=E_{(1\text{-}10)}=170$
	Poisson ratio		
	$\nu_{yz}=\nu_{(110),(001)}=0.36$	$\nu_{yx}=\nu_{(110),(1\text{-}10)}=0.36$	$\nu_{zx}=\nu_{(001),(1\text{-}10)}=0.28$
	Shear modulus (GPa)		
	$G_{yz}=G_{(110),(001)}=80$	$G_{yx}=G_{(110),(1\text{-}10)}=51$	$G_{zx}=G_{(001),(1\text{-}10)}=80$
SiGe-layer	Young's modulus (GPa)		
	$E_y=E_{(110)}=139$	$E_z=E_{(001)}=103$	$E_x=E_{(1\text{-}10)}=139$
	Poisson ratio		
	$\nu_{yz}=\nu_{(110),(001)}=0.36$	$\nu_{yx}=\nu_{(110),(001)}=0.03$	$\nu_{zx}=\nu_{(001),(1\text{-}10)}=0.27$
	Shear modulus (GPa)		
	$G_{yz}=G_{(110),(001)}=68$	$G_{yx}=G_{(110),(1\text{-}10)}=41$	$G_{zx}=G_{(001),(1\text{-}10)}=68$

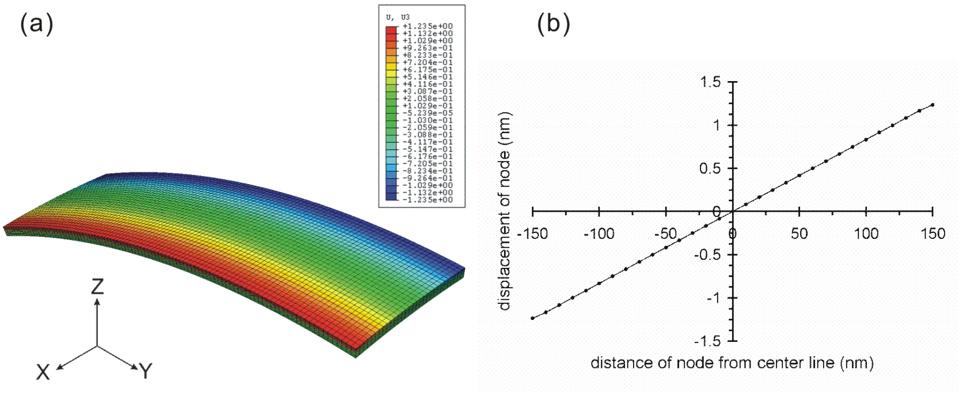

Figure 4.23: (a) Displacement contour plot of the FEM of the SiGe/Si bilayer stripe along the direction X=(1-10). The SiGe/Si bilayer stripe has a thickness of 19 nm (8nm Si/ 11nm SiGe), a width of 300 nm, a length of 1µm and is aligned to <110>. In the simulation, the top layer is the SiGe layer for the easy inspection. (b) Line plot of the displacement in the X-direction of the FEM nodes from the stripe front top edge.

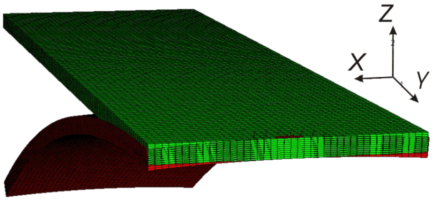

Figure 4.24: FEM simulation of the bending state of a SiGe/Si bilayer stripe, in which the stripe is not only bending along the Y axis, but also along its short axis slightly, i.e. X axis

4.2.2.3 Mechanism of chirality reversion

The strain condition in the helical nanobelts is quite complex. The scrolling process relaxes the strain only in the direction of scrolling where it does not affect the strain in the perpendicular direction. The FEM simulations in the last section show that at the edges the strain will partially relax in the direction perpendicular to the longitudinal axis of the mesa. This relaxation process does not depend on the width of the mesa line used for the helix fabrication. However, the ratio between strained and relaxed material will decrease with decreasing of the stripe width. It appears obvious that the stress relaxation leads to diameter increasing of helical nanobelts with width decreasing of the stripes (see figure 4.21a-b), however, an explanation of chirality change still requires a more detailed discussion of the phenomena related to the stress relaxation.

In the case of microcoils, whose edge effects can be neglected due to the relative large width in a micrometer scale, one can get $F_{[010]}>F_{[100]}$ if the stripe is ϕ degree off from <110> as defined (also for $F_{[010]}$ and $F_{[100]}$) in figure 4.25a because of the magnitude of $F_{[010]}$ and $F_{[100]}$ is proportional to the length of b_1 and b_2, respectively (see eq. 2.3 and eq. 4.3-4). When the stripe becomes narrower, the difference in absolute values between b_1 and b_2 becomes smaller, thus the difference for the forces $F_{[010]}$ and $F_{[100]}$ becomes smaller as well. However, the reversion of the scrolling direction (chirality) to form a γ type helix still requires a driving force along a direction other than the original [100] along which the conventional microcoils scroll. This force is then found arising from the perpendicular stress relaxation at the two edges of the stripe in a nanometer scale. As the FEM analyses showed, the crystalline structure near the edge tends to be relaxed in the direction perpendicular to the mesa line since the atoms at the rim can move outward, whereas little or no relaxation will occur along the longitudinal direction of the mesa line. Consequently, this asymmetrical relaxation induces a force $F_{[hk0]}$, which is directed along the mesa line, as shown in figure 4.25b. The force $F_{[hk0]}$ can be decomposed into components of $F'_{[010]}$ and $F'_{[100]}$ as illustrated in figure 4.25b. Notably, for the same orientation angle ϕ of the mesa line as shown in figure 4.25a and in figure 4.25b, force $F_{[010]}$ is larger than $F_{[100]}$, whereas $F'_{[010]}$ is smaller than $F'_{[100]}$. The difference between $F'_{[010]}$ and $F'_{[100]}$ is independent of the mesa line widths, whereas the difference of $F_{[010]}$ and $F_{[100]}$ decreases with the width of the mesa line. Thus, it is proposed that the change in chirality occurs when

$$\left| F_{[010]} - F_{[100]} \right| < \left| F'_{[010]} - F'_{[100]} \right| \qquad (4.6)$$

Furthermore, adding a strained isotropic film, such as the Cr film, will increase the effect of $F_{[hk0]}$ [72], leading a more pronounced change of the helicity, which is in a perfect agreement with the experimental observations. It is reasonable to expect that the change in chirality could occur even for a relatively wide mesa if a relatively thick Cr layer is incorporated in the layer stack (see figure 4.21a-b).

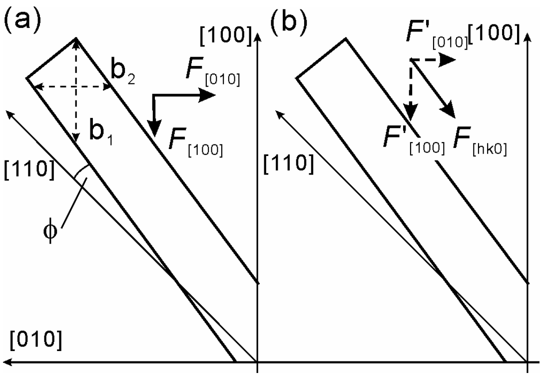

Figure 4.25: A schematic drawing for the explanation of the change of the chirality. The SiGe/Si stripe has ϕ degree off from [110]. (a) The lengths b_1 and b_2 are the lengths of the lines that intersect the mesa line along the [100] and the [010], respectively. (b) $F_{[hk0]}$, which is induced by asymmetrical stress relaxation, can be decomposed into $F'_{[010]}$ and $F'_{[100]}$, and $F'_{[010]} < F'_{[100]}$.

By using this model, the dramatic reducing of the pitch (figure.4.17e and f) and the helicity angle (see figure 4.21c-d) of a nanocoil is also explained. The pitch decreases, i.e. the helicity angle decreases with decreasing mesa line widths. If the SiGe/Si/Cr or SiGe/Si stripe width becomes narrow enough, the scrolling direction is near the stripe longitudinal axis [hk0] instead of the <100> direction. Due to the relaxation of strain perpendicular to the mesa line orientation, the material at the edges of the mesa line can be considered as harboring predominantly uniaxial strain along the mesa line. This uniaxial strain component will induce the force $F_{[hk0]}$, i.e. a moment for scrolling in the direction parallel to the mesa line. Consequently, in the mesa lines used for the fabrication of helical nanobelts, a biaxial strain condition in the center of the mesa line and a uniaxial strain condition at the sides of the mesa line exist. The latter is independent of the mesa line width, whereas the former decreases with line width. The area under biaxial strain induces a preferred scrolling direction along <100> directions, whereas the uniaxial strain at the edges prefers scrolling the stripe in the direction parallel to the mesa line. Therefore the final scrolling direction will be determined by the sum of the components of forces $F_{<100>}$ along one of the <100> directions and the force $F_{[hk0]}$ along the mesa sides. For a narrow stripe this leads to a reduction of the helicity angle, i.e. the scrolling direction is shifted from the <100> directions towards the [hk0] orientation of the mesa line. The experimental results proved that for very narrow Si/SiGe mesa lines (<300nm) $F_{[hk0]}$ will become dominant and the structure scrolls into a multiwall ring along the mesa line.

Based on our results it can be also concluded that when the stripe width is decreased, the Cr coated helices will change the nature of helicity (α, β and γ) at a larger stripe width than that without Cr. The stress contribution of a Cr film can be considered to be isotropic, thus it will not induce a preferred scrolling direction. However, the strained Cr film will relax at the edges as well, adding uniaxially strained material at the edges without adding a moment in the <100> directions, thus $F_{[hk0]}$ increases whereas $F_{<100>}$ remains the same.

4.2.2.4 Deviation of curvature radius from the calculation model

It is shown in figure 4.21 that the radius increases dramatically and that the value of the radius of helices deviates significantly from the calculation based on Eq. (2.20) when the stripe is narrow enough. Investigation is also performed for Si/Cr bilayers (figure 4.22). Based on the rather uniform curvature radius of the α-helices as showed in figure 4.22a, the misfit strain ε is estimated according to Eq. (2.20). Here Poisson's ratio value of the

Si layer is used for calculation. The Young's modulus of Si, Cr and the Poisson's ratio of the Si are given by $E_{\mathrm{Si(100)}}$=130GPa, E_{Cr}=377GPa and v_{Si}=0.27 respectively [43]. According to figure 4.22a, when R=0.74 μm, $h_1=h_2$=10 nm the tensile strain ε of the Cr layer on the Si layer is worked out to be 1.5%. By applying Eq. (2.20) and put the strain value of 1.5% and the thickness of Si/Cr bilayer with 35/10 nm in the equation, a yield radius of the cylindrical coiled structure is 3.8 μm (see the horizontal solid line in figure 4.22b), which fits the experimental results very well when the stripe width is larger than 2 μm. Based on Eq. (2.6), the calculated maximum curvature radius of the structure is about 0.95 μm and 4.9 μm for the stripes with bilayer thickness of 10/10 nm and 35/10 nm, respectively (see the horizontal dashed lines in figure 4.22). However, the experimental results show that the maximum curvature radius of Si/Cr nanorings is still about 40%-60% larger than the prediction. The same phenomena were reported from other coiled bilayer mesa line as well [73]. Takagaki *et al.* reported that the AlN/GaN bilayer stripe with 1 μm width has much less mismatch strain (0.99%) than the expected value (2.37%) resulted from plastic relaxation of the strain at the interface of the bilayer [73]. Thus, we assume that the unexpected extra increasing of the radius is resulted from the same reason. However, which factor exactly leads to the plastic relaxation is still not clear at the moment. By applying the experimental results of the maximum curvature radii from figure 4.26a and figure 4.26b, the misfit strain is reduced from 1.5% to 0.75% and 0.85% respectively.

4.2.3 Si/Cr bilayer nanospirals

To explain the phenomenon that the diameter is decreased with the reduced stripe width in figure 4.22, attention has been paid to the edges of the mesa line again. Careful SEM observations reveal that the p-type Si layer is laterally underetched typically 10-20 nm more than the Cr layer (see figure 4.26a inset and schematic drawing in figure 4.26b). It is presumable that this narrowing occurs because the p-type Si film is attacked during the RIE and wet etching processes, whereas the Cr layer maintains the same width. Moreover, it has been reported that the tensile stress at a polysilicon-oxide interface can enhance spontaneous etching of the poly-Si layer [74]. The tensile stress at a Si/Cr interface may induce a similar effect in the Si layer. The observation indicates that the ratio of Si to Cr material does depend on the width of the stripe and changes in the favor of the Cr material. We make the narrowing of the Si layer responsible for the change over from the Si to the Cr dominated scrolling of the stripes with decreasing stripe width.

This effect offers the possibility to fabricate planar nanospirals by using tapered mesa lines as shown in figure 4.26. It is observed in figure 4.26a that the turning radius gradually increases with the width of the mesa stripe. Figure 4.26c presents an SEM image of the rolled-up structure by etching a tapered mesa line in longer time, showing that when the width of a Si/Cr bilayer stripe is gradually reduced in the direction from the fixed end to the tip of the stripe, the freestanding structure is transformed correspondingly from α-type helix (left handed) to γ-type helix (right handed), and eventually to an nanospiral.

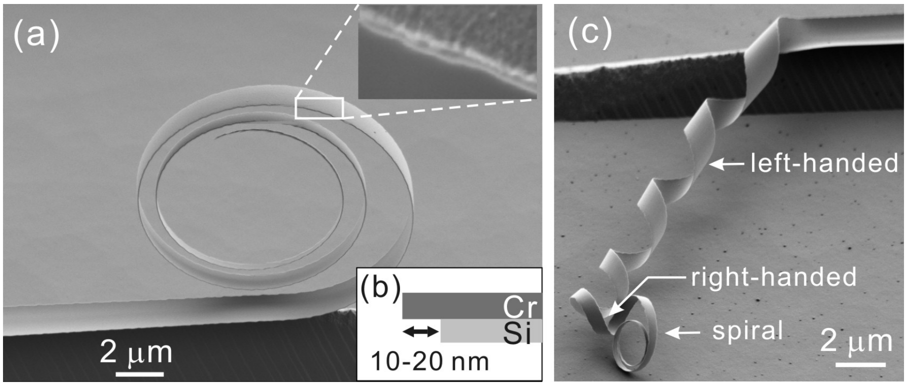

Figure 4.26: (a) SEM images of a freestanding Si/Cr (35/10 nm) spiral nanobelts fabricated from a tapered mesa line. Inset visualizes the 15 nm wide Cr overhang at the rim of the Si/Cr bilayer. (b) Schematic drawing of the cross section profile of the Si/Cr bilayer spiral. (c) SEM image of a 3D structure made from a tapered Si/Cr (10/10 nm) stripe. When the stripe width reduces, the structure transformed from a left-handed helix to a right handed helix and finally to a spiral.

The force F leading to the bending moment can be expressed by [75]:

$$F = \varepsilon b \frac{h_1 h_2 E_{Si} E_{Cr}}{h_1 E_{Si} + h_2 E_{Cr}} \qquad (4.7)$$

in which ε is the misfit strain, E is the elastic modulus, h gives the layer thickness, and b is the width of the stripe along the scrolling direction. According to Eq. (4.7), the rolling-up force F for a narrow stripe decreases proportionally with reduced stripe width b. The bending moment M is given by [41]:

$$M = F\left(\frac{h_1 + h_2}{2}\right) \qquad (4.8)$$

The curvature of the stripe κ can be described as [75]:

$$\kappa = \frac{M}{EI} = \frac{F(h_1 + h_2)}{2(E_{Si}I_{Si} + E_{Cr}I_{Cr})} \qquad (4.9)$$

In Eq. (4.9), EI is the stiffness of the stripe for bending, which is proportional to the bilayer stripe width b [75]. In the ideal case, the Si and Cr layers should have the same width, so the curvature κ is independent of b. However, since the width of the Si layer is smaller than that of the Cr layer due to the lateral underetching of the Si at the edges, the actual EI is smaller than the ideal value, thus the counter moment for bending decreases. Although the relaxation could occur at both edges of Si and Cr layers, it is expected that the strain in the freestanding part of the Cr layer would remain in a certain extent, which could lead to the curvature κ increase. This effect becomes more pronounced when the bilayer width is sufficient narrow.

4.2.4 Conclusions

Anomalous scrolling of SiGe/Si, SiGe/Si/Cr and Si/Cr helical nanobelts (β and γ types) has been observed. The nature of the helicity of the nanocoils differs from helical micro-structure (α helix). Two factors dominate the chirality of a helix formed on Si(100): the different bending moment between the two <100> directions, and the impact of strain relaxation at the sidewalls of the mesa lines. The anomalous coiling of narrow mesa lines can be used to tune the chirality, pitch and helical angle for the nanohelices. Adding films with an isotropic Young's modulus such as amorphous or polycrystalline metal can also be used to tailor these parameters. Using this technique, helical nanobelts with a helical angle of less than 10° can be achieved, which is much smaller than the previously reported minimum 45° given by the preferred <100> scrolling direction. The systematic investigation of curvature dependence on the stripe width shows that if the stripe width is below 1 μm, the diameter of the rolled-up structure is increasing with reduced stripe width due to the stress relaxation at the stripe edges. Our above new findings have provided more opportunities in design and fabrication of 3D nanostructures for more realistic applications.

Chapter 5

Conductivity measurements of freestanding SiGe/Si microtubes

5.1 Introduction

In the previous chapters, we have introduced various three-dimensional (3-D) micro-/nanostructures, such as micro-/nanotubes, helical nanobelts, nanorings and nanospirals, which have been fabricated by rolling of strained semiconductor thin films in a highly controllable fashion. In this chapter, the conductivity of the as-fabricated freestanding SiGe/Si microtubes heavily doped with boron is examined and also discussed.

5.2 Experimental method for conductivity measurement

In the experiments for electrical property investigation, samples of boron doped SiGe/Si microtubes were fabricated on n-type Si(100) substrates with high resistivity (10kΩ·cm) to minimize the effect of current leakage in the substrate. Metal electrodes with ohmic contacts to the tubes were prepared. Three different types of metals, i.e. Al, Cr and Au have been considered and tested. Among them, Al is frequently used as an interconnection material in Si microelectronics [47], however, it usually has a low etching resistance to alkaline solutions such as KOH. Campbell et al. reported that Al could have better chemical resistance in ammonia hydroxide water (AHW) solution, which is attributed to the formation of a sparingly soluble pyrophyllite-type silicate passivation layer to prevent the further attack to the aluminium surface [58]:

$$2H_2Si_2O_5 + 2Al(OH)_3 \rightarrow Al_2(OH)_2(Si_2O_5)_2 + 4H_2O \qquad (5.1)$$

In this process, a minimum concentration of Si dissolved in the AHW solution is required for the passivation [58]. On the contrary, Cr is chemically much more stable than Al, and of low electrical resistivity, while Au has better electrical conductivity than Al but poor adhesion to a Si surface. To improve the adhesion, a thin interlayer of Cr (10 nm thick) can be alternatively deposited between the Au layer and the Si surface. Our experimental results showed that 300 nm thick Al contacts were unstable and would be etched away gradually when the patterned SiGe/Si bilayers were released from the substrate in the 3.7% AHW solution, whereas Cr and Cr/Au bilayers contacts are very stable. One drawback of the Cr/Au contacts is that, during etching process, the sample surface becomes very rough; the reason is not clear at the moment. Thus, mainly Cr was used as the contact material for the reliability.

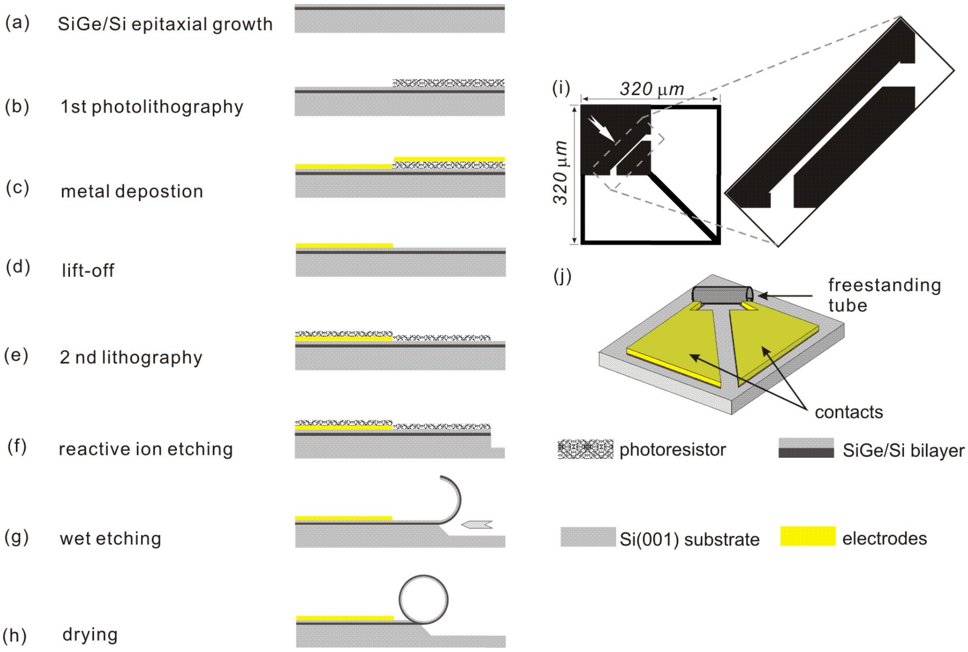

Figure 5.1: Fabrication flowchart of a freestanding SiGe/Si microtube with two metal contact pads for resistivity measurement.

To prepare a device for conductivity measurement of SiGe/Si microtubes, a two-step photolithographic patterning process has been adopted after deposition of the p-type SiGe/Si bilayer by UHV-CVD as follows. Firstly, lift-off processes are employed to coat metal contacts on the SiGe/Si bilayer (figure 5.1a-d). In detail, photoresist S1813 is spin-coated on the sample surface and followed by a photolithography, then a 300 nm thick metal layer is deposited on the top of the sample. After the sample is rinsed in remover solution to dissolve the S1813 together with the coated metal layer above the photoresist, patterned contacts on part of the sample surface are obtained. The second photolithography process is used to pattern the SiGe/Si bilayer for tube fabrication. To do so, the sample surface was coated with S1813 again, and then the pattern was transferred from a photomask to the S1813 layer (figure 5.1 e) by the second lithography. This pattern is further transferred to the SiGe/Si bilayer and Si substrate by the followed reactive ion etching (RIE) as shown in figure 5.1 (f). Finally, the device for conductivity testing of tubes are prepared by wet etching and drying processes as shown in figure 5.1(g-h). Figure 5.1(i) depicts a pattern design of the SiGe/Si bilayer on a Si substrate. Figure 5.1(j) illustrates the configuration of the device, consisting of a freestanding SiGe/Si microtube and two contacts.

A two-probe method is adopted in the following experiments to measure the electrical conductivity of the tubes: a variable DC bias is applied to a tube through two probes made of stainless steel, which are inserted into the metal contacting pads with ohmic contact. Then I-V curve between the two probes is recorded from the applied voltage and the measured current passing through the tube. Note that the electrical resistance between the probes and the contacts is very small (only several ohms), thus the voltage drop from the contacting is negligible. In order to ensure the reproducibility of the experimental data the measurement of each I-V curve was conducted for at least two times.

5.3 Conductivity of individual SiGe/Si microtubes

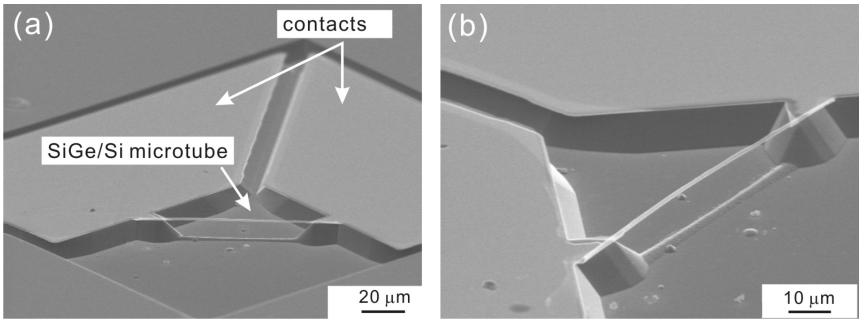

Figure 5.2: SEM images of a freestanding SiGe/Si microtube for two-probe measurement. In this sample, Cr is used as metal contacts.

Figure 5.2 shows SEM images of a typical device: a freestanding microtube connected with Cr contacts. Four SiGe/Si microtubes, with the same diameter of about 1.25μm and different total lengths of 90 µm, 100 µm, 110 µm and 120 µm, were used for the testing. The thickness of the SiGe and Si layers of the tubes is about 11 nm and 8 nm respectively, with 40% Ge in the SiGe layer. The measured I-V curves of these four microtubes are presented in figure 5.3, they all show linear relations between the current and the applied voltage within a range of -1V to 1V. Thus, the total resistance R_t of each tube can be calculated from the slope of the curves in figure 5.3 by applying Ohm's law, i.e. the ratio of the applied voltage and the measured current. The measured resistance R_t between two probes is 11.7 kΩ, 14 kΩ, 16 kΩ and 18.5 kΩ, respectively. Since the resistance of the metal probes to the Cr contact layers is negligible, the total resistance between the two probes is the sum of two components: (1) the total contact resistance $2R_c$, and (2) the resistance of the SiGe/Si microtube R_{tube} [76]:

$$R_t = 2R_c + R_{tube} \qquad (5.2)$$

The linear dependence of the measured current and voltage indicates that the heavily doped SiGe/Si bilayers behave like resistors. To calculate the contact resistance R_c, transmission line model (TLM) is applied [76]. Apparently, the resistance of tube (R_{tube}) is related to the resistivity (ρ), the spacing between two contacts (S_{tube}) and the cross sectional areas A of the tubes, giving the total resistance as:

$$R_t = 2R_c + \rho \frac{S_{tube}}{A} \qquad (5.3)$$

Thus, the conductivity of a SiGe/Si microtube, which is the reciprocal value of the resistivity ($\sigma = 1/\rho$), can be calculated. The cross section of the tubes calculated from the width (4.0 µm) and thickness (19 nm) of pattered bilayers is $A = 4 \cdot 10^{-4} \cdot 1.9 \cdot 10^{-6}\, cm^2 = 7.6 \cdot 10^{-10}\, cm^2$. As an approximation based on the TLM, the shortest contact spacing, i.e. $S_{tube} = L_s$ (see figure 5.4a), is first used as a nominal length of the tube in the following calculation, assuming all the current flows through the front-edge of the contact, e.g. point "a" in figure 5.4b. The contact spacing of four individual tubes ($S_{tube} = L_s$, see figure 5.4a) is 60 µm, 70 µm, 84 µm and 94 µm, respectively. Using linear fitting, a curve of the total resistance R_t versus the shortest contact spacing (L_s) of the microtubes is drawn in figure 5.5a. According to Eq. (5.2), letting L_s to zero, $2R_c$ can be measured from the intersection of the linear R_t *versus* L_s curve with the y-axis by extrapolation. Thus, $2R_c = 288\ \Omega$ is obtained as illustrated in figure 5.5a. This value is about two orders of magnitude smaller than R_t, indicating the nature of ohmic contact between the Cr contacts and the highly boron-doped bilayers. Using Eq. (5.2), the respective resistivity (ρ) of 1.45 mΩ·cm, 1.49 mΩ·cm, 1.42 mΩ·cm and 1.47 mΩ·cm for the four tubes is obtained. Thus, an average resistivity of about 1.46 mΩ·cm, corresponding to a conductivity (σ) value of 686 $\text{S}\cdot\text{cm}^{-1}$, is worked out for the tubes. As a comparison, the contact spacing (L_s) is replaced by the full length (L_t, see figure 5.4a) of tubes in the calculation of the conductivity, then lengths of 90 μm, 100 μm, 110 μm and 120 μm are used for the four tubes respectively in Eq. (5.2). A negative contact resistance is resulted as shown in figure 5.5b. The significant difference in the calculated contact resistance implies that the calculation of contact resistance R_c based on the TLM is very sensitive to values of S_{tube} and R_t. It means that slight deviation in the value of contact spacing S_{tube} or of experimentally measured R_t can result in a large error of the calculated R_c, especially when R_c is small [76, 77]. Letting the current flow from the left contact to the right one as illustrated in figure 5.4, since the metal Cr layer has much lower resistivity than the thin Si and SiGe layers, it is expected that the current density J_a flowing from front-edge "a" of the contact is much higher than the current density J_b flowing from end-edge "b" of the contact (see figure 5.4b). The analysis of two dimensional current flow into and out the lateral contacts made by Kennedy and Murley has revealed that only a fraction of the total contact length in the front edges was active during the transfer of current from the metal to the semiconductor or from the semiconductor to the metal due to the current crowding at the front-edges of contacts [76, 78]. Assuming the contact resistance is zero, this fraction was found to be approximately equal to the thickness of the diffused semiconductor sheet [76, 78], i.e. about 19 nm in the case of our experiments. Therefore, comparing above two calculated results for R_c, the first one (using the shortest contact lengths L_s) is considered to be much closer to the real situation. It should be noted that the model (TLM) used here to calculate the contact resistance is a simple one-dimensional (1-D) model. In the reality, R_c is related to the layout dependent non-uniform current flow pattern [77]. Thus, for more accurate calculation of R_c, using 2-D or 3-D simulation may be required [77] although it is not so necessary here for only an approximate evaluation .

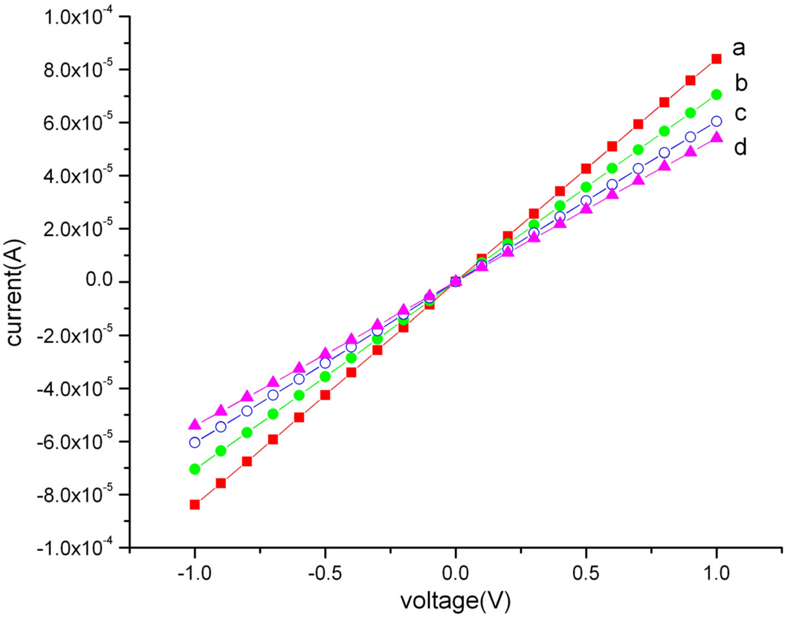

Figure 5.3: The measured I-V curves of the four freestanding SiGe/Si tubes with a diameter of about 1.25 μm. The four curves, marked with a, b, c and d, are measured from the tubes with a total length of 90, 100, 110, and 120 μm respectively. All four tubes show linear feature of the I-V curves in the voltage range from -1V to 1V. The resistivity of Si substrate is 10 kΩ·cm. At the two ends of the freestanding tube, two Cr electrodes are connected.

Theoretically, the conductivity of a p-type semiconductor can be expressed as:

$$\sigma = pq\mu \tag{5.4}$$

in which p is the doping level of a heavily doped semiconductor, q is the unit of electric charging (q=1.6x10^{-19} C) and μ is the mobility of holes. Before scrolling to form a tube, the SiGe/Si bilayer can be considered separately as a rectangular Si sheet and a SiGe sheet connected to each other in parallel as shown in figure 5.6. Thus the total resistance ($R_{SiGe/Si}$) of the bilayer can be expressed as a function of resistances of the Si layer (R_{Si}) and the SiGe layer (R_{SiGe}):

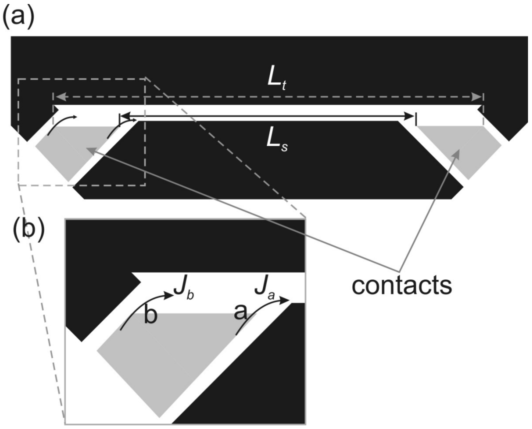

Figure 5.4: Schematic diagram to show the local current density at the contacts. (a) L_t is the total length of the tube and L_s means the spacing between two front-edges of the contacts. (b) J_a represents the current density at the contact front-point "a", while J_b represents the current density at the contact end-point "b". The current is assumed flowing from the left contact to the right one.

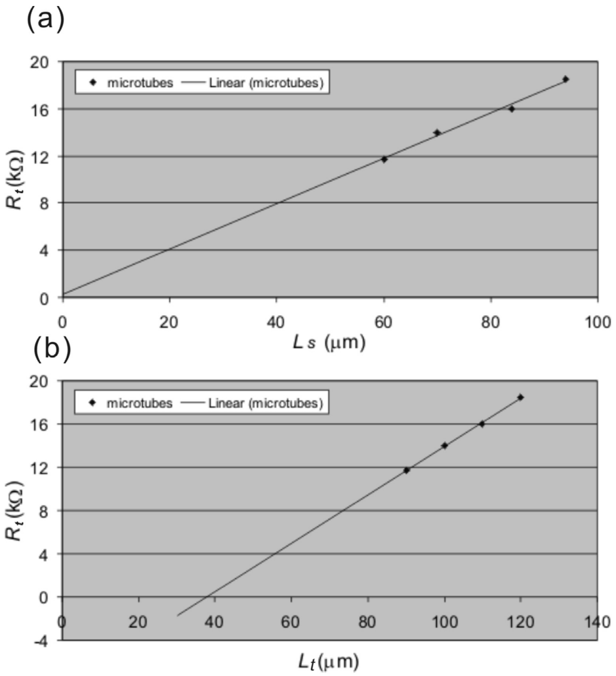

Figure 5.5: (a) The experimental curve of the total resistance R_t versus the shortest contact spacing (L_s) of the microtubes. By extrapolation, contact resistance $2R_c$ can be obtained when L_s=0. (b) The curve of the total resistance R_t versus the total length of microtubes (L_t).

$$R_{SiGe/Si} = \frac{R_{Si}R_{SiGe}}{R_{Si} + R_{SiGe}} \qquad (5.5)$$

By using formula $R = \rho\frac{l}{A}$ and substituting Eq.(5.4) to Eq.(5.5), the conductivity of the SiGe/Si bilayers *($\sigma_{SiGe/Si}$)* can be calculated:

$$\rho_{SiGe/Si}\frac{l}{A_{Si} + A_{SiGe}} = \frac{\frac{l}{p_{Si}q\mu_{Si}}\cdot\frac{l}{p_{SiGe}q\mu_{SiGe}}}{\frac{l}{p_{Si}q\mu_{Si}} + \frac{l}{p_{SiGe}q\mu_{SiGe}}} \qquad (5.6)$$

$$\Rightarrow \sigma_{SiGe/Si} = (\rho_{SiGe/Si})^{-1} = (\frac{A_{Si} + A_{SiGe}}{q(p_{Si}\mu_{Si}A_{Si} + p_{SiGe}\mu_{SiGe}A_{SiGe})})^{-1} \qquad (5.7)$$

in which A_{Si} and A_{SiGe} are the cross sectional areas of the Si and SiGe layers respectively, l is the length of the bilayer. The doping level (p) and the mobility (μ) of the Si and SiGe layers, grown with the same condition as SiGe/Si bilayers, were probed by Hall measurement, i.e., $p_{Si} = 2.03\cdot10^{20}cm^{-3}$, $p_{SiGe} = 4.57\cdot10^{20}cm^{-3}$ and $\mu_{Si} = 24.1cm^{2}V^{-1}s^{-1}$, $\mu_{SiGe} = 12.3cm^{2}V^{-1}s^{-1}$, and the cross sectional areas A_{Si} and A_{SiGe} are calculated as $A_{Si} = 4\cdot10^{-4}\cdot8\cdot10^{-7} = 3.2\cdot10^{-10}cm^{-2}$ and $A_{SiGe} = 4\cdot10^{-4}\cdot1.1\cdot10^{-6} = 4.4\cdot10^{-10}cm^{-2}$. Substituting these values to Eq. (5.7), a conductivity of 850 S·cm^{-1} is resulted. The experimental result (686 S·cm^{-1}) is about 19% lower than this value. Several reasons may lead to the discrepancy of the experimental results from the calculation. Firstly, the value of cross sectional area of the tubes for conductivity calculation may be not precise due to the oxidation of tube surfaces, especially when the wall thickness of the tube is in nanometer scale. Our calculations demonstrated that, for a tube with the wall thickness of 19 nm, the formation of 1 nm thick oxidation layers in each surface of the tube will cause about 11 % reduction of the value of cross sectional area *(A)*, leading to an undervalued conductivity. Taking 1 nm thick oxidation layer in the each surface of the tube as an example, conductivity value of 767 S·cm^{-1} instead of 686 S·cm^{-1} is resulted, which is only 9.8% deviated from the theoretical estimation. On the other hand, during the wet etching, a few monolayers of p-Si layer might be etched away with long etching time. In addition, the accuracy of the contact resistance calculation may also influence the resulted value of the conductivity. For instance, the nominal length of the tube for the calculation may be underestimated by using the shortest contact spacing (L_s) in the transmission line model, resulting in a higher calculated resistivity of the tube.

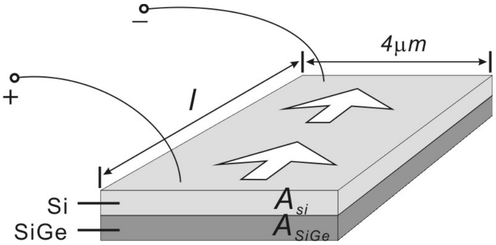

Figure 5.6: The schematic drawing of rectangular SiGe/Si bilayers which have the same width and the thickness to the patterned bilayers for tube conductivity measurement. The bilayers are parallel connected to the electrodes. White arrows point out the direction of the current flow. A_{Si} *and* A_{SiGe} *are the cross sectional area of the Si layer and the SiGe layer respectively.*

It should be pointed out that the measured current is directly used for conductivity calculation of the tube, although it is a sum of the currents from two paths: one from the freestanding tube, and the other from the leakage passing through the Si substrate. The leakage current can be measured in the following way. Firstly, a high bias is applied to burn the tube away, then a lower bias as normally used for measuring the I-V curve was applied (-1V – 1V) to obtain the value of the leakage current. Figure 5.7 shows a tube with a total length of 120 μm was burnt away when the applied bias was higher than 11V, and the current dropped suddenly. A very tiny current still existed after the tube was burnt, resulting from the leakage passing through the substrate. The observed leakage current is three orders of magnitude lower than that passed through the tube, thus can be neglected in the I-V curve.

The electrical stability of the tubes is also probed by applying a constant voltage. It is found that the current is very stable when the applied voltage is lower than 3.5V for SiGe/Si microtubes (figure 5.8a-b). However, when the bias is higher than 3.5V, the current decreases gradually with the time. Especially, if the bias is higher than 5V, the current becomes irregularly fluctuated. This phenomenon is attributed to the high current density in the microtube (> $3.7\text{x}10^5$ A/cm^2), which leads to the joule heating of the tube.

The elevated temperature causes the crystal lattice to vibrate stronger, which will lead to more electrical scattering of electrons. Eventually, the heating energy may even permanently damage the structure of the tube.

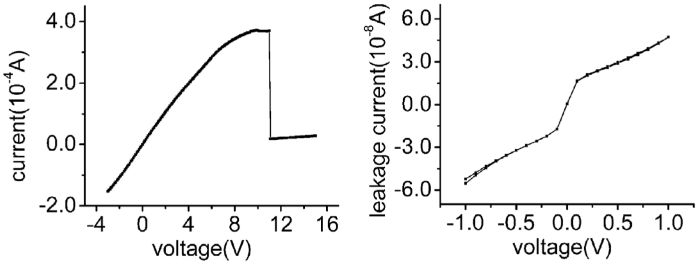

Figure 5.7: To burn out the tube, the voltage applied to a tube with total length of 120 μm was increased from -3V to 15V. (a) The sudden drop of current at about 11V indicates that the tube was burned out. (b) The leakage current is about $5 \cdot 10^{-8}$ *A with the supplied voltage of 1V.*

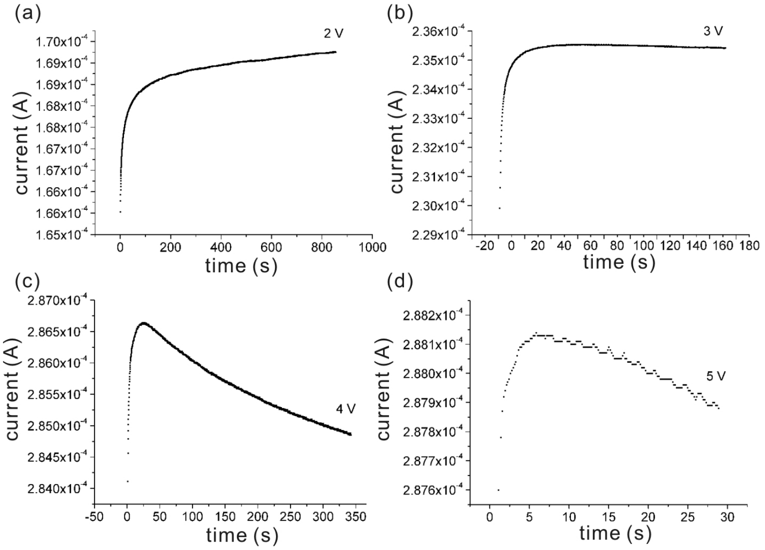

Figure 5.8: The current stability experiment of a SiGe/Si micro-tube on different voltages. The total length of the tube is 100 μm. (a-b): The curves show that the current is stable when the voltage is not higher than 3V. (c): When the voltage is higher than 4V, the current starts to decrease with the testing time. (d): When the voltage is higher than 5V, the current starts to oscillate, implied that the structure of tube is going to be damaged.

5.4 Conclusions

In conclusion, the heavily boron doped SiGe/Si microtubes are very conductive. The measured conductivity is about 686 $S\cdot cm^{-1}$ based on the transmission line model, which is lower than the theoretically calculated result (850 $S\cdot cm^{-1}$). Surface oxidation and thinning of the layer after wet etching have been attributed to the decrease of the resulted conductivity of the freestanding microtubes. The I-V curves show a linear feature in the voltage range of -1V-+1V. When the applied bias is lower than 3.5 V, the current is very stable in the SiGe/Si micro-tubes. Thus, these high conductive rolled-up structures could be utilized as capacitors by sandwich of dielectric layers into the rolled-up structure.

Chapter 6

Mechanical properties of individual SiGe/Si microtubes

Obviously, mechanical properties of the fabricated micro/nanostructures are very important to determine their applications. However, the mechanical properties are not well known yet although the fabrication technique of rolled-up structures is well developed. In this chapter, the bending stiffness of individual SiGe/Si microtubes is probed quantitatively by atomic force microscopy (AFM). Then, nanorobotic manipulation technique has been applied to investigate the elasticity and the compression stability of individual SiGe/Si microtubes. The experimental results are compared with calculations based on an ideal seamless tube model.

One-end-fixed SiGe/Si microtubes are exclusively employed here for testing of their mechanical properties. The fabrication of these one-end-fixed SiGe/Si microtubes is given in chapter 4 (see figure 4.1). The initial planar films consist of SiGe/Si bilayer with a thickness of 11/8 nm, respectively, and about 40% Ge in the SiGe layer. The SiGe/Si tubes have a diameter (*d)* of 1.25 μm and varied freestanding lengths (*L*). For AFM bending tests, SiGe/Si microtubes of 1.2 turns (corresponding to *w*=4.8 μm, see figure 4.1a) were used. In nanorobotic manipulation experiments, microtubes with 1.6 turns (*w*=6.4 μm) were investigated.

6.1 Bending stiffness studied by atomic force microscopy

Recently, processing and manipulation of nanostructures such as carbon nanotubes and zinc oxide nanobelts with AFM have given remarkable results [15, 79-83], for instance Young's modulus, shear modulus, bending stiffness of the nanostructures can be determined by performing bending or buckling test of the samples. Here, AFM is applied for the bending stiffness investigation of the rolled-up tubes.

6.1.1 Measurements and calculations of the bending stiffness

To investigate the bending stiffness of these freestanding tubes, the AFM cantilever is operated in contact mode. In the first step, the AFM cantilever is bent on a flat reference surface of the solid part of the sample by pushing down the cantilever (see figure 6.1a-b). A slope of photodiode signal versus tip displacement curve on the stiff sample surface (N_{stiff}) can be obtained directly (see figure 6.2a). Then the cantilever is mounted on the top of the microtube's free-end under an optical microscope as depicted in figure 6.1c. After that, the AFM cantilever is pushed down on the tube (see figure 6.1d). In this operation, the second slope of the photodiode signal vs. displacement curve related to tube's stiffness can be obtained (N_{tube}, see figure 6.2b). Upon the above two operations, the bending stiffness (k_{tube}) of the freestanding tube can be quantitatively deduced by [1, 84]:

$$k_{tube} = \frac{k_{AFM}}{\frac{N_{stiff}}{N_{tube}} - 1} \qquad (6.1)$$

where k_{AFM} is the spring constant of the AFM cantilever (0.03 N/m in our experiments). The detailed explanation for Eq. (6.1) is given in appendix B.

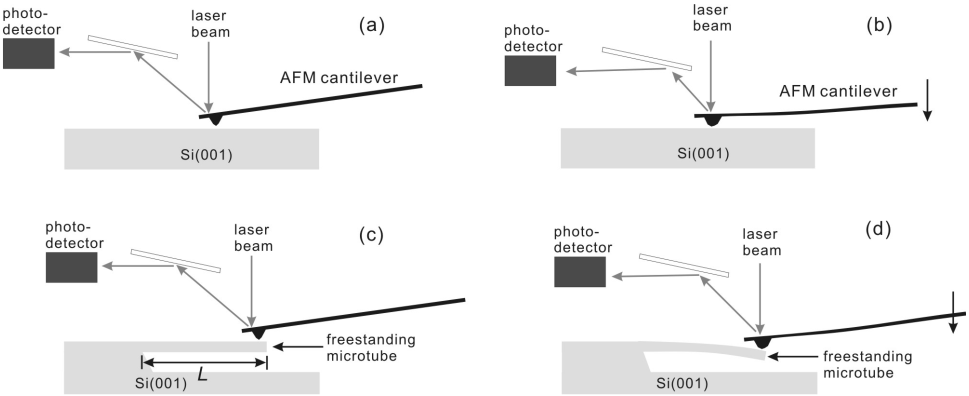

Figure 6.1: Schematic depiction of AFM manipulation of freestanding microtube for bending stiffness measurement. (a-b) AFM cantilever is deformed on a reference surface of the sample to obtain N_{stiff}. (c) AFM cantilever is mounted on the free end of the tube. (d) AFM cantilever is pushed down to deform the tube. Thus, N_{tube} can be obtained from the deformation of the AFM cantilever.

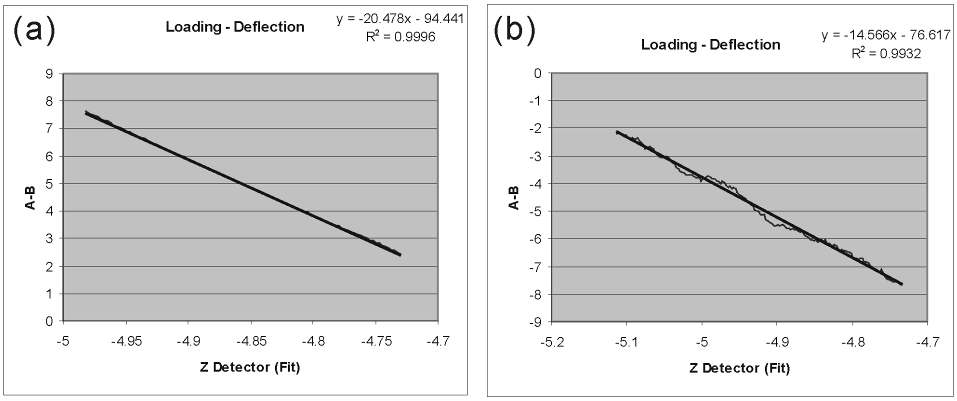

Figure 6.2: Experimental curves of N_{stiff} *(left) and* N_{tube} *(right). The stiffness of the tube can be calculated by Eq. (6.1), if* N_{stiff}, N_{tube} *and* k_{AFM} *are known.*

Table 6.1: Experimental values of bending stiffness of the five tubes. Note that the spring constant of the AFM cantilever is 0.03 N/m.

	tube *a*	tube *b*	tube *c*	tube *d*	tube *e*
L (µm)	47.9	47.9	47.9	68.5	68.5
k_{tube} (N/m)	0.062	0.068	0.034	0.016	0.013

Five SiGe/Si microtubes, divided into two groups according to their freestanding lengths (L), were selected for the bending stiffness tests: three of them are 47.9 µm long (type I) and the other two are 68.5 µm (type II). The experimental results of bending stiffness (k_{tube}) for the five tubes are listed in table 6.1, in which two of the three tubes with the length of 47.9 µm show similar bending stiffness, whereas the third one (tube "*c*") has only half value of the former. The reason for much less bending stiffness of tube "*c*" is unclear, we assume that the structure is somehow damaged during fabrication processing. For the two longer tubes (68.5 µm), the values of the bending stiffness are quite close to each other.

The experimental values of these freestanding microtubes are compared with theoretical calculations by applying a model based on an ideal one-end–clamped beam [42] (figure 6.3a). In this model, the beam is assumed having a uniform ring-shape cross section with a diameter of d and a wall thickness of t (see figure 6.3b-c). When a concentrated load P applied at the free end of this beam, the unit-load method yields [42, 81]:

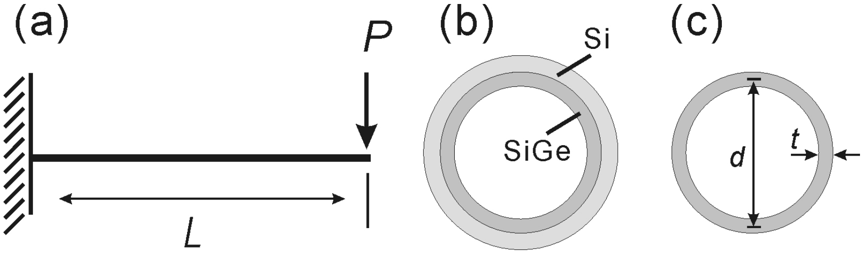

Figure 6.3: (a) The one-end–clamped beam model used for calculation. Column with cross section of ring is assumed in the calculation. (b) For the calculation, the rolled-up SiGe/Si microtube was assumed as a combination of a SiGe tube and a Si tube. (c) The cross sectional area for calculation of the moment of inertia (I), $I = \pi d^3 t/8$ *is resulted.*

$$H = H_B + H_S = \frac{PL^3}{3EI}\left(1+\frac{3f_s EI}{GAL^2}\right) = \frac{PL^3}{3EI} + \frac{f_s PL}{GA} \qquad (6.2)$$

where H is the total deflection of the free end, H_B reflects the deflecting due to bending, H_S is the deflection due to shearing, L is the freestanding length of tube, E is the Young's modulus ($\text{Si}_{<010>}$=130.2GPa, $\text{Ge}_{<010>}$=102.1GPa [85]), I is the moment of inertia of cross sectional area of the tube ($I = \frac{\pi}{8}d^3 t$, with $d>>t$, see figure 6.3c), f_s is the shape factor (equal to 2 for a tube system with thin wall thickness), G is the shear modulus ($\text{Si}_{<010>}$=79.4 GPa, $\text{Ge}_{<010>}$=67 GPa [85]) and A is the cross sectional area. Because E and G are in comparable magnitude, shear modulus becomes important only for a relatively short tube [81]. In fact, shear becomes an important contribution when $L/R \leq 4\sqrt{E/G}$ [42]. Therefore, in our case, shear could be neglected because of the large value of L/R *(>36)*. Then, Eq. (6.2) could be simplified to:

$$H \approx H_B = \frac{PL^3}{3EI} \qquad (6.3)$$

Therefore, the bending stiffness of the tube is given by $k_{beam}=P/H=3EI/L^3$. Since a rolled-up SiGe/Si microtube is composed of SiGe and Si two layers, the bilayer tube can be considered as a composite beam system [42]: a Si tube is combined with a SiGe tube as shown in figure 6.3b. Thus, the bending stiffness of the whole composite tube system (k_{beam}) is expressed as:

$$k_{beam} = \frac{3(E_{Si}I_{Si} + E_{SiGe}I_{SiGe})}{L^3} \qquad (6.4)$$

The geometry parameters and the calculated results for ideal seamless SiGe/Si tubes with the same wall thickness and diameter of the tubes for AFM experiments are shown in table 6.2. For ideal tubes with lengths of 47.9 μm and 68.5 μm, the calculated values of the bending stiffness are 0.049 N/m and 0.017 N/m respectively.

Table 6.2: The theoretically calculated bending stiffness and the related parameters of ideal seamless SiGe/Si tubes having the same wall thickness and diameter of the tubes for AFM experiments

	Type I	Type II
Length (L)	47.9 μm	68.5 μm
Diameter (d)	1.25 μm	1.25 μm
Wall thickness of SiGe layer (h_1)	11 nm	11 nm
Wall thickness of Si layer (h_2)	8 nm	8 nm
E_{Si}	130.2 GPa	130.2 GPa
E_{SiGe} (SiGe, 40% Ge)	119 GPa	119 GPa
$E_{Si}I_{Si}$	0.8*10^{-15} N*m^4	0.8*10^{-15} N*m^4
$E_{SiGe}I_{SiGe}$	1.00*10^{-15} N*m^4	1.00*10^{-15} N*m^4
Bending stiffness (k_{beam})	0.049 N/m	0.017 N/m

6.1.2 Discussion and conclusions

For a clear comparison, both experimental and theoretically calculated results of the bending stiffness for the five 1.2 turns rolled-up microtubes are listed in Table 6.3. It shows that the measured value from AFM experiments is rather diversely distributed and somewhat deviated from the calculations, and that the short tubes ($L=47.9$ μm) have higher measured values than the modeled ones whereas the long type tubes ($L=68.5$ μm) have lower values than the calculations. The diversity of the measured bending stiffness can be explained by the following factors. (1) The error arises from using the freestanding length of a tube as the nominal length to calculate the stiffness of the tube. When the AFM tip was mounted on a tube under the top-view observing of an optical microscope, it is difficult to put the tip exactly at the free-end position of the tube because the viewing direction is blocked by the AFM cantilever. It means that the true value of the effective length measured from the AFM tip to the fixed end of the tube could be a few micrometers less than the apparent length (L) of the tube. According to Eq. (6.4), the calculated value of the stiffness (k_{beam}) is inversely proportional to the cubic power of the length (L^3). Thus, even a small deviation of L will cause relatively large error of the measured stiffness, especially for relatively short tubes. As a result, the measured stiffness is usually larger than the calculation due to the true length is always smaller than the full length of the tube in calculation. Take the tube with a length of 47.9 μm as an example, if the AFM tip is mounted 3 μm away from the free-end of the tube, the measured stiffness will be 21% more than the calculated value. (2) The asymmetric wall shape of a rolled-up 1.2 turns microtube may also affect the accuracy of the measurement. The cross section of the tube is actually not a seamless ring but rather like a spiral as shown in figure 6.4. The overlapped 0.2 turn of the tube has a double bilayer thickness. Thus, the location of this doubled wall in the circumference of the tube sometimes becomes crucial as demonstrated in figure 6.4. For example, if the position of the thicker wall is completely down as shown in figure 6.4a, the tube would show a relatively high stiffness when the AFM tip applies a force on the top surface of the tube, even higher than the ideal one. However, if the seam (the doubled wall) is located in other places of the tube, e.g., 90 degree rotated from the former position as shown in figure 6.4b, the bending stiffness becomes apparently smaller because the average distance from the doubled layer to the neutral plane of the bent tube is smaller than the former case. FESEM inspection revealed that the seam may rotate along the tube axis of the one-end-fixed tube as shown in figure 6.5, indicating that the location of the overlapped wall is also varied. The rotation of the seam is probably caused by two factors: on the one hand, along the *CD* side of the pattern (see figure 4.1a), the bilayer cannot scroll at the point *D* while the bilayer near the point *C* is free for scrolling; on the other hand, the orientation of *AB* and *CD* sides may have 1-2 degree of misalignment angle to the <100> direction, which leads to the rotation of the seam. This phenomenon is more pronounced for long tubes, which could affect the accuracy of measured stiffness. (3) Other factors to influence the stiffness may also exist, such as the ellipse deformation of the tube and local structure defects, resulting in a lower stiffness of the tube as showed in the case for the long tubes. More precise results can be expected if finite element modeling is performed for the simulation.

Table 6.3: Bending stiffness comparison of the experimental results to the calculations

	tube *a*	tube *b*	tube *c*	tube *d*	tube *e*
calculation	0.049	0.049	0.049	0.017	0.017
AFM results	0.062	0.068	0.034	0.016	0.013
deviation	+27%	+39%	-31%	-6%	-24%

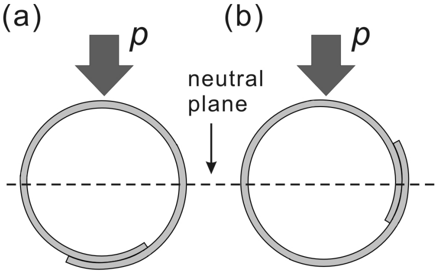

Figure 6.4: When the AFM tip is pushed on the different position of the rolled-up tube (1.2 turn), the measured bending stiffness would be different. The top arrows represent the load P from AFM and the spirals below are models for the cross section shape of rolled-up tubes.

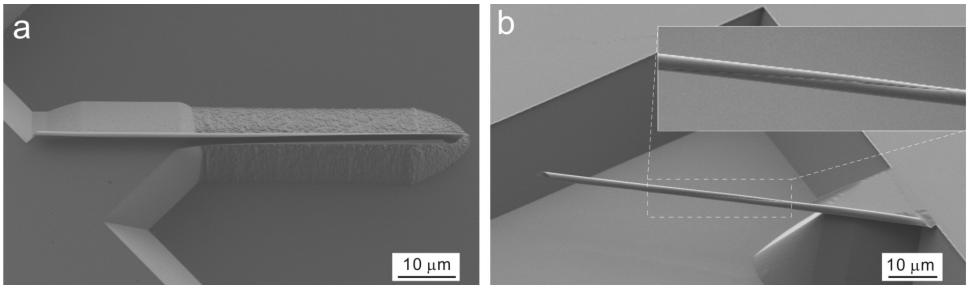

Figure 6.5: The seam of the tubes sometimes rotates along the tube axis. (a) FESEM image of a freestanding SiGe/Si/Cr microtube with less than one turn. (b) FESEM image of a freestanding SiGe/Si microtube. The inset shows the rotation of the seam.

The AFM manipulation of rolled-up 3-D micro-structures also shows some limitations. For example, to mount the AFM tip on tubes, it is operated by top-view observing under an optical microscope, so the position of the AFM tip on the tube cannot be controlled precisely. In addition, when the AFM cantilever is bending a tube, the deformation state of the tube cannot be simultaneously monitored. Thus, to manipulate the rolled-up microtubes in a better controllable way, nanorobotic manipulation technique is adopted.

6.2 Mechanical properties studied by nanorobotic manipulation

A nanorobotic manipulator (MM3A^{TM} from Kleindiek) holding a probe was installed inside a Zeiss DSM962 scanning electron microscope (SEM). The manipulator has 3-D freedom as shown in figure 6.6, with resolutions of 5 nm, 3.5 nm, and 0.25 nm in *X*, *Y*, and *Z* directions at the tip, respectively [86].

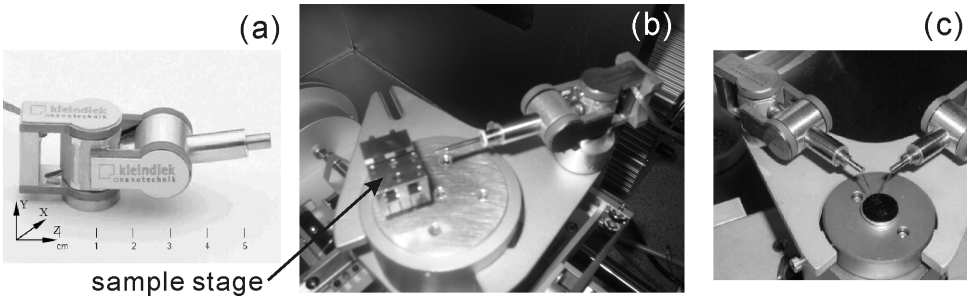

Figure 6.6: (a) Operation system of the nanorobotic manipulator (MM3A^{TM} from Kleindiek). (b) A manipulator installed in an SEM. (c) The geometric arrangement of the two manipulators installed in the SEM.

The standard tool of the manipulator is a commercially available tungsten sharp probe (Picoprobe T-1-10-1mm) shown in figure 6.7a. To facilitate different processes, special tools have been fabricated, including a nanohook (figure 6.7b) prepared by controlled "tip-crashing" of a sharp probe onto a substrate. A "sticky" probe is also prepared by dipping the tip of the probe into double-sided silver conductive tape (Ted Pella, Inc.) as presented in figure 6.7c-d. This sticky probe is used to cut individual freestanding SiGe/Si microtubes from the substrate.

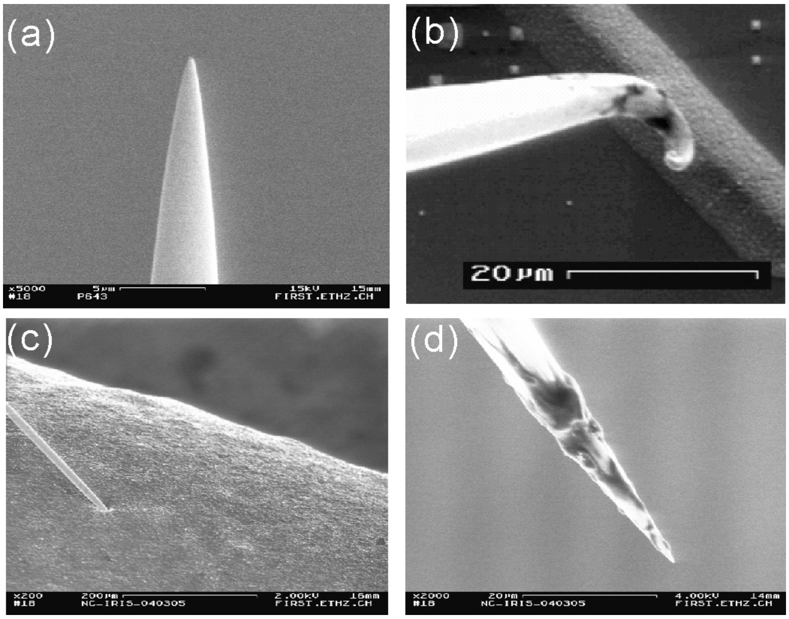

Figure 6.7: SEM images of the manipulator probe. (a) A conventional manipulator tungsten probe (b) A hook can be made by crashing the tip to the sample surface. (c) The probe is inserted into glue. (d) The probe with the glue on its tip.

6.2.1 Elasticity test

To investigate the flexibility of an individual SiGe/Si microtube, the manipulator probe (nanohook) has been used to bend the tube with different deflection angles between 0° and 180° as presented in figure 6.8. Surprisingly, the tube still can recover itself to the original shape after the probe was removed (figure 6.8b and figure 6.8d). No significant change of its shape due to the bending was observed in the SEM, indicating that these freestanding microtubes are extremely flexible even under a large deflection. The excellent elasticity of these microtubes also implies that the as-grown SiGe/Si heterostructure has a good quality, i.e. nearly free from dislocations. However, with a very large deflection angle (figure 6.8c), the tube could be strongly deformed locally (kinked) and dislocations may accumulate to the kinked position. Eventually, the tube will be fractured due to the severe deformation at the kinked position after repeating this bending test. With large deflection angles, i.e. larger than 120°, the tube usually has fatigue failure within less than 10 circles of the bending test.

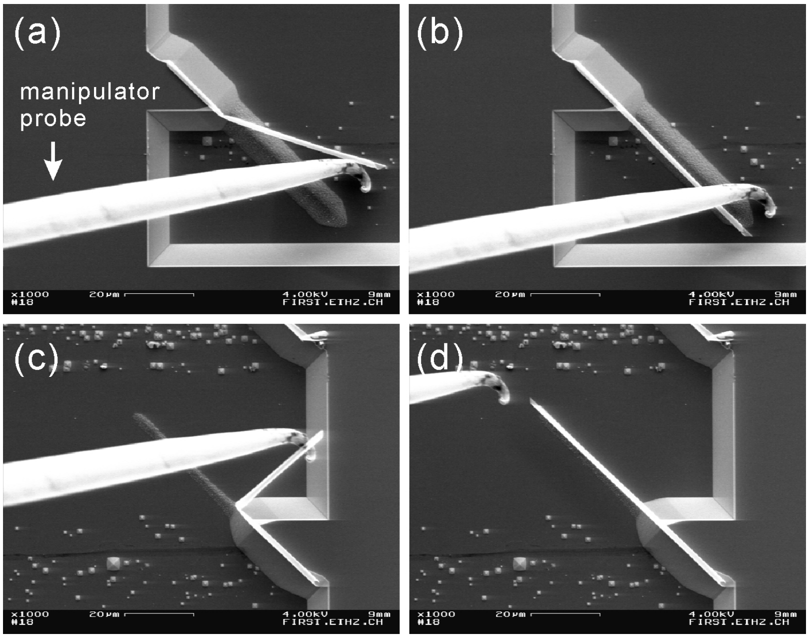

Figure 6.8: Bending tests of freestanding SiGe/Si microtubes. (a) A SiGe/Si microtube is bent about 30° by a manipulator probe; the probe is indicated by a white arrow. (b) The SiGe/Si microtube recovered to its original shape after the manipulator probe removed. (c) A SiGe/Si microtube is bent with a very large deflecting angle (90°) by manipulator probe. (d) The tube is recovered to its original shape, after the probe is removed.

6.2.2 Buckling test

Buckling test, as a non-destructive technique, has been shown effective in mechanical characterization of single carbon nanotubes using nanorobotic manipulation [87]. To test the flexural rigidity and the mechanical stability of individual SiGe/Si microtubes, the sticky probe was attached to a microtube near the place where the tube is fixed to the substrate, and then the probe is moved sidewise to cut the tube off from the substrate (see figure 6.9a). Next, the micromanipulator is used to bring the microtube into contact with the backside of an AFM cantilever and to maneuver it to a position so that its axis is perpendicular to the AFM cantilever, which is required for the subsequent buckling test. The main manipulation steps have been *in situ* recorded by SEM images as shown in figure 6.9b-d. The tube for buckling test is placed in such a way that its one end is attached to the ball-like joint at the sticky probe and the other end contacted to the backside of the AFM cantilever. However, this end of the tube is usually not well hold due to the flat backside of the AFM cantilever. To fix it better to the cantilever, a second type of AFM cantilever with a pyramid hole at the backside has been used. The latter configuration is favorable, because it becomes possible to adjust the angle between the tube and the manipulator probe, and an angle of 90 degree between the tube and the cantilever can be realized. Moreover, the microtube will not readily slide on the backside of the AFM cantilever during the buckling test. The buckling test is performed by pushing the “sticky” probe along the tube axis. Thus, the microtube is subjected to a uniaxial compressive stress and deflects the AFM cantilever, which has a known spring constant. The deflection of the AFM cantilever measures the compressive force applied to the longitudinal axis of the tube, from which the load and the stress on the microtube can be obtained.

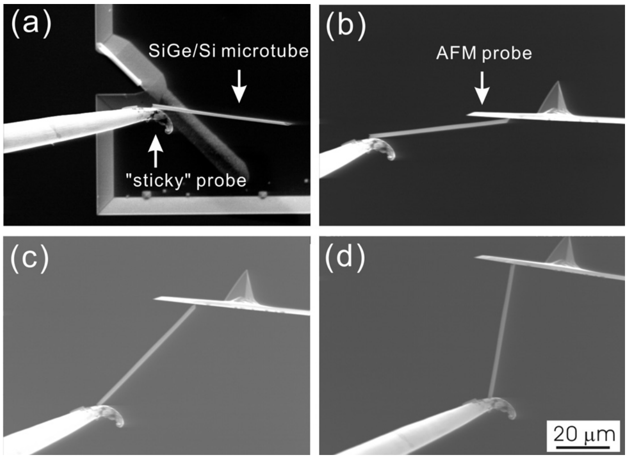

Figure 6.9: Nanorobotic manipulation of a freestanding SiGe/Si microtube. (a) Cutting and picking up a tube. (b) Placing, and (c-d) rotating the tube. All four SEM images have the same scale bar.

Figure 6.10 demonstrates a series of SEM images of the buckling test. The measured curve in figure 6.11 shows the dependence of the deformation of the microtube on the applied force for a SiGe/Si tube with a length of 61.6 μm. The deformation of the tube, i.e. ΔL in figure 6.12, is measured as the shortened length of the tube between its glued end on the manipulator probe and its free end on the AFM cantilever, which decreases during the buckling test. The distance is directly measured from the SEM in the experiment. Three evolution regimes can be identified in the buckling test. Initially, the load increases linearly with very small displacement; the microtube is in a stable equilibrium state and keeps itself straight (see figure 6.12a). In the second regime the curve becomes flat. The sudden drop of the slope indicates that the tube begins to be buckled (see figure 6.12b). Finally, in the third regime, the slope becomes steep again while the wall of the tube is severely bent. A typical Euler buckled [88] microtube is shown in figure 6.10f, where the bending of the tube is clearly visible. A further increase of the load leads to severely local deformation of the tube and finally to mechanical fracture of the microtube.

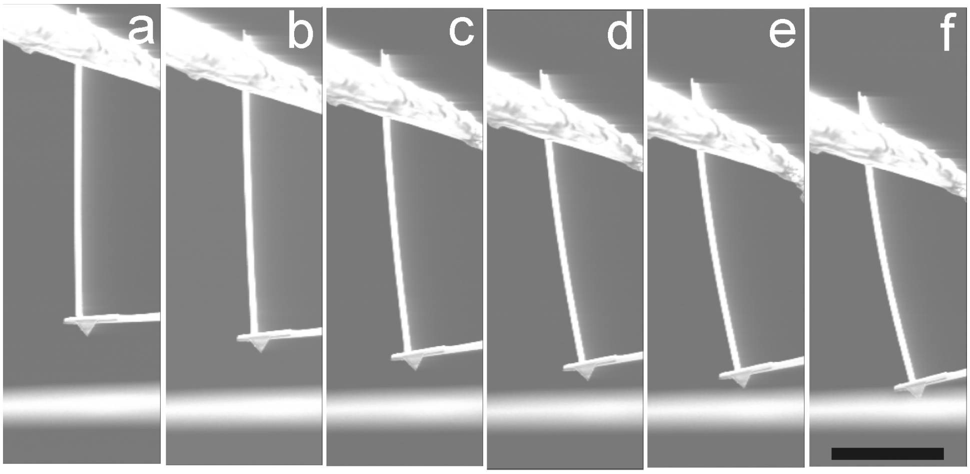

Figure 6.10: A series SEM images of buckling test of a SiGe/Si microtube. The scale bar for all images is 25 μm.

The kink point of the curve between the first and the second stage represents the neutral equilibrium of the microtube. The corresponding load is defined as the critical load (P_{cr}). As shown in figure 6.11, the value of the critical load close to 2.2 μN is determined for a 61.6 μm long 1.6-turn SiGe/Si microtube. The critical stress (δ_{cr}) can be expressed by:

$$\delta_{cr} = P_{cr} / A \qquad (6.5)$$

where A is the cross sectional area of the tube. The critical stress in this tube is worked out as 18.4 MPa. It should be noted that bilayers scrolled into incomplete tubes, e.g. ¾ of a turn, showed a critical stress approximately one order of magnitude smaller than that of the films scrolled by 1.6 turns. For a microtube with a length of 50.6 μm and the same diameter and wall thickness as the former, the tube keeps straight up to a compressive load of 2.5 μN, corresponding to a stress of 20.9 MPa. The displacement-load curve is presented in figure 6.11 with gray lines. In this experiment a cantilever with a flat back surface was used, hence this tube slipped away from the back side of AFM cantilever before it apparently buckled.

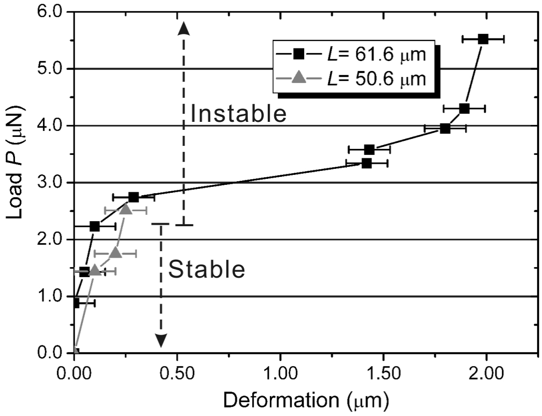

Figure 6.11: The experimental curve of force versus displacement resulted from buckling test for 61.6 μm and 50.6 μm long SiGe/Si microtubes. The stable and instable regions of the 61.6 μm long tube are marked in the diagram.

According to the Euler's formula [88], the critical load can be expressed as:

$$P_{cr} = \frac{\pi^2 EI}{L_{eff}^2} \qquad (6.6)$$

in which EI is the flexural rigidity, and L_{eff} is the effective length of the tube ($L_{\mathrm{eff}} = 2L$, for hinged-fixed condition and $L_{\mathrm{eff}} = L$ for hinged-free condition [42]). Using this formula the calculated critical load for an ideal seamless Si microtube with 61.6 μm length under hinged-fixed condition is about 1.23 μN. Here, the Young's modulus of Si from bulk material [85] and the Si tube with a diameter of 1.25 μm and a wall width of 19 nm have been assumed. The 1.6-turn rolled-up tube is approximated as a combination of an ideal tube and a 0.6 turn tube, so the cross sectional area is the sum of a thin circular ring and a thin circular arc. For this 1.6-turned ideal tube the critical load is calculated to be 2.0 μN, rather close to the experimental value (2.2 μN). This result indicates that the mechanical stability of a scrolled microtube, with 1.6 turns, is very similar to a seamless tube. Based on above results, it is presumable that the seamless model for calculation of the critical load and the flexural rigidity (*EI*) of the scrolled microtube would work even better for a tightly scrolled multi-turn tube with more turns, the larger numbers of the tightly wound turns of the tube's wall the higher accuracy of the modeling.

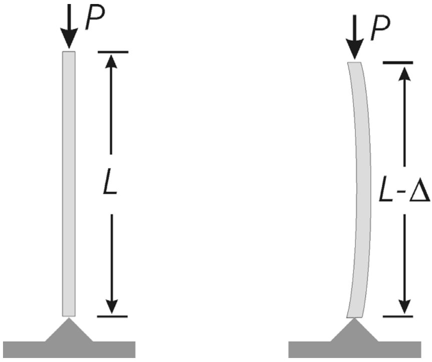

Figure 6.12: Model of the Euler buckling of a tube. When $P<P_{cr}$, the tube is mechanically stable (left), while $P>P_{cr}$, the tube will be buckled and bend sidewise. P_{cr} is the critical load (right).

The deviation of the real flexural rigidity of a scrolled microtube and the calculated value from the ideal tube model might result from the difference of the moment of inertia of cross sectional area *I*. For an ideal seamless tube, *I* can be calculated as $I = \frac{\pi}{8} d^3 t$ when $t \ll d$ [42], where *d* and *t* are the diameter and the wall thickness of the tube. However, the 1.6 turn rolled-up microtube actually has a seam along the tube axis.

In the rolled up bilayer the two edges of the rolled sheet do not bond together to form a seamless tube. However, when these edges overlap sufficiently the tubes become very stable. Surprisingly, the microtubes do not open along the seam when the axial compressive force is larger than the critical load. Additionally, the microtubes exhibit an excellent ability to recover from the post-buckling stage to their initial straight shape, as shown in figure 6.13. Moreover, in cycling of the experiment the critical load remained unchanged after the microtube recovered from the buckled state. This implies that the microtube is elastically deformed and no permanent damages occur in the SiGe/Si crystalline structure, even after it has been exposed to the instable state. An interesting observation is that in the third regime, the microtube becomes stiffer again (see figure 6.11). This may be attributed to the increase of the moment of inertia of the cross sectional area of the microtube. When the microtube is heavily buckled, the cross sectional shape is no longer ring-like. Also, in this stage the neighboring walls of the tube may interact with each other, leading to a reinforcement of the stiffness of the tube. When the microtube is strongly buckled, the internal (compression) side walls of the tube may open locally, which leads to highly localized stress. If the applied load is sufficient high, the tube will be destroyed in a brittle failure mode, which implies that the SiGe/Si microtubes may have much lower resistance to be fractured under tension [42].

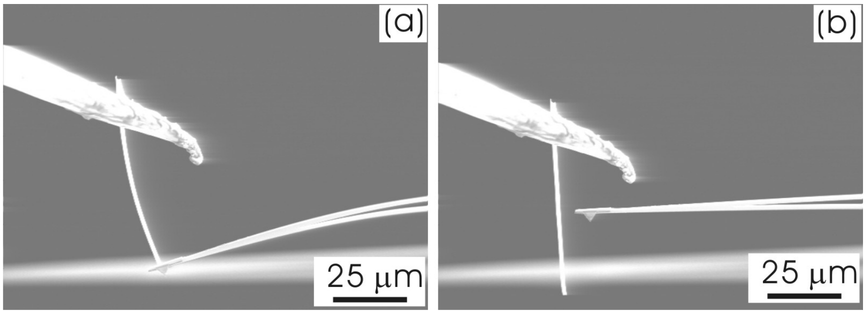

Figure 6.13: (a) Post-buckling state of a 61.6 μm long SiGe/Si tube. (b) The tube recovered from the axial compressive load.

6.2.3 Conclusions

Euler buckling has been experimentally observed in SiGe/Si microtubes when they are subjected to axial compressive load by nanorobotic manipulation. The flexural rigidity of the scrolled SiGe/Si microtube, which has 1.6 turns, is close to the ideal seamless tube. The self-scrolled SiGe/Si microtubes show no ductility and excellent elastic recovery from the post-buckling state. Our results also show that nanorobotic manipulation is a useful technique for the mechanical property characterization of rolled up micro-/nanostructures.

Chapter 7

Mechanical properties of Si-based helical structures

The as-fabricated 3-D micro-/nanohelices have many potential applications in semiconductors, electromagnetics and micro-/nanomechanics based on their specific shape and structure. As demonstrated in chapter 6 that nanomanipulation technique is a suitable method to investigate the properties of the 3D rolled-up structures. This newly developed analytical technique is also applied to examine the mechanical properties of rolled-up helical microcoils and other helical micro-/nanostructures such as spirals and multi-turn rings in this chapter.

7.1 Spring constant of SiGe/Si/Cr helical structures

7.1.1 Stretching test of a microcoil

A nanomanipulator and an AFM cantilever built in an SEM were used for the stretching test of individual helical nanobelts. The stiffness of the AFM cantilever used for this test was 0.06 N/m. The manipulation processes were conducted as follows: a tungsten probe on the manipulator was first dipped into a silver tape to make its tip sticky as already shown in figure 6.7. This probe was used to cut an one-end-fixed freestanding microcoil off from the substrate, and then the freestanding microcoil with its one end stuck on the probe's tip was picked up for the succeeding operations. In order to attach the other end of the microcoil to the AFM cantilever, the AFM tip was carefully dipped into the glue attached on the probe. After the microcoil was fixed between the probe and the AFM cantilever as shown in figure 7.1a, a tensile force was applied to the microcoil by moving the probe away from the AFM cantilever (see figure 7.1). Five continuous frames of SEM images were taken to detect the deflection of the cantilever and the elongation of the microcoil, i.e. the relative displacement of the probe to the AFM cantilever. Since the resolution of the SEM images (figure 7.1) is about 60 nm, the relative error of the coil deformation and the AFM cantilever deflection are estimated not more than 3% and 8% respectively.

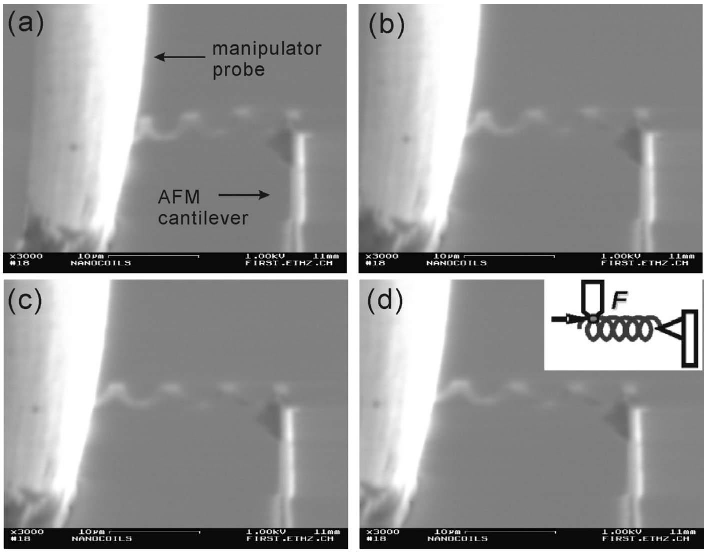

Figure 7.1: SEM images of the nanomanipulation for the spring constant measurement of a SiGe/Si/Cr microcoil in which the SiGe/Si bilayer thickness is 12/8 nm and the Cr layer is 21 nm thick. The diameter and the pitch of the coil are 3.4 μm and 7 μm respectively. The manipulator probe moves to the left.

From the displacement and the known stiffness of the AFM cantilever, the tensile force acting on the microcoil and the related microcoil elongation can be determined. Practically, the deformation of the microcoil was measured in such a way: the first measurement of the coil under a little tensile force is set as the initial stage (zero deformation) for the subsequent measurements. This is necessary because the proper attachment of the AFM cantilever to the microcoil must be checked in the first measurement. Accordingly, the plotted curve of the microcoil elongation versus the applied load in figure 7.2 has been shifted to start from the origin of the coordinate, i.e. zero load and zero elongation.

The resulted curve of elongation versus load (figure 7.2) shows that it is linear when the elongation of the microcoil is less than 4.5 μm (corresponding to a load of about 0.106μN), while it becomes nonlinear after the elongation is larger than 4.5 μm. When the applied force reached 0.176 μN, the attachment between the coil and the AFM cantilever disconnected. An exponential approximation was fitted to the nonlinear region of the curve. From the slope of the linear part of the curve in figure 7.2, the stiffness of the SiGe/Si/Cr coil is estimated to be 0.0233 N/m, which is approximately three times lower than that of the AFM cantilever. Finite element simulation (ANSYS 9.0) was used to validate the experimental data [89]. Since the contact point between the microcoil and the manipulator probe cannot be precisely identified by the SEM images, the number of the turns of the microcoil is estimated to be in the range of 4-5. Thus, simulations were conducted for 4, 4.5, and 5 turns respectively. The coil in the simulations was fixed on one end and had an axial load of 0.106 μN applied on the other end. From the simulation, stiffness values of 0.0302 N/m, 0.0230 N/m and 0.0191 N/m are resulted for the springs with 4, 4.5, and 5 turns, respectively. The measured spring constant (0.0233 N/m) is very close to the simulated value of the 4.5 turns microcoil (0.0230 N/m). The relative error arising from the measurement of the effective turn number of the microcoil falls into a range of about ± 22% between the minimum (0.0191 N/m) of 5-turn and the maximum (0.0302 N/m) of 4-turn according to the simulation.

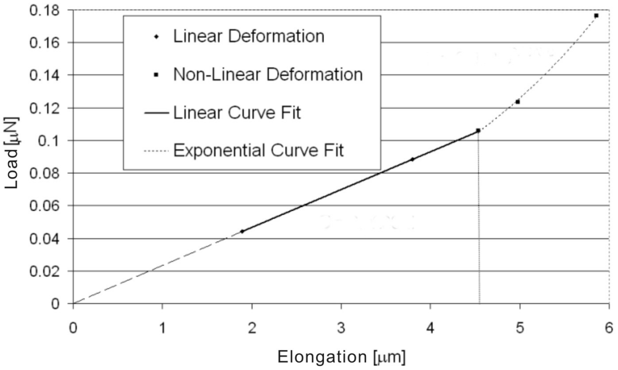

Figure 7.2: Measured spring constant of a SiGe/Si/Cr microcoil.

7.1.2 Stretching test of anomalously coiled nanohelices

The stretching test was also performed for SiGe/Si/Cr nanohelices in a field-emission scanning electron microscope (FESEM, Zeiss SUPRA 55VP). A typical anomalously coiled $Si_{0.6}Ge_{0.4}$/Si/Cr nanohelix with layer thickness of 11/8/21 nm is used in the experiment.

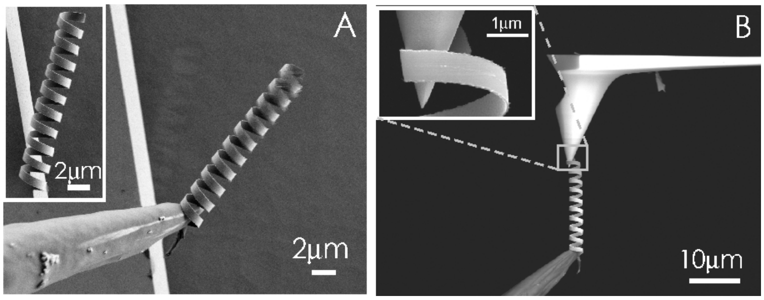

Figure 7.3: (A) Pick up an as-fabricated nanocoil (inset) to a tungsten probe. (B) Place it onto the tip of an AFM cantilever and solder it using EBID (inset).

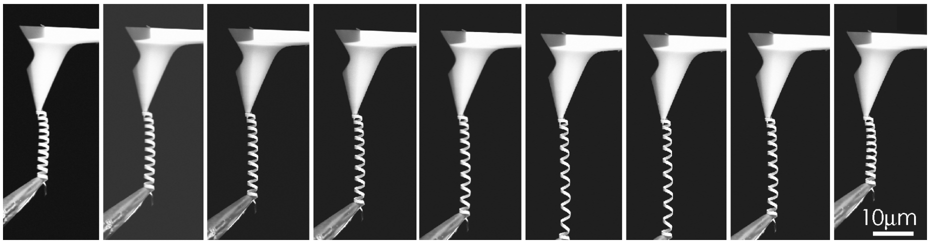

Figure 7.4: Pulling the nanocoil for stiffness characterization (All images have the same scale bar).

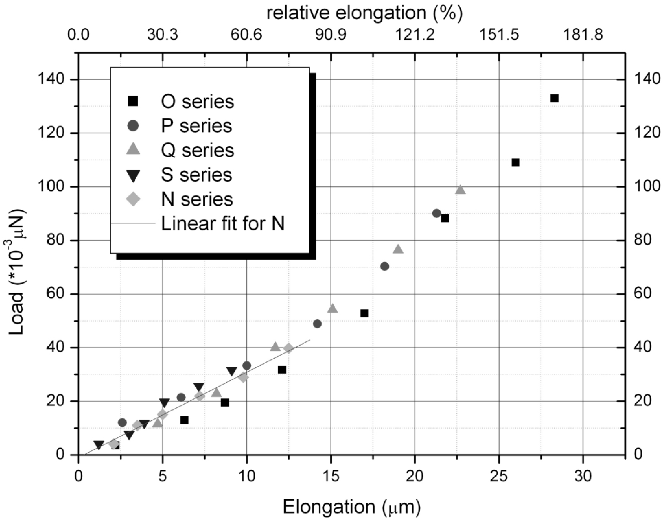

Figure 7.5: Elongation-load curves for a SiGe/Si/Cr nanohelix.

As shown in figure 7.3A, the as-fabricated nanohelix was first picked up by the manipulator with a sticky tip. The free end of the spring was then clamped onto an AFM cantilever (Fig. 7.3B, Mikromasch, CSC38/Ti-Pt, nominal stiffness 0.03 N/m) using electron-beam-induced deposition (EBID) [90]. To simplify the deposition process, the residual contamination (mainly hydrocarbons) in FESEM chamber was applied instead of precursor gas. The interaction of the primary e-beam (in focus mode) with the hydrocarbons results in a deposition of a hydrocarbon film on the contact place between the nanohelix and the cantilever [91]. The nanohelix was loaded under tension and unloaded successively for several cycles. Figure 7.4 shows a series of SEM images of the process. Applying a special software (SmartSEM^{TM} user interface) to the images from these experiments, the deformation of both the nanohelix and the AFM cantilever has been measured. The applied load was also calculated according to the deflections of the AFM cantilever (calibrated stiffness: 0.038 N/m). Figure 7.5 depicts the elongation vs. load curves for several series. Interestingly, the spring constant of the nanohelix remains constant as the spring is extended to 91% of its original length, which is six times of that of carbon coils (15%) [92] and more than twice that of rolled-up InGaAs/GaAs microcoils (40%) [93]. In the low strain region, linear fitting indicates a spring contestant of 0.003 N/m. This value is surprisingly small compared to the bottom-up synthesized nanocoils, which is only 1/40th of the spring constant of carbon coils (0.12 N/m) [92] and over three orders of magnitude less than that of superlattice ZnO nanohelices (4.2 N/m) [15]. Moreover, this value is also an order of magnitude smaller than that of the most flexible commercially available AFM cantilevers (on the order of 10^{-2} N/m). Thus, it is expected that using this nanospring as a visual based force sensor, a resolution as high as 3 pN/nm can be provided if an FESEM with an imaging resolution of approximately 1 nm is adopted for the displacement measurement.

7.2 Mechanical properties of Si/Cr micro-/nanostructures

7.2.1 Unrolling test for elasticity investigation

The as-fabricated Si/Cr in-plane spirals are manipulated for characterization of the elasticity by an unrolling test. Figure 7.6 shows a manipulator probe mounted on the manipulator approaching a spiral and being inserted into the hollow of the spiral (inset, figure 7.6). To investigate the flexibility of the spiral, the probe is used to extend it as shown in figure 7.7, where the spiral is completely extended along its longitudinal axis and subsequently recovers to its original shape after being released from the extension (see Fig. 7.7d). No significant change in its curvature was observed after the extension experiment, which indicates that these freestanding spirals have an excellent elasticity and good "memory" for their original shape.

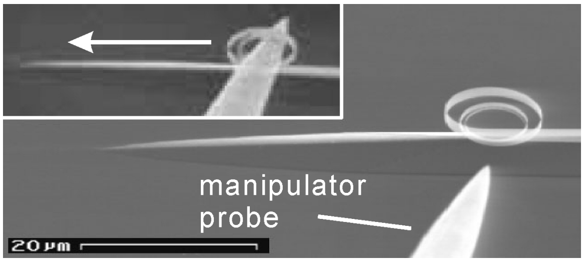

Figure 7.6: Manipulation of a Si/Cr spiral. The inset shows insertion of the probe into the spiral.

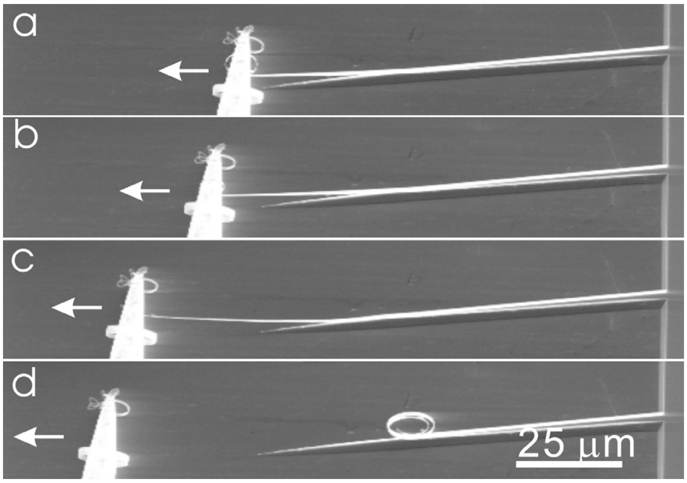

Figure 7.7: The manipulator probe translates to the left (white arrow) to unroll the Si/Cr spiral. (d) The spiral returns to its original shape. The scale bar is 25 μm in all four images.

The same unrolling test is also adopted for testing of multi-turn Si/Cr rings rolled up by 35/10nm thick Si/Cr nanobelt (Fig. 7.8). The multi-turn (2.5-turn) Si/Cr nanoring with a stripe width of 500 nm was strongly deformed during the unrolling process and the maximum relative elongation of the Si/Cr ring along the unrolling direction is about 50% as shown in figure 7.8d. After the multi-turn ring was unrolled until only less than one turn remained, the curvature elastically recovered to its original one as we can see in figure 7.8e. The unrolling test proves that the adjacent bilayers of a Si/Cr multiple-turn (more than 2 turns) ring are tightly wound and bonded together, thus can be considered as a physically closed ring-structure, instead of a spiral with zero-gap without interaction between the neighbouring bilayers. We attribute this "sticky force" mainly to van der Waals force. It is also expected that the magnitude of the "sticky force" depends on the tightly overlapped area of each turn of the ring-structure, and that larger overlapping areas of the bi-layers would generate larger bonding force. For instance, a Si/Cr multi-turn ring with a width of 1.1 μm (measured in the FESEM before the manipulation), as indicated by a white arrow in figure 7.8a, was fractured at its fixed end before it could be unrolled, and then stayed together with the manipulator probe. Thus, it is predictable that multiple-turn Si/Cr, SiGe/Si or SiGe/Si/Cr micro-/nanotubes become mechanically stronger by the bonding force between the neighbouring films when the number of the scrolled turns is increased.

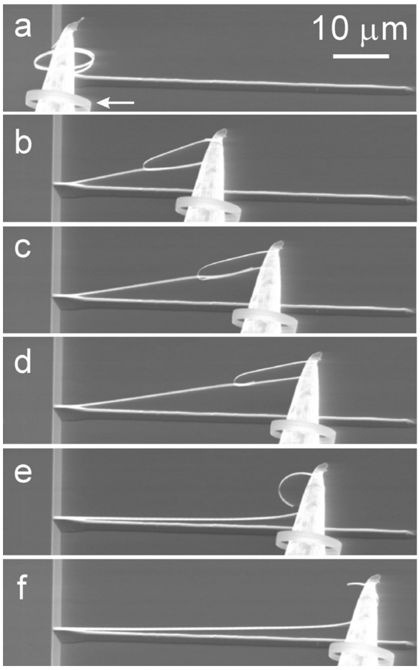

Figure 7.8: The manipulator probe translates from left to right to unroll a multi-turn Si/Cr ring. The width of the stripe is 500 nm. The white arrow points to another multi-turn Si/Cr ring with a stripe width of 1.1 μm.

7.2.2 Radial stiffness of a 2.5 turn Si/Cr ring structure

To investigate the radial stiffness of the multi-turn Si/Cr ring structure, an individual Si/Cr microring with stripe width of 1.2 μm is investigated. Firstly, the ring was cut and picked up from the Si substrate as shown in figure 7.9a. Then it was mounted on the backside of an AFM cantilever (see figure 7.9b-c) to subject a compressive or tensile load through pushing or pulling the ring by the manipulator probe. Figure 7.10a shows that the Si/Cr ring undergoes compression force. The compression stiffness of the 2.5 turn Si/Cr ring is obtained by measuring the slope of the compressive load and the corresponding deformation. Figure 7.10b presents the load-deformation curves of the compression test. The results demonstrate a linear relation between the compressive load and the deformation when the relative deformation of this 2.5 turns Si/Cr ring is smaller than 33%. Thus, the compression radial stiffness of the ring can be read directly from the slope of the load-deformation curves. In the first circle of the test, the two slopes are very close to each other, i.e. 0.133 N/m and 0.138 N/m. The compression tests also show that the top half of the ring has much less deformation than the bottom half, which is obviously due to the extra half turn of the ring structure on the top side. In addition, the distance from the outermost turn to the neutral plane (the undeformed plane) is larger than that from the inner turns, resulting in the higher flexural rigidity, because the rigidity increases quadratically with the distance to the neutral plane. The calculation shows that the flexural rigidity of the second turn of the ring is 14 times larger than that of the first turn. Therefore, the base half of the ring is more compliant (at least one magnitude less) and undergoes the most deformation which leads to the strong anisotropy of the radial stiffness of the ring. Stretching test of the Si/Cr ring has also been performed directly after the compression test as demonstrated in figure 7.11a. The linear fit line in the figure 7.11b indicates that with small deformation the radial stiffness under a tensile load is 0.332 N/m, which is much higher than that under a compression load. This can be understood that the deformation of the ring is confined more locally compared with the compression condition when it is subjected to a tensile force. The upper half of the ring has to follow the deformation as its bottom half does (see figure 7.12). During the compression and the stretching tests, no sliding between the neighbouring bilayers has been observed.

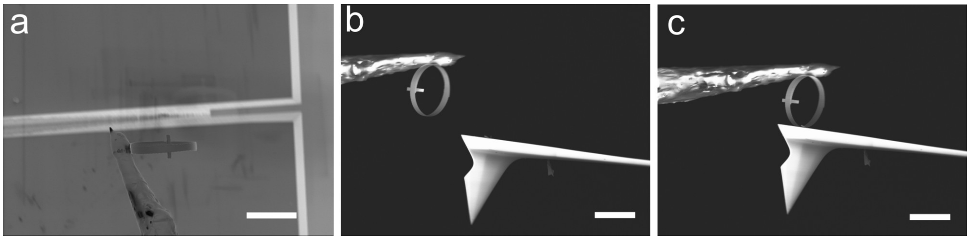

Figure 7.9: (a) A Si/Cr ring is cut from substrate by a sticky probe. (b-c) A Si/Cr ring is moved to the backside of an AFM cantilever by a manipulator probe. All three images have the same scale bar of 10 µm.

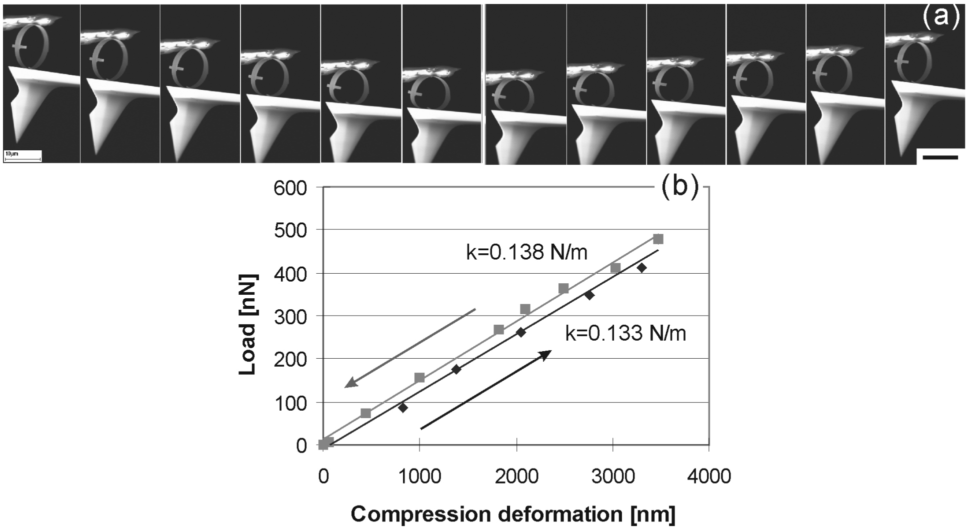

Figure 7.10: Radial stiffness test of an individual Si/Cr ring (35/10 nm). The ring has stripe width of 1.2 μm and diameter of 12.5 μm. (a) A series of FESEM images with increasing compression force on the Si/Cr ring and then recovering to zero compression. (b) Compression of load versus deformation from the first circle.

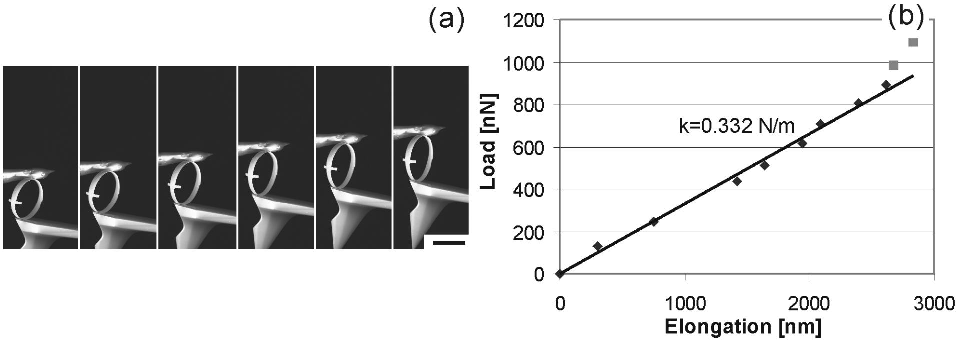

Figure 7.11: (a) A series of FESEM images with increasing tensile load on a Si/Cr ring. (b) Tensile load versus deformation. The scale bar is 10 μm for all of the FESEM images.

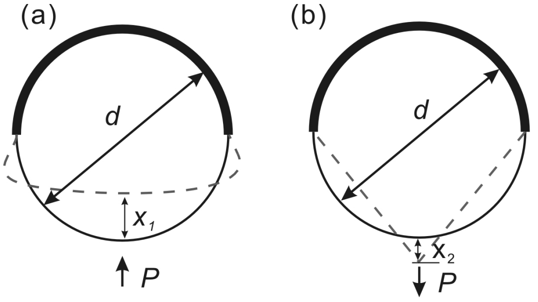

Figure 7.12: Assuming the stiffness of the upper half of the ring is much higher than the bottom half, when a load P is applied, only the bottom half of the ring will be deformed. However, due to the geometrical shape, the limitation of the deformation for the compression (x_1) and the stretching (x_2) is different, i.e. $x_1 < 0.5d$ *and* $x_2 < \frac{d}{2}\left(\frac{\sqrt{\pi^2-4}}{2}-1\right) \approx 0.1d$.

7.3 Conclusions

Our manipulation tests show that SiGe/Si/Cr helical structures are very elastic and they behave like micro-/nanosprings. The measured spring constant of the microcoil is consistent to the prediction given by the FEM simulation. According to tensile tests, the spring constant of the anomalously coiled SiGe/Si/Cr nanohelices keeps constant with much larger relative elongation region than microcoils. These excellent mechanical properties make them very promising to function as elastic elements in ultra-sensitive, large-range force/mass sensors and elastic elements of NEMS. The as-fabricated Si/Cr micro-/nanostructures, i.e. spirals and rings, exhibit excellent elastic recovery ability. The adjacent bilayers of the multiple-turn (more than 2 turns) Si/Cr ring are bonded together strongly, and the bonding between the adjacent bilayers does not break under compression loads in the experiments. The manipulation tests of the 2.5-turn ring also show that the radial stiffness is strongly influenced by the extra half turn of the ring structure.

Chapter 8

Summary and prospects

8.1 Summary

In this thesis, self-scrolling technique has been applied to fabricate a variety of 3D micro-/nanostructures, such as SiGe/Si, SiGe/Si/Cr and Si/Cr tubes and helices, which have novel properties for potential applications in MEMS/NEMS. Two fundamental issues are focused: one is related to controllable fabrication of the 3D rolled-up structures with mesa-structures going from micro- to nano-scale, and the other is to characterize properties of the micro-/nano-objects effectively. It is found that the rule of scrolling is significantly changed when the dimension of patterned thin films reduces to nanometer scale, which is particularly important for the design and fabrication of new realistic nano-devices. The mechanical and electrical properties of the as-fabricated 3D structures are examined by AFM, nanomanipulation and two-point probe methods respectively.

The scrolling behaviour of the patterned SiGe/Si bilayers and SiGe/Si/Cr hybrid films with the width of mesa-structures from micro- to nanometer range has been systematically investigated, which determines the nature of the finally formed 3D structures. Our fabrication results revealed that if the width of bilayers is in a micrometer scale or larger the scrolling direction is either determined by the smallest Young's modulus direction in the case of Si (001) substrate, or governed by the underetching speed for the substrates of Si (110) and (111). Two typical microstructures, i.e. micro-/nanotubes and helices have been successfully synthesized on Si(001) surface. Especially, the controllable fabrication of the helices has been achieved, which means that the chirality, the helicity angle and the pitch of helices can be quantitatively controlled by the starting 2D mesa design.

A remarkable result has been found when the mesa line is shrunk into nanometer scale, new effects from the edges of the stripe will cause the anomalous coiling of the nanohelices and influence the shape of the rolled-up nanostructure tremendously. The experimental results show that when the stripe width is reduced to 300 nm, for a total 20 nm thick SiGe/Si bilayer, the effect of stress relaxation at the edges of the stripe, rather than the Young's modulus, will dominate the scrolling process. The stress relaxation leads to a uniaxial strain component along the mesa line, which has been also confirmed by our finite element simulation (FEM). Based on this anomalous coiling principle, SiGe/Si nanocoils with helical angles between 0° to 45° have been able to be achieved, which breaks the limitation of 45° confined by the preferred <100> scrolling direction for the helices in micrometer scale. Depositing a metal layer on the bilayers can also be used to tailor the shape of the nanostructure. Moreover, "edge effects" have also been found in the rolled-up Si/Cr stripes, where the curvature radius first increases and then decreases with the reduction of the stripe width in the range from 3 μm to 100 nm. According to these effects, novel upstanding Si/Cr micro-/nanospirals have been realized by a special design. Our new findings of the anomalous coiling principle have offered an additional possibility to design and fabricate 3D nanostructures for their use in more practical purposes.

The conductivity of the micro-/nanotubes is of decisive significance for their application in micro-/nanoelectronics and MEMS/NEMS devices. Metal contacts were fabricated at the two ends of the structures by photolithography. The measured results from the two-probe method show that the highly boron doped (> 10^{20} cm^{-3}) SiGe/Si microtubes are very conductive with linear I-V curves. The conductivity matches the expectation with respect to the doping level and the thickness of the bilayer films. It is noticed, however, that the high doping level in the rolled-up structures to improve the etching selectivity leads to the losing of the semiconductivity, and has limited their application mainly to mechanical/electromechanical devices. Therefore, other etching selectivity methods to decrease the doping level of the SiGe/Si bilayers should be further considered.

Finally, mechanical properties of the rolled-up micro-/nanostructures were examined using atomic force microscopy and nanorobotic manipulation technique. The excellent elastic recovery characteristic of the SiGe/Si microtubes was discovered from bending and buckling tests. More significantly, the microtube with 1.6-turn is rather robust and mechanically stable, which is comparable to the ideal seamless tube. Not only the tubes, various helical micro-/nanostructures have also been probed using nanomanipulation technique. Stretching tests show that SiGe/Si/Cr microhelices (micro-structures) are very elastic and they behaved like micro-springs. The measured spring constant of the structure is consistent to the prediction from the FEM simulation. By tuning design parameters, i.e. the number of turns, the thickness of the wall, the width and orientation of the stripe, the diameter and the pitch of a helical spring with a required stiffness can be obtained through the simulation. A specific property of the SiGe/Si/Cr nanohelices (nanostructures) is found that on the contrary to microcoils under tension, the spring constant of the SiGe/Si/Cr nanohelices keeps constant within much larger relative elongation region. This excellent mechanical property makes them very promising to function as elastic elements in ultra-sensitive, large-range force/mass sensors and elastic elements of NEMS. The unrolling tests of the Si/Cr rings and the spirals have revealed that these upright helical micro-/nanostructures are very elastic and have a strong ‘‘memory’’ for their original shapes. Moreover, the unrolling tests of the multiwall Si/Cr rings testified that the adjacent Si/Cr bilayers bond together strongly and form a closed structure. The buckling and unrolling tests show that a multiple-turn rolled-up micro-/nanotube can be considered as a strong closed structure and can be used as pipeline for micro-/nanofluidics or micro-/nanoneedles for injection and so on. On the other hand, the nanorobotic manipulation technique is proven to be a suitable approach for mechanical properties characterization of the micro-/nanostructures.

Our above study shows that the self-scrolling technology is very promising for controllable fabrication of 3D micro-/nanostructures, which are good candidates for applications in MEMS/NEMS devices. Contrary to micro-structures, the nano-structures exhibit different scrolling behaviours that offer more opportunities for the design and fabrication of new fascinating devices.

8.2 Prospects

The study on controllable fabrication and effective property characterization of these rolled-up 3D micro-/nanostructures has shown a prospective future not only in the field of application for advanced micro-/nanodevices, but also in the new scope of research for the developing nanotechnologies. Some possible work is suggested below for the future prospective research and applications based on the current results.

According to our buckling and unrolling tests, it is promising to use the micro-/nanotube as needle for micro-injection or pipeline for micro-/nanofluidics. Our unrolling test of the multi-turn ring has shown rather strong bonding strength between the tightly wound bilayers; however, systematic study is yet to be done to work out the bonding strength of ring structures with varied stripe width and turns. For further works, it is possible to measure the unzipping force of the multiwall ring structure quantitatively by a nano-manipulation system combining with an AFM cantilever, although practically it is not an easy task. Also, bilayers with different hetero-structure, such as semiconductors or hybrid semiconductor/metal systems, can be used in the unrolling tests to investigate the different bonding strength due to the specific surface property in the contacting interface. Then the experimental results of the bonding force can be compared with finite element simulation to find the nature of bonding between different coiled films. In addition, it will be interesting to see whether the interface energy of the adjacent bilayers can be modified by post annealing process which is usually involved in wafer bonding technique to increase the bonding strength [94].

The bending test shows that the SiGe/Si microtubes have excellent flexibility, but their fatigue properties are still not well known. It is also an interesting subject to apply the rolled-up micro-/nanotube structures in vibrating devices such as oscillators in MEMS/NEMS because theoretically tube structure is a good candidate for high frequency devices.

Since semiconductor layer and metal layer have different coefficient of thermal expansion, semiconductor-metal hybrid 3D structure has high chances to be used as bimorph actuators which can be driven by thermal stress. However, new effects may occur to influence the internal stress at the semiconductor/metal interface of the bilayers. Also, electrostatic force can be applied to stimulate the semiconductor metal hybrid helical structure. The benefit from these rolled-up structures, which have only nanometer scale thickness, is that very large reversible deformation can be obtained.

More significantly, the mechanical properties investigation of the anomalous coiled SiGe/Si/Cr nanohelices shows remarkable high flexibility and exceptionally wide linear range which are far superior to either bottom-up synthesized nanocoils or rolled-up microcoils. Besides these features, the high degree of precision with which their diameter, chirality, helicity angle, and pitch can be controlled, indicating the high suitability for batch fabrication and the possibility for application of them as elastic elements in ultra-sensitive, large-range force/mass sensors and elastic elements of NEMS. With smaller stripe widths, more turns, by using higher resolution microscopy or other readout techniques, nanosprings can potentially provide femto-Newton (fN) to atto-Newton (aN) resolution. However, for their realistic applications in this field, closer cooperation between scientists and engineers will be essential. Thus, both the opportunity and challenge are involved for the future research and application of the novel rolled-up structures.

References

[1] K. Lee, "Private communication," EPFL, Lausanne, 2004.

[2] B. A. Korgel, "Nanosprings take shape," *Science*, vol. 309, pp. 1683-1684, 2005.

[3] E. D. Sone, E. R. Zubarev, and S. I. Stupp, "Semiconductor nanohelices templated by supramolecular ribbons," *Angewandte Chemie-International Edition*, vol. 41, pp. 1706-+, 2002.

[4] Y. Cui, X. F. Duan, Y. Huang, and C. M. Lieber, "Nanowire as Building Blocks for nanoscale Science and Technology," in *Nanowires and Nanobelts: Materials, Properties and Devices*, 1 ed. vol. 1, Z. L. Wang, Ed. Boston: Kluwer Academic, 2003, pp. 3-68.

[5] A. P. Alivisatos, "Semiconductor clusters, nanocrystals, and quantum dots," *Science*, vol. 271, pp. 933-937, 1996.

[6] T. Guo, P. Nikolaev, A. G. Rinzler, D. Tomanek, D. T. Colbert, and R. E. Smalley, "Self-Assembly of Tubular Fullerenes," *Journal of Physical Chemistry*, vol. 99, pp. 10694-10697, 1995.

[7] S. Iijima, "Helical Microtubules of Graphitic Carbon," *Nature*, vol. 354, pp. 56-58, 1991.

[8] S. Iijima and T. Ichihashi, "Single-Shell Carbon Nanotubes of 1-Nm Diameter," *Nature*, vol. 363, pp. 603-605, 1993.

[9] Y. Cui, L. J. Lauhon, M. S. Gudiksen, J. F. Wang, and C. M. Lieber, "Diameter-controlled synthesis of single-crystal silicon nanowires," *Applied Physics Letters*, vol. 78, pp. 2214-2216, 2001.

[10] A. M. Morales and C. M. Lieber, "A laser ablation method for the synthesis of crystalline semiconductor nanowires," *Science*, vol. 279, pp. 208-211, 1998.

[11] Z. W. Pan, Z. R. Dai, and Z. L. Wang, "Nanobelts of semiconducting oxides," *Science*, vol. 291, pp. 1947-1949, 2001.

[12] S. Amelinckx, X. B. Zhang, D. Bernaerts, X. F. Zhang, V. Ivanov, and J. B. Nagy, "A Formation Mechanism for Catalytically Grown Helix-Shaped Graphite Nanotubes," *Science*, vol. 265, pp. 635-639, 1994.

[13] S. Meister, H. Peng, K. McIlwrath, K. Jarausch, X. F. Zhang, and Y. Cui, "Synthesis and Characterization of Phase-Change Nanowires," *Nano Lett.*, vol. 6, pp. 1514-1517, 2006.

[14] X. Y. Kong and Z. L. Wang, "Spontaneous polarization-induced nanohelixes, nanosprings, and nanorings of piezoelectric nanobelts," *Nano Letters,* vol. 3, pp. 1625-1631, 2003.

[15] P. M. Gao, Y. Ding, W. J. Mai, W. L. Hughes, C. S. Lao, and Z. L. Wang, "Conversion of zinc oxide nanobelts into superlattice-structured nanohelices," *Science,* vol. 309, pp. 1700-1704, 2005.

[16] *Nanowires and Nanobelts: Materials, Properties and Devices*, 1 ed. Boston: Kluwer Academic, 2003.

[17] C. Dekker, "Carbon nanotubes as molecular quantum wires," *Physics Today,* vol. 52, pp. 22-28, 1999.

[18] S. Iijima, "Carbon nanotubes: past, present, and future," *Physica B-Condensed Matter,* vol. 323, pp. 1-5, 2002.

[19] C. M. Lieber, "Nanoscale science and technology: Building a big future from small things," *Mrs Bulletin,* vol. 28, pp. 486-491, 2003.

[20] C. M. Lieber, "Nanowires as building blocks for nanoscale science and technology," *Abstracts of Papers of the American Chemical Society,* vol. 227, pp. U1420-U1420, 2004.

[21] A. Cho, "NANOTECHNOLOGY: Pretty as You Please, Curling Films Turn Themselves Into Nanodevices," *Science,* vol. 313, pp. 164-165, 2006.

[22] V. Y. Prinz, V. A. Seleznev, and A. K. Gutakovsky, in *Proceedings of 24th International Conference on the Physics of Semiconductors,* N. Gershoni, Ed.: World Scientific, Singapore, 1999.

[23] V. Y. Prinz, V. A. Seleznev, A. K. Gutakovsky, A. V. Chehovskiy, V. V. Preobrazhenskii, M. A. Putyato, and T. A. Gavrilova, "Free-standing and overgrown InGaAs/GaAs nanotubes, nanohelices and their arrays," *Physica E,* vol. 6, pp. 828-831, 2000.

[24] O. C. Schmidt, N. Schmarje, C. Deneke, C. Muller, and N. Y. Jin-Phillipp, "Three-dimensional nano-objects evolving from a two-dimensional layer technology," *Advanced Materials,* vol. 13, pp. 756-759, 2001.

[25] O. G. Schmidt and K. Eberl, "Nanotechnology - Thin solid films roll up into nanotubes," *Nature,* vol. 410, pp. 168-168, 2001.

[26] S. V. Golod, V. Y. Prinz, V. I. Mashanov, and A. K. Gutakovsky, "Fabrication of conducting GeSi/Si micro- and nanotubes and helical microcoils," *Semiconductor Science and Technology,* vol. 16, pp. 181-185, 2001.

[27] S. V. Golod, D. Grutzmacher, C. David, E. Deckardt, O. Kirfel, S. Mentese, and B. Ketterer, "Fabrication of SiGe/Si/Cr bent cantilevers based on self-rolling of epitaxial films," *Microelectronic Engineering,* vol. 67-8, pp. 595-601, 2003.

[28] S. V. Golod, V. Y. Prinz, P. Wagli, L. Zhang, O. Kirfel, E. Deckhardt, F. Glaus, C. David, and D. Grutzmacher, "Freestanding SiGe/Si/Cr and SiGe/Si/SixNy/Cr microtubes," *Applied Physics Letters,* vol. 84, pp. 3391-3393, 2004.

[29] L. Zhang, S. V. Golod, E. Deckardt, V. Prinz, and D. Grutzmacher, "Free-standing Si/SiGe micro- and nano-objects," *Physica E-Low-Dimensional Systems & Nanostructures,* vol. 23, pp. 280-284, 2004.

[30] L. Zhang, E. Deckhardt, A. Weber, C. Schonenberger, and D. Grutzmacher, "Controllable fabrication of SiGe/Si and SiGe/Si/Cr helical nanobelts," *Nanotechnology,* vol. 16, pp. 655-663, 2005.

[31] L. Zhang, E. Deckardt, A. Weber, C. Schonenberger, and D. Grutzmacher, "Directional scrolling of hetero-films on Si(110) and Si(111) surfaces," *Microelectronic Engineering,* vol. 83, pp. 1233-1236, 2006.

[32] L. Zhang, L. X. Dong, D. J. Bell, B. J. Nelson, C. Schoenenberger, and D. Gruetzmacher, "Fabrication and characterization of freestanding Si/Cr micro- and nanospirals," *Microelectronic Engineering,* vol. 83, pp. 1237-1240, 2006.

[33] L. Zhang, E. Ruh, D. Grutzmacher, L. X. Dong, D. J. Bell, B. J. Nelson, and C. Schonenberger, "Anomalous Coiling of SiGe/Si and SiGe/Si/Cr Helical Nanobelts," *Nano Lett.,* vol. 6, pp. 1311-1317, 2006.

[34] L. Zhang, L. X. Dong, D. J. Bell, B. J. Nelson, C. Schoenenberger, and D. Gruetzmacher, "Euler Buckling of Individual SiGe/Si Microtubes," *Nanotech 2006 Conference Technical Proceedings,* vol. 1, pp. 42-45, 2006.

[35] D. J. Bell, Y. Sun, L. Zhang, L. X. Dong, B. J. Nelson, and D. Grutzmacher, "Three-dimensional nanosprings for electromechanical sensors," *Sensors and Actuators A: Physical,* vol. 130-131, pp. 54-61, 2006.

[36] R. Abermann and H. P. Martinz, "Internal stress and structure of evaporated chromium and MgF2 films and their dependence on substrate temperature," *Thin Solid Films,* vol. 115, pp. 185-194, 1984.

[37] G. Thurner and R. Abermann, "Internal stress and structure of ultrahigh vacuum evaporated chromium and iron films and their dependence on substrate temperature and oxygen partial pressure during deposition," *Thin Solid Films,* vol. 192, pp. 277-285, 1990.

[38] G. G. Stoney, "The tension of metallic films deposited by electrolysis," *Proceedings of the Royal Society of London Series a-Containing Papers of a Mathematical and Physical Character,* vol. 82, pp. 172-175, 1909.

[39] S. Timoshenko, "Analysis of bi-metal thermostats," *Journal of the Optical Society of America and Review of Scientific Instruments,* vol. 11, pp. 233-255, 1925.

[40] T. W. Clyne, "Residual stresses in surface coatings and their effects on interfacial debonding," in *Interfacial Effects in Particulate, Fibrous and Layered Composite Materials*. vol. 116-, 1996, pp. 307-330.

[41] Y. C. Tsui and T. W. Clyne, "An analytical model for predicting residual stresses in progressively deposited coatings .1. Planar geometry," *Thin Solid Films,* vol. 306, pp. 23-33, 1997.

[42] J. M. Gere, *Mechanics of materials,* 6 ed. Belmont, Calif: Brook/Cole - Thomson Learning, 2004.

[43] J. J. Wortman and R. A. Evans, "Youngs Modulus Shear Modulus and Poissons Ratio in Silicon and Germanium," *Journal of Applied Physics,* vol. 36, pp. 153-&, 1965.

[44] M. Grundmann, "Nanoscroll formation from strained layer heterostructures," *Applied Physics Letters,* vol. 83, pp. 2444-2446, 2003.

[45] S. Mendach, "InGaAs-Mikro- und Nanoröhrchen," in *Dissertation zur Erlangung des Doktorgrades des Fachbereichs Physik* Hamburg: Universität Hamburg, 2005.

[46] F. Schaffler, in *Properties of Advanced SemiconductorMaterials GaN, AlN, InN, BN, SiC, SiGe* M. E. Levinshtein, S. L. Rumyantsev, and M. S. Shur, Eds. New York: John Wiley & Sons, Inc., 2001, pp. 149-188.

[47] J. D. Plummer, M. Deal, and P. B. Griffin, *Silicon VLSI Technology - Fundamentals, Practice and Modeling*. New Jersey: Prentice Hall, 2000.

[48] M. J. Madou, *Fundamentals of microfabrication : the science of miniaturization* 2ed. Boca Raton, FL: CRC Press, 2002.

[49] B. S. Meyerson, "Uhv Cvd Growth of Si and Si-Ge Alloys - Chemistry, Physics, and Device Applications," *Proceedings of the IEEE,* vol. 80, pp. 1592-1608, 1992.

[50] D. J. Paul, "Silicon-germanium strained layer materials in microelectronics," *Advanced Materials,* vol. 11, pp. 191-+, 1999.

[51] J. W. Matthews and A. E. Blakeslee, "Defects in Epitaxial Multilayers .1. Misfit Dislocations," *Journal of Crystal Growth,* vol. 27, pp. 118-125, 1974.

[52] J. C. Bean, L. C. Feldman, A. T. Fiory, S. Nakahara, and I. K. Robinson, "Gexsi1-X/Si Strained-Layer Superlattice Grown by Molecular-Beam Epitaxy," *Journal of Vacuum Science & Technology a-Vacuum Surfaces and Films,* vol. 2, pp. 436-440, 1984.

[53] L. J. van der Pauw, "A method to measuring specific resistivity and Hall effect of discs of arbitrary shape," *Philips Research Reports,* vol. 13, pp. 1-9, 1958.

[54] "MICROPOSIT S1800 SERIES PHOTO RESISTS Data Sheet," SHIPLEY.

[55] S. D. Collins, "Etch Stops," in *Semiconductor Micromachining*. vol. 2, S. A. Campbell and H. J. Lewerenz, Eds. Chichester: John Wiley & Sons Ltd., 1998.

[56] U. Schnakenberg, W. Benecke, and B. Lochel, "Nh4oh-Based Etchants for Silicon Micromachining," *Sensors and Actuators a-Physical,* vol. 23, pp. 1031-1035, 1990.

[57] U. Schnakenberg, W. Benecke, B. Lochel, S. Ullerich, and P. Lange, "Nh4oh-Based Etchants for Silicon Micromachining - Influence of Additives and Stability of Passivation Layers," *Sensors and Actuators a-Physical,* vol. 25, pp. 1-7, 1991.

[58] S. A. Campbell, S. N. Port, and D. J. Schiffrin, "Anisotropy and The Micromachining of Silicon," in *Semiconductor micromachining*. vol. 2, S. A. Campbell and H. J. Lewerenz, Eds. Chichester: John Wiley & Sons Ltd., 1998.

[59] F. Wang, Y. Shi, J. L. Liu, Y. Lu, S. L. Gu, and Y. D. Zheng, "Highly selective chemical etching of Si vs. Si1-xGex using NH4OH solution," *Journal of the Electrochemical Society,* vol. 144, pp. L37-L39, 1997.

[60] V. Seleznev, H. Yamaguchi, Y. Hirayama, and V. Prinz, "Single-turn GaAs/InAs nanotubes fabricated using the supercritical CO2 drying technique," *Japanese Journal of Applied Physics Part 2-Letters,* vol. 42, pp. L791-L794, 2003.

[61] Z. Suo, E. Y. Ma, H. Gleskova, and S. Wagner, "Mechanics of rollable and foldable film-on-foil electronics," *Applied Physics Letters,* vol. 74, pp. 1177-1179, 1999.

[62] D. Kandall and G. de Guel, *Micromachining and Micropackaging of Transducers*. Amsterdam: Elsevier, 1985.

[63] B. C. S. Chou, C. N. Chen, and J. S. Shie, "Micromachining on (111)-oriented silicon," *Sensors and Actuators a-Physical,* vol. 75, pp. 271-277, 1999.

[64] J. Kim, D. Cho, and R. S. Muller, "Why is (111) silicon a better mechanical material for MEMS?," in *TRANSDUCERS-'01.-EUROSENSORS-XV*, 2001, pp. 662-5.

[65] H. Seidel, L. Csepregi, A. Heuberger, and H. Baumgartel, "Anisotropic Etching of Crystalline Silicon in Alkaline-Solutions .1. Orientation Dependence and Behavior of Passivation Layers," *Journal of the Electrochemical Society,* vol. 137, pp. 3612-3626, 1990.

[66] Y. Cui, Q. Q. Wei, H. K. Park, and C. M. Lieber, "Nanowire nanosensors for highly sensitive and selective detection of biological and chemical species," *Science,* vol. 293, pp. 1289-1292, 2001.

[67] M. Elwenspoek, "On the Mechanism of Anisotropic Etching of Silicon," *Journal of the Electrochemical Society,* vol. 140, pp. 2075-2080, 1993.

[68] M. Elwenspoek, "The form of etch rate minima in wet chemical anisotropic etching of silicon," *Journal of Micromechanics and Microengineering,* vol. 6, pp. 405-409, 1996.

[69] A. B. Vorob'ev and V. Y. Prinz, "Directional rolling of strained heterofilms," *Semiconductor Science and Technology,* vol. 17, pp. 614-616, 2002.

[70] D. J. Bell, L. X. Dong, Y. Sun, L. Zhang, B. J. Nelson, and D. Grutzmacher, "Manipulation of nanocoils for nanoelectromagnets," in *5th IEEE Conf. Nanotechnology*, Nagoya, 2005.

[71] Y. L. Shen, S. Suresh, and I. A. Blech, "Stresses, curvatures, and shape changes arising from patterned lines on silicon wafers," *Journal of Applied Physics,* vol. 80, pp. 1388-1398, 1996.

[72] A. Gouldstone, Y. L. Shen, S. Suresh, and C. V. Thompson, "Evolution of stresses in passivated and unpassivated metal interconnects," *Journal of Materials Research,* vol. 13, pp. 1956-1966, 1998.

[73] Y. Takagaki, Y. J. Sun, O. Brandt, and K. H. Ploog, "Strain relaxation in AlN/GaN bilayer films grown on gamma-LiAlO2(100) for nanoelectromechanical systems," *Applied Physics Letters,* vol. 84, pp. 4756-4758, 2004.

[74] J. P. Chang and H. H. Sawin, "Notch formation by stress enhanced spontaneous etching of polysilicon," *Journal of Vacuum Science & Technology B,* vol. 19, pp. 1870-1873, 2001.

[75] J. M. Gere, *Mechanics of materials* 6ed. Belmont, Calif: Brooks/Cole - Thomson Learning 2004.

[76] D. K. Schroder, *Semiconductor Material and Device Characterization*. New York: John Wiley & Sons Inc., 1990.

[77] K. C. Saraswat, "Advanced Integrated Circuit Fabrication Processes " *http://www.stanford.edu/class/ee311/NOTES/Ohmic_Contacts.pdf.*

[78] D. P. Kennedy and P. C. Murley, "A Two-Dimensional Mathematical Analysis of the Diffused Semiconductor Resistor," *IBM J. Res. Dev.,* vol. 12, pp. 242-250, 1968.

[79] E. W. Wong, P. E. Sheehan, and C. M. Lieber, "Nanobeam mechanics: Elasticity, strength, and toughness of nanorods and nanotubes," *Science,* vol. 277, pp. 1971-1975, 1997.

[80] J. P. Salvetat, J. M. Bonard, N. H. Thomson, A. J. Kulik, L. Forro, W. Benoit, and L. Zuppiroli, "Mechanical properties of carbon nanotubes," *Applied Physics a-Materials Science & Processing,* vol. 69, pp. 255-260, 1999.

[81] J. P. Salvetat, G. A. D. Briggs, J. M. Bonard, R. R. Bacsa, A. J. Kulik, T. Stockli, N. A. Burnham, and L. Forro, "Elastic and shear moduli of single-walled carbon nanotube ropes," *Physical Review Letters,* vol. 82, pp. 944-947, 1999.

[82] A. Kis, S. Kasas, B. Babic, A. J. Kulik, W. Benoit, G. A. D. Briggs, C. Schonenberger, S. Catsicas, and L. Forro, "Nanomechanics of microtubules," *Physical Review Letters,* vol. 89, 2002.

[83] W. L. Hughes and Z. L. Wang, "Controlled synthesis and manipulation of ZnO nanorings and nanobows," *Applied Physics Letters,* vol. 86, 2005.

[84] P. J. Cumpson, C. A. Clifford, and J. Hedley, "Quantitative analytical atomic force microscopy: a cantilever reference device for easy and accurate AFM spring-constant calibration," *Measurement Science & Technology,* vol. 15, pp. 1337-1346, 2004.

[85] J. J. Wortman and R. A. Evans, "Youngs Modulus Shear Modulus and Poissons Ratio in Silicon and Germanium," *Journal of Applied Physics,* vol. 36, pp. 153-156, 1965.

[86] L. X. Dong, L. Zhang, D. J. Bell, B. J. Nelson, and D. Gruetzmacher, "Hybrid Nanorobotic Approaches for Fabricating NEMS from 3D Helical Nanostructures," in *Proceedings of the 2006 IEEE International Conference on Robotics and Automation*, Orlando, Florida, 2006, pp. 1396-1401.

[87] L. X. Dong, F. Arai, and T. Fukuda, "Destructive constructions of nanostructures with carbon nanotubes through nanorobotic manipulation," *Ieee-Asme Transactions on Mechatronics,* vol. 9, pp. 350-357, 2004.

[88] S. P. Timoshenko and J. M. Gere, *Theory of elastic stability*. New York: Mcgraw-Hill, 1985.

[89] D. J. Bell, Y. Sun, L. Zhang, L. X. Dong, B. J. Nelson, and D. Grutzmacher, "Three-dimensional nanosprings for electromechanical sensors," *Sensors and Actuators a-Physical,* vol. 130, pp. 54-61, 2006.

[90] L. Dong, F. Arai, and T. Fukuda, "Electron-beam-induced deposition with carbon nanotube emitters," *Applied Physics Letters,* vol. 81, pp. 1919-1921, 2002.

[91] N. Sullivan, T. Mai, S. Bowdoin, and R. Vane, "A STUDY OF THE EFFECTIVENESS OF THE REMOVAL OF HYDROCARBON CONTAMINATION BY OXIDATIVE CLEANING INSIDE THE SEM," *Microscopy and Microanalysis,* vol. 8, pp. 720-721, 2002.

[92] X. Q. Chen, S. L. Zhang, D. A. Dikin, W. Q. Ding, R. S. Ruoff, L. J. Pan, and Y. Nakayama, "Mechanics of a carbon nanocoil," *Nano Letters,* vol. 3, pp. 1299-1304, 2003.

[93] D. J. Bell, L. X. Dong, B. J. Nelson, M. Golling, L. Zhang, and D. Grutzmacher, "Fabrication and characterization of three-dimensional InGaAs/GaAs nanosprings," *Nano Letters,* vol. 6, pp. 725-729, 2006.

[94] T. Qin-Yi, G. Cha, R. Gafiteanu, and U. Gosele, "Low temperature wafer direct bonding," *Microelectromechanical Systems, Journal of,* vol. 3, pp. 29-35, 1994.

Appendix: deducing the equation 6.1

1) When the AFM cantilever was pressed on a very stiff surface, the surface will not undergo any deformation, so the Z scanner displacement is equal to the cantilever deflection:

Z scanner displacement on Stiff Surface = constant * (Photodiode Signal Change on Stiff Surface):

$$dZ_{stiff} = a * dV_{stiff} \qquad \text{(b1)}$$

2) When the AFM cantilever was pressed on a freestanding tube, both the tube and the cantilever will experience deformation, therefore the z scanner displacement is the sum of the cantilever deflection and the tube deflection.

$$dZ_{tube} = a * dV_{stiff} + d_{tube} \qquad \text{(b2)}$$

where d_{tube} is the tube deflection.

3) And also, force from the cantilever to the tube is equal to the force from the tube to the cantilever

$$k_{AFM} * a * dV_{tube} = k_{tube} * d_{tube} \qquad \text{(b3)}$$

where k_{AFM} is the cantilever spring constant and k_{tube} is the bending stiffness of tube.

$$\text{So,} \quad k_{tube} = \frac{k_{AFM} * a * dV_{tube}}{d_{tube}} \qquad \text{(b4)}$$

4) Substituting Eq. (b2) to Eq. (b4),

$$k_{tube} = \frac{k_{AFM} * a * dV_{tube}}{dZ_{tube} - a * dV_{tube}} \qquad \text{(b5)}$$

5) And if we choose the ranges so that $dZ_{stiff} = dZ_{tube}$, we have

$$k_{tube} = \frac{k_{AFM} * a * dV_{tube}}{a * dV_{stiff} - a * dV_{tube}} \quad \text{(b6)}$$

Now we can get rid of constant *a*, which is the sensitivity of the AFM system setup:

$$k_{tube} = \frac{k_{AFM} * dV_{tube}}{dV_{stiff} - dV_{tube}} \quad \text{(b7)}$$

since $dZ_{stiff} = dZ_{tube}$,

$$k_{tube} = k_{AFM} * \frac{\frac{dV_{tube}}{dZ_{tube}}}{\frac{dV_{stiff}}{dZ_{stiff}} - \frac{dV_{tube}}{dZ_{tube}}} \quad \text{(b8)}$$

dV_{stiff}/dZ_{stiff} is the slope of the photodiode signal vs. displacement curve on stiff surface (N_{stiff}), and dV_{tube}/dZ_{tube} is the slope of the photodiode signal vs. displacement curve on sample (N_{tube}) which simplified Eq. (b8) to

$$k_{tube} = \frac{k_{AFM} * N_{tube}}{N_{stiff} - N_{tube}} \quad \text{(b9)}$$

$$\Rightarrow \quad k_{tube} = \frac{k_{AFM}}{\frac{N_{stiff}}{N_{tube}} - 1} \quad \text{(b10)}$$

This is the equation that we used to calculate the bending stiffness of the SiGe/Si tubes from AFM experimental data.

Publications List

Journal publications

1. S.V. Golod, V.Ya. Prinz, P. Wägli, L. Zhang, O. Kirfel, E. Deckardt, F. Glaus, C. David, D. Grützmacher, *Freestanding SiGe/Si/Cr and SiGe/Si/*Si_xN_y*/Cr microtubes*, *Appl. Phys. Lett.*, **84**, 3391 (2004).
2. L. Zhang, S.V. Golod, E. Deckardt, V. Prinz, D. Grützmacher, *Free-standing Si/SiGe micro- and nano-objects*, *Physica E*, **23**, 280 (2004).
3. L. Zhang, E. Deckardt, A. Weber, C. Schönenberger and D. Grützmacher, *Controllable Fabrication of SiGe/Si and SiGe/Si/Cr Helical Nanobelts*, *Nanotechnology*, **16**, 655 (2005). (this issue cover featured article)
4. D.J. Bell, L.X. Dong, B.J. Nelson, M. Golling, L. Zhang, D. Grützmacher, *Fabrication and Characterization of Three-dimensional InGaAs/GaAs Nanosprings for Electromechanical Sensors*, *Nano Lett.* **6**, 725 (2006).
5. L. Zhang, E. Deckardt, A. Weber, C. Schönenberger and D. Grützmacher, *Directional scrolling of hetero-films on Si (110) and Si (111) surfaces, Microelectron. Eng.* **83**, 1233 (2006).
6. L. Zhang, L.X. Dong, D.J. Bell, B.J. Nelson, C. Schönenberger, D. Grützmacher, *Fabrication and characterization of freestanding Si/Cr micro- and nano-spirals*, *Microelectron. Eng.* **83**, 1237 (2006).
7. D.J. Bell, Y. Sun, L. Zhang, L.X. Dong, B.J. Nelson, D. Grützmacher, *Three-Dimensional Nanosprings for Electromechanical Sensors, Sensors and Actuators A*, 130-131, **54** (2006).
8. L. Zhang, E. Ruh, D. Grützmacher, L.X. Dong, D.J. Bell, B.J. Nelson, C. Schönenberger, *Anomalous Coiling of SiGe/Si and SiGe/Si/Cr Helical Nanobelts*, *Nano Lett.* **6**, 1311 (2006). (Editor's choice: All Wound Up, *Science*, Vol. 312, 2006, pp. 1719)
9. D. Grützmacher, C. Dais, L. Zhang, E. Müller, H.H. Solak, *Templated self-organization of SiGe quantum structures for nanoelectronics*, , Mater. Sci. Eng. C. online.

Proceeding publications

1. D.J. Bell, Y. Sun, L. Zhang, L.X. Dong, B.J. Nelson, D. Grützmacher, *Three-Dimensional Nanosprings for Electromechanical Sensors,* Transducers ’05 Seoul Korea, 2005, pp. 15-18.
2. D.J. Bell, L.X. Dong, Y. Sun, L. Zhang, B.J. Nelson, D. Grützmacher. *Manipulation of Nanocoils for Nanoelectromegnets*, Proceedings of 2005 5th IEEE Conf. on Nanotechnology, Nagoya, Japan, 2005, pp. 303-306.
3. D. Grützmacher, Z. Li, E. Deckhardt, A. Weber, C. Schönenberger, *Scrolled Si/SiGe nano-helices for bio- and chemical sensors*, Physics, Chemistry and Application of Nanostructures, ed. V.E. Borisenko, S.V. Gaponenko, V.S. Gurin, World Scientific, ISBN 981-256-288-5, (2005) pp. 459-462.
4. D. J. Bell, L.X. Dong, B. J. Nelson, Y. Sun, L. Zhang, and D. Grützmacher, *Electromagnetic Nanoactuators Based on Nanocoils,* ASME Integrated Nanosystems (Design, Synthesis & Applications) Conf., 2005, Berkeley, US. pp. 14-16.
5. L. Zhang, L.X. Dong, D.J. Bell, B.J. Nelson, C. Schönenberger, D. Grützmacher, *Euler Buckling of individual SiGe/Si microtubes*, NSTI-Nanotech 2006, ISBN 0-9767985-6-5 Vol. 1, Boston, US. pp. 42-5.
6. L.X. Dong, L. Zhang, D.J. Bell, B.J. Nelson, D. Grützmacher, *Hybrid Nanorobotic Approaches for Fabricating NEMS from 3D Helical Nano-structures*, Proceedings of the 2006 IEEE International Conference on Robotics and Automation, Orlando, US, 2006, pp. 1396.
7. D. J. Bell, L.X. Dong, M. Golling , L. Zhang , B. J. Nelson , D. Grützmacher, *Analysis and Experiments for Fracture-Controlled Fabrication of Nanocoils, T*he 3rd Annual Conf. on Foundations of Nanoscience: Self-Assembled Architectures and Devices (FNANO2006), Apr. 23-27, Utah, US, pp. 12-18.
8. L.X. Dong, L. Zhang, D.J. Bell, B.J. Nelson and D. Grützmacher, *Nanorobotics for Creating NEMS from 3D Helical Nanostructures*, International conference on Nanoscience and Technology ICN&T 2006, Jul. 30-Aug. 4, Basel, Switzerland, accepted

Curriculum Vitae

Name	Li Zhang
Date of birth	13. 11.1978
Place of birth	Zhejiang, China
Nationality	Chinese

9.1990 - 7.1993	Middle school, Hangzhou, Zhejiang, China
9.1993 - 7.1996	High school, Hangzhou, Zhejiang, China
9.1996 – 7.2000	**Zhejiang University, Hangzhou, Zhejiang, China** B.Sc. in Materials Science and Engineering Thesis: Preparation, structural characterization and property of ZnO film deposited on Si substrate. (The thesis work was done in the State Key Lab. of Silicon Materials in Zhejiang University, China)
10.2000 – 9.2002	**Christian-Albrechts-University of Kiel, Germany** M.Sc. in Materials Science and Engineering Thesis: TEM investigation of self-assembled Ge islands on Si (110) substrate.
Since 10. 2002	**Paul Scherrer Institute (PSI) and University of Basel, Switzerland** Ph.D work has been done in the Laboratory for Micro- and Nanotechnology, CH-5232, Villigen PSI, Switzerland. PSI Supervisor: Dr. Detlev Grützmacher (Now has a professorship in physics department of RWTH Aachen, Germany) Ph. D candidate registered in the Institute of Physics, University of Basel, CH-4056 Basel, Switzerland. University supervisor: Prof. Dr. Christian Schönenberger

Acknowledgements

I would like to thank Dr. Detlev Grützmacher, my advisor at the Paul Scherrer Institute, for introducing and guiding me through this amazing “scrolling” research field, for fruitful discussing of my results and for careful revising of my manuscript for publication. His suggestion and comments were always very helpful. I am grateful to Professor Christian Schönenberger, my doctoral advisor at the University of Basel, for his supporting, understanding, generosity and always helpful discussion. Furthermore, I am obliged to Dr. Oliver Schmidt who gave me the honor to participate on the jury of this thesis.

Many thanks to Professor Jens Gobrecht, the head of the Laboratory for Micro- and nanotechnology at PSI, who gave me the chance to work in LMN and helpful comments for this thesis.

I am indebted to Professor Bradley Nelson at ETH Zurich who gives me the chance to investigate my pretty 3D structures with the nice facilities in his laboratory. I appreciate his helpful revision of my paper. Moreover, I will never forget his encouragement and recognition of my results.

My special thank goes to Dr. Lixin Dong, research staff of the Institute of Robotics and Intelligent Systems at the ETH Zurich for his countless help both in experiments and discussion. All of the nanorobotic manipulation experiments were done together with him (see section 6.2 and chapter 7).

Many thanks to Elisabeth Ruh for the finite element modeling presented at the chapter 4 (figure 4.23 and 4.24). Also, many thanks to Dominik Bell for the plotting of the figure 7.2 from our experimental results together with Dr. Lixin Dong (see Section 7.1.1).

Many thanks to Dr. Andrzej Kulik and Kyumin Lee at EPFL for a one-day AFM experiments. The experimental results in section 6.1 are achieved from their lab.

The controllable fabrication of 3D micro-/nanostructures is an important part of this thesis and requires the knowledge, experience and assistance of many people. I would like to express my deep thanks to all people of our lab for their continuous help and support. Without them this work would be never accomplished.

I would like to thank the Swiss National Science Foundation (SNF) for paying me to do this interesting research.

At the end, I am very deeply indebted to my beloved parents, for their everlasting understanding, support and encouragement.

Li ZHANG

9. 2006